Ⅲ-2

Materials Sciences

BL1B

Terahertz Spectroscopy of Ionic Liquids

T. Awano
Faculty of Engineering, Tohoku Gakuin University, Tagajo 985-8537, Japan

We have observed millimeter wave absorption bands in AgI-superionic conductive glasses previously [1,2]. These bands were also observed in CuI-superionic glasses at slight different peak positions[3]. These bands seems to be due to collective motion of conductive ions, although how conduction ions moves in correlation is not clear.

Ionic liquid is molten salt at room temperature because of large radius of component ions. Figure 1 shows molecular structures of [DEME] (a) and [Tf_2N] (b). It is interesting to compare ionic motion in ionic liquids with those in superionic conductor for investigation of dynamics of mobile ions. In superionic conducting glasses, only cation is movable.

Temperature dependence of absorption spectra of ionic liquids in spectral range between 20 to 60 cm^{-1} have measured to investigate change of dynamics of ions in process of change of state from liquid to solid. Transmittance spectra of one and two filter papers with the ionic liquid of the same quantity per the paper were measured. Absorption spectra were obtained by subtracting each other. To eliminate interference structure remaining in the spectra, absorption difference spectra between each spectrum and that at 86 K are shown in Figs. 2 and 3.

There observed some slight structures in the absorption spectra in terahertz region contrary to the previously reported THz-TDS result[4]. Temperature dependence of the absorption spectra showed similar tendency as the results in the millimeter wave region, that were obtained using coherent millimeter wave at the LINAC of the Kyoto University Research Reactor Institute[5]. Absorption intensity of [DEME][BF_4], which becomes solid (crystal) under 282 K, drastically decreased at that temperature. On the other hand, that of [DEME][Tf_2N], which becomes solid (glass) under 182 K decreased gradually. Absorption intensity of all other ionic liquids measured in this study decreased like these ones, concerning with the transition temperature of melting point or glass transition temperature.

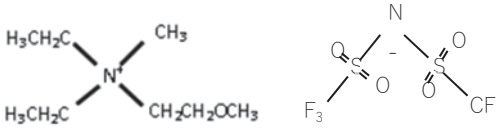

Fig. 1. Ionic structures of [DEME] (a) and [Tf2N] (b).

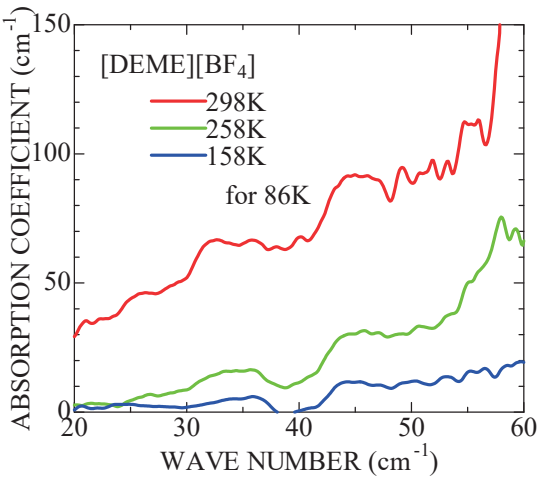

Fig. 2. Absorption increment spectra of [DEME] [BF_4] against the absorption spectrum at 86 K.

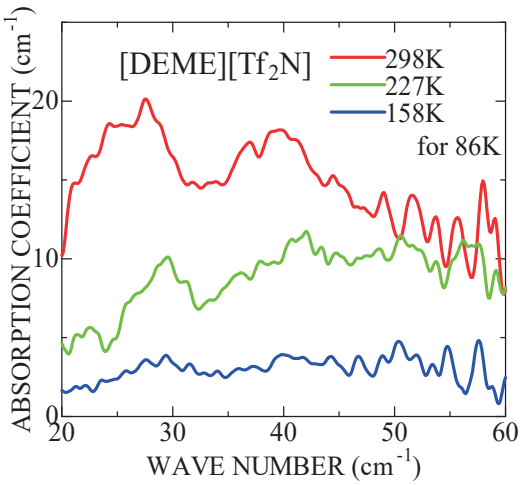

Fig. 3. Absorption increment spectra of [DEME] [Tf_4N] against the absorption spectrum at 86 K.

[1] T. Awano and T. Takahashi, J. Phys. Conf. Ser. **148** (2009) 012040.
[2] T. Awano and T. Takahashi, J. Phys. Soc. Jpn. **79** (2010) Suppl. A, 118.
[3] T. Awano and T. Takahashi, Proc. 13th Asian Conf. Solid State Ionics (2012) 569.
[4] T. Yamada, Y. Tominari, A. Tanaka and M. Mizuno, J. Phys. Chem. B **119** (2015) 15696.
[5] T. Awano and T. Takahashi, KURRI Prog. Rep. 2015, CO4-1.

BL1B

Optical Conductivity Spectra of Electron- and Hole-doped Anisotropic Kondo Semiconductor $CeOs_2Al_{10}$ in the THz Region

S. Kimura[1, 2], H. Takao[2], J. Kawabata[3], Y. Yamada[3] and T. Takabatake[3, 4]

[1]*Graduate School of Frontier Biosciences, Osaka University, Suita 565-0871, Japan*
[2]*Department of Physics, Graduate School of Science, Osaka University, Toyonaka 560-0043, Japan*
[3]*Department of Quantum Matter, ADSM, Hiroshima University, Higashi-Hiroshima 739-8530, Japan*
[4]*Institute for Advanced Materials Research, Hiroshima University, Higashi-Hiroshima 739-8530, Japan*

An anisotropic Kondo semiconductor $CeOs_2Al_{10}$ exhibits an unusual antiferromagnetic order at rather high transition temperature T_0 of 28.5 K [1]. Two possible origins of the magnetic order have been proposed so far, one is the Kondo coupling of the hybridization between the conduction (c) and the 4f states and the other is the charge-density wave/charge ordering along the orthorhombic b axis [2,3]. To clarify the origin of the magnetic order, we have investigated the electronic structure of hole- and electron-doped $CeOs_2Al_{10}$ [$Ce(Os_{1-y}Re_y)_2Al_{10}$ and $Ce\sigma$ $(Os_{1-x}Ir_x)_2Al_{10}$, respectively] by using optical conductivity [$\sigma(\omega)$] spectra along the b axis.

$\sigma(\omega)$ spectra, which were derived from the Kramers-Kronig analysis of reflectivity spectra, along the b axis at $T = 10$ K in $\hbar\omega < 100$ meV are shown in Fig. 1(a). In this region, it should be noted that a very sharp peak owing to a transverse optical phonon is observed at around 25 meV in all samples. Except for the sharp peak, one Drude component owing to carriers and three interband transition peaks are observed in all samples.

To clarify the change of the spectra by increasing x and y, we adopt the Drude-Lorentz fitting method. The $\sigma(\omega)$ spectra are fitted by using the combination of one Drude and three Lorentz functions. The obtained values of the effective electron number N^* together with T_0 and γ are plotted in Fig. 1(b) as functions of Re (y) and Ir (x) concentrations. Firstly, the carrier density (N^* of Drude component) is almost proportional to the electron specific heat coefficient γ. Secondly, the intensity of the c-f hybridization gap (N^* of $\Delta_{c\text{-}f}$) at $\hbar\omega$ ~ 50 meV continuously decreases from $y = 0.10$ to $x = 0.12$ via $x = y = 0$. On the other hand, the intensity of the charge excitation (N^* of Δ_0) observed at $\hbar\omega$ ~ 20 meV has the maximum at $x = y = 0$ as similar with the doping dependence of T_0. The fact that the charge excitation is strongly related to the magnetic order strengthens the possibility of the charge density wave/charge ordering as the origin of the magnetic order [4].

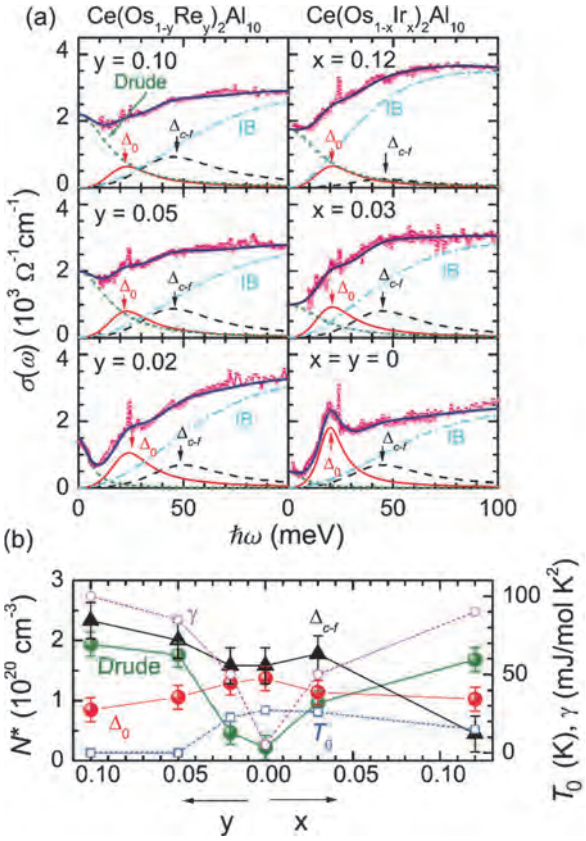

Fig. 1. (a) $\sigma(\omega)$ spectra along the b axis at $T = 10$ K and the fitted lines of one Drude and three Lorentz functions. The three Lorentz functions are assumed as a peak (Δ_0, solid line) appearing below the magnetic ordering temperature T_0, the interband transition in the c-f hybridization gap ($\Delta_{c\text{-}f}$, dashed line), and higher interband transition from lower energy side (IB, dot-dashed line). (b) Obtained effective electron numbers (N^*s) of the Drude, Δ_0, and $\Delta_{c\text{-}f}$ components, which are plotted together with T_0 and the electronic specific heat coefficient as functions of the Re (y) and Ir (x) concentrations.

[1] A. M. Strydom, Physica B **404** (2009) 2981.
[2] S. Kimura, T. Iizuka, H. Miyazaki, A. Irizawa, Y. Muro and T. Takabatake, Phys. Rev. Lett. **106** (2011) 056404.
[3] S. Kimura, T. Iizuka, H. Miyazaki, T. Hajiri, M. Matsunami, T. Mori, A. Irizawa, Y. Muro, J. Kajino and T. Takabatake, Phys. Rev. B **84** (2011) 165125.
[4] T. Yoshida, T. Ohashi and N. Kawakami, J. Phys. Soc. Jpn. **80** (2011) 064710.

BL2A

Local Structural Evaluation of Alloy Nitrides Extracted by Electrolytic Extraction Method

M. Sato
Institute for Materials Research, Tohoku University, Sendai 980-8577, Japan

It is well known that the martensite phase obtained by quenching is hard but brittle. Therefore the balance between hardness and toughness is adjusted by the subsequent tempering treatment. At that time, cementite is precipitated in case carbon steel, and Fe_4N is precipitated in case of nitrogen steel [1, 2].

Although it is known that alloying elements partially dissolve in solid solution in these precipitates, there is little knowledge on the chemical state of these substitution elements in the precipitates. In this study, changes in the chemical state of the substitutional elements before and after tempering treatment were investigated by XAFS measurement.

Fe-1mass%Si and Fe-1mass%Mo alloys were used as starting materials. They were homogenized at 1523 K for 24h and furnace-cooled until room temperature. Fe-1Mo-0.3N and Fe-1Si-0.3N alloys were prepared by nitriding and quenching process using NH_3/H_2 mixed gas at 1273 K for 1 h. Then Fe-1Mo-0.3N and Fe-1Si-0.3N alloys were tempered at 773 K for 1 h. and precipitates generated during tempering were extracted using Iodine-alcohol procedure. The Si K-edge and Mo $L_{Ⅲ}$-edge XANES spectra were corrected by fluorescence method using InSb double crystal monochrometer and silicon drift detector (SDD) at BL-2A in UVSOR, respectively. Obtained data were analyzed using Athena software.

Figure 1 shows Si K-edge XANES spectra of (a) ~ (c) references and (d) ~ (f) samples. Since the obtained spectrum from the as-quenched sample mainly had the similar shape with that of the Si powder (see Fig 1(a) and (d)), and it was suggested that Si atoms are substituted into the Fe structure. However, peak was observed around 1844 eV, which is consistent with the white line of SiO_2, suggesting a partial oxidation of sample. In case of the tempered sample, a new peak appeared around 1842 eV consistent with the white line of Si3N4 in addition to the above peaks. On the other hand, the spectrum of the extracted residue showed two peaks around 1842 and 1844 eV, and these peak positions were consistent with the white line of Si_3N_4 and SiO_2, respectively.

Figure 2 shows Mo $L_{Ⅲ}$-edge XANES spectra of (a) reference and (b) ~ (d) samples. No change in spectral shape was observed before and after tempering. This result indicate that local structure around Mo atom does not change by tempering treatment. However, the spectrum of the extracted powder sample showed chemical shift to the high energy side, implying the precipitation of Mo compounds. From this result, it was suggested that a trace amount of Mo is precipitating as compounds such as Mo nitrides etc. In the future, detailed examination will be carried out by analysis of the EXAFS region and calculation using FEFF code.

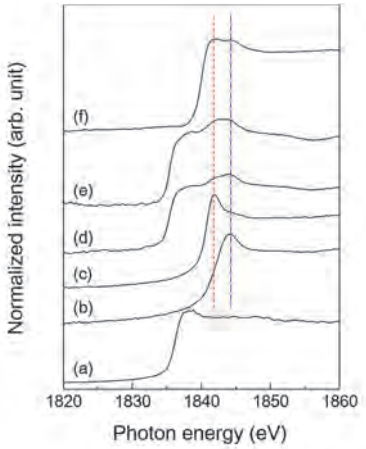

Fig. 1. Si K-edge XANES spectra of samples. (a) Si, (b) SiO_2, (c) Si_3N_4, (d) as quenched Fe-1Mo-0.3N alloy, (e) tempered Fe-1Mo-0.3N alloy and (f) extracted residue.

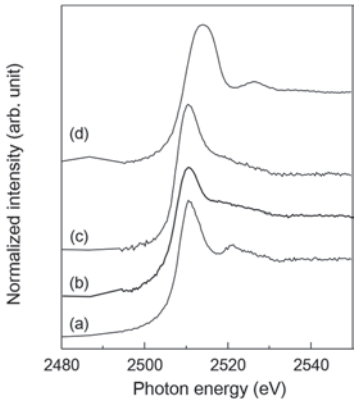

Fig. 2. Mo $L_{Ⅲ}$-edge XANES spectra of samples. (a) Mo foil, (b) as quenched Fe-1Mo-0.3N alloy, (c) tempered Fe-1Mo-0.3N alloy and (d) extracted residue.

[1] L. Cheng and E. J. Mittemeijer, Met. Trans. A **21A** (1990) 13.
[2] L. Cheng, A. Bottger and E. J. Mittemeijer, Met. Trans. A **23A** (1992) 1129.

BL2A

Characterization of MTB-Active Mo-Carbide Species Supported on H-MFI Catalysts by Mo L_{III}-edge XANES

H. Aritani[1], S. Mogi[1], R. Yamazaki[1], M. Akutsu[1], K. Kawashima[1], M. Tsutsumi[1] and A. Nakahira[2]

[1]*Graduate School of Engineering, Satama Institute of technology, Fukaya 369-0293 Japan*
[2]*Graduate School of Engineering, Osaka Prefecture University, Sakai 599-8531 Japan*

For direct conversion of LNG (Liquified natural gas) to useful organic compounds, Mo-modified H-MFI is a typical catalyst for MTB (Methane to Benzene) reaction, *i.e.*, methane dehydroarimatization. The MTB reaction is very unique and useful for industrial methane conversion, however, coke deposition over the catalyst cannot be avoided during the reaction.[1] At the same time, active Mo species should be changed structurally because of excess carburizaiton on both Mo species and acid sites of H-MFI.[2] For obtaining the durable MTB reactivity, the deactivation process over the catalysts is one of an important point to develop the industrial MTB catalysts. In this study, time course of the characterization of active Mo species for MTB (manly Mo_2C species) on H-MFI zeolites in various Si./Al_2 ratios is investigated by means of Mo L_{III}-edge XANES.

Catalyst samples were prepared by impregnation of each H-MFI (Si/Al_2=28 and 40) support with $MoO_2(acac)_2$–$CHCl_3$ solution (in 5wt% as MoO_3), and followed by dried and calcined at 773 K. The H-MFI supports were synthesized hydrothermally at 413 K for a week, and followed by ion-exchanging with NH_4Cl and calcined at 873 K. The catalytic MTB reactivity was evaluated by means of fixed-bed flow reaction at 1023 K, as described in a separate paper [1]. Mo L_{III}-edge XANES spectra were measured in BL2A of UVSOR-IMS in a total- electron yield mode using InSb double-crystal monochromator. Photon energy was calibrated by using Mo metal-foil, and normalized XANES spectra and their derivatives are presented. REX-2000 (Rigaku Co.) software was used by normalization of each XANES spectrum.

Figure 1 shows the time course of the Mo L_{III}-edge XANES spectra over MTB-active Mo/H-MFI (in Si/Al_2 ratios are 28 and 40) catalysts during the reaction. For Mo/H-MFI in Si/Al_2=28, higher MTB activity and lower deactivation are shown than in Si/Al_2=40. For these catalysts, edge energy of L_{III}-XANES becomes lower by proceeding the MTB reaction. This result indicates that a carbonization of molybdenum species advanced according to the reaction time. On the other hand, the MTB reactivity has been maximized at 30-55 minutes over Mo/H-MFI (Si/Al_2=28-40) catalysts. For the XANES spectrum, metallic Mo species can be seen at 30-90 minutes over these catalysts. The result suggests the formation of active Mo species as well-dispersed metallic ones. For Mo/H-MFI (Si/Al_2=40), the XANES spectra at 180 minutes (well-deactivated) shows the formation of α-Mo_2C species with higher edge energy than that of metallic one. In contrast, the XANES spectra of Mo/H-MFI (Si/Al_2=28) shows excess carbonized Mo species at 180 minutes. These results suggest the relationship between the formation of α-Mo_2C species and deactivation of Mo species for MTB reaction. For obtaining more details, metal-ion promoted Mo/H-MFI catalysts have been employed to characterize the highly active Mo species for MTB. This study is now in progress.

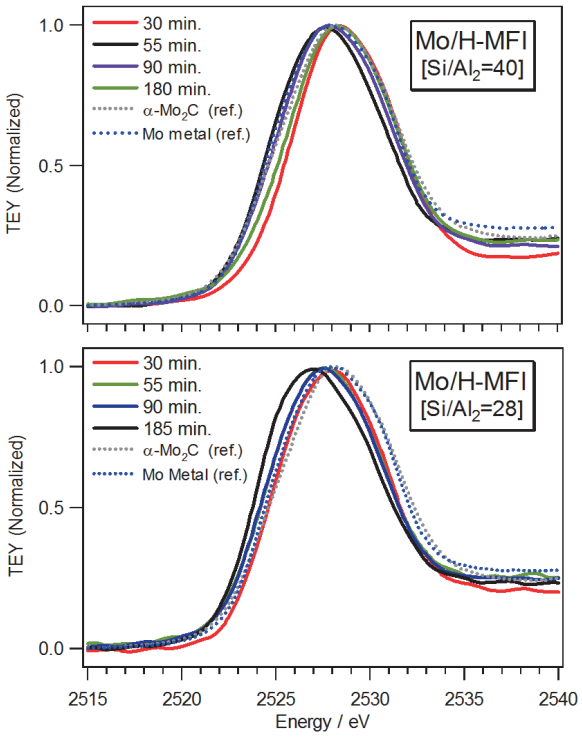

Fig. 1. Time course of the Mo L_{III}-edge XANES spectra over Mo/H-MFI [Si/Al_2 ratios are 28 (top) and 40 (bottom)] catalysts during the MTB reaction.

[1] H. Aritani, H. Shibasaki, H. Orihara and A. Nakahira, J. Environm. Sci. **21** (2009) 736.
[2] H. Aritani, S. Mogi, N. Naijo, T. Sugawara, A. Akutsu, K. Kawashima and A. Nakahira, UVSOR Activity Report **43** (2016) 49.

BL2A

XAS Analysis of Charge State of Eu in $Ba_2Eu_xBi_{(2-x)}O_6$ Double Perovskite

A. Kamata[1] and T. Yamamoto[1, 2]

[1]*Faculty of Science and Engineering, Waseda University, Tokyo 169-8555, Japan*

[2]*Institute of Condensed-Matter Science, Waseda University, Tokyo 169-8555, Japan*

Bithmus is an interesting elements, which can stably exist as various charge states, 3+ and 5+ for Bi. Especially, both of Bi^{3+} and Bi^{5+} can exist in one material, e.g., in $BaBiO_3$ with the ratio of Bi^{3+}:Bi^{5+} = 1:1. This is simply because of keeping the charge neutrality in the material. When the Bi^{3+} and Bi^{5+} exist periodically, say 3+,5+,3+,5+, …, superlattice should be constructed, one of which is shown in Fig. 1 drawn with VESTA [1]. This structure is called as double perovskite structured $BaBiO_3$. It was reported that this double perovskite structure can be stabilized with the doping of rare-earth ions. In the case of Ce doping, however, no double perovskite structure appeared. [2] Although it is essential to know substition site and charge state of doped rare-earth, such have not been clearly understood yet. In the current study, charge state of Eu ions in $BaBiO_3$ has been examined with Eu-M_5 X-ray absorption spectrum (XAS) measurements.

All the samples were fabricated with the solid-state reaction method. Reagent grade powders, $Ba(CO)_3$, Bi_2O3, Eu_2O_3 were ground and mixed in an agate mortar in air for 30 min. with ethanol, which were calcined at 1073 K for 6 hours in air. Resultant powders were ground and mixed again, which were pressed into a pellet form (10 mmϕ). These pellets were sintered in air at 1123 K for 12 hours.

Crystal structures of synthesized materials were examined by the conventional powder X-ray diffraction technique with Cu-Kα X-rays, which showed all the samples have double perovskite structure.

Eu-M_5 XAS were measured at BL2A in UVSOR with the total electron yield method. Samples powders were put on the carbon adhesive tape, which were attached on the first Cu-Be dinode of the electron mutiplier. Synchrotron beams were monochromatized with beryl (10-10)double- crystal monochrometar.

Observed Eu-M_5 XAS of Eu-doped $BaBiO_3$ are shown in Fig. 2 together with that of Eu_2O_3. All the Eu-M_5 XAS are almost identical and similar to that of Eu_2O_3. From the comparison with the standard oxide, in which Eu ions exist as trivalent, we can safely determine the charge state of the Eu ions in $BaBiO_3$ is trivalent.

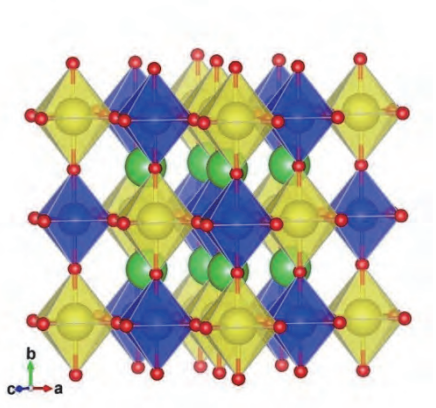

Fig. 1. Schematic illustration of double perovskite structured $BaBiO_3$. Green, blue, yellow and red balls denote Ba^{2+}, Bi^{3+}, Bi^{5+} and O^{2-} sites, respectively [1].

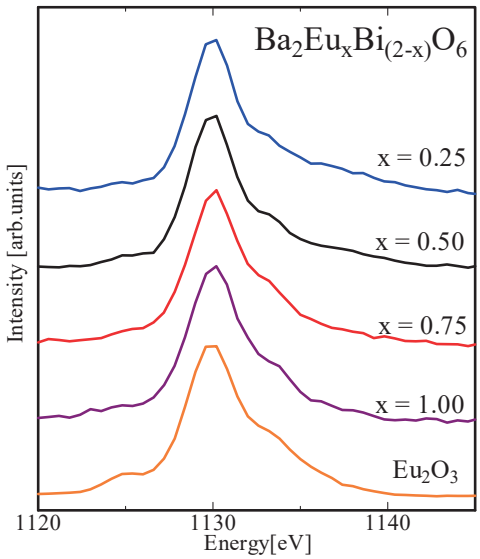

Fig. 2. Observed Eu-M_5 XAS spectra of $Ba_2Eu_xBi_{(2-x)}O_6$ and Eu_2O_3.

[1] K. Momma and F. Izumi, J. Appl. Crystallogr. **44** (2011) 1272.

[2] A. Matsushita *et al.*, Jpn. J. Appl. Phys. **51** (2012) 121802.

BL2A

Structural Evaluation of AlPO-5 with Si

A. Nakahira[1, 2], M. Togo[1], T. Takahashi[1], T. Minami[1], C. Takada[1], M. Matsumoto[1], M. Iida[1] and H. Aritani[3]

[1]*Faculty of Engineering, Osaka Prefecture University, Sakai 599-8531, Japan*
[2]*Trans-Regional Corporation Center for Industrial Materials Research (IMR), Tohoku University, Sakai 599-8531, Japan*
[3]*Saitama Institute of Technology, Fukaya 369-0293, Japan*

In recent years, the micro- and meso-porous inorganic materials attract much attention with growing concern about a lot of environmental problems. Although especially porous aluminophosphate (AlPO-n) is one of unique microporous materials, these materials have low catalytic ability. In order to achieve the catalytic activities of AlPO-n, various heterovalent elements have been incorporated into the framework of AlPO-n. These modified AlPO-n were generally found to incorporate negative charges in the framework, and extra-framework cations are present to balance the charges. For example, AlPO doped with Si, that is "SAPO-n", was synthesized to achieve the catalytic properties. In the so-called SAPO-n, a portion of P(V) is replaced by Si(IV). In special, SAPO-34 has attracted much attentions on the MTO (methanol to olefin) reaction because of high specific surface area, adsorptive capacities, and excellent catalytic activities.

The purpose in this study was to evaluate the local structure of SAPO-34 synthesized by the static hydrothermal process at 473 K using various starting materials and organic-structure-directing-agents (SDA) like tetraethylammonium hydroxide (TEAOH). The effect of synthetic condition parameters (starting materials, SDA, temperature, and time, etc) on the microstructure for various SAPO-34 samples was investigated.

All chemicals were analytical reagent-grade, and they used without further purification. The reagants used were γ-alumina, phosphoric acid, morpholine, and various silicon sources (TEOS, SiO_2, colloidal silica, and fumed silica etc). SAPO-34 were synthesized from starting gel with the composition of Al_2O_3 : P_2O_5 : TEAOH : SiO_2 : H_2O =1.0 : 1.6 : 4.0 : (0.3~0.6) : 140. γ-alumina was first mixed with TEAOH as a SDA and deionized water at room temperature. Various silica sources were then added into the mixture. Finally, phospholic acid was added dropwise to the resultant solution. The reaction mixture was further stirred for 1 h prior to being transferred into a stainless steel autoclave. The crystallization was conducted in an oven through the static hydrothermal process with preprogrammed heating profiles at 473 K for 24 h. In order to investigate the influence of hydrothermal synthetic conditions the samples were characterized. After all of the ground product powders were characterized by XRD method, FT-IR and TG-DTA. The microstructures of product powder were observed by SEM. The local structures around Si for the products of samples were characterized by measuring X-ray adsorption near edge structure (XANES) at BL02A in UVSOR.

The evaluation of XRD was carried out for various products synthesized by the static hydrothermal process. According to XRD results, products prepared by this hydrothermal process at 473K with the colloidal silica and fumed silica (0.3) as a silicon source and TEAOH as a SDA were identified to be SAPO-34. And similarly products with high contents of 0.6 for silica were composed of SAPO-34. Figure 1 shows the XANES spectra of various SAPO-34 samples with colloidal silica and fumed silica (0.6). As shown in Fig. 1, XANES spectra of sample obtained by hydrothermal process were quite similar. Furthermore, SAPO-34 with the high contents of colloidal silica and fumed silica as a silicon source were similar to SAPO-34 with low content of silica.

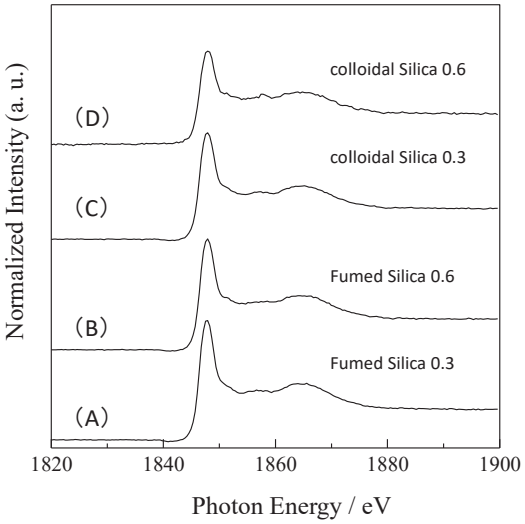

Fig. 1. Si-*K* XANES spectra of various products synthesized by the hydrothermal process at 473 K. (A) fumed silica of 0.3, (B) fumed silica of 0.6, (C) colloidal silica of 0.3, and (D) colloidal silica of 0.6.

BL2A

Soft X-ray Irradiation Effect on the Local Structural Deformation in a Molecular Conductor

T. Sasaki
Instutute for Materials Research, Tohoku University, Sendai 980-8577, Japan

It has been known that X-ray irradiation to the organic materials causes molecular defects and disorder. We have investigated the X-ray irradiation effect widely in the series of molecular materials κ-(BEDT-TTF)$_2$X showing superconductivity or Mott insulating state from the viewpoint of the relation between the correlated electronic states and randomness [1, 2]. Recently, we investigated the local structure deformation induced by X-ray irradiation in κ-(BEDT-TTF)$_2$Cu[N(CN)$_2$]Br using density functional theory based first-principles calculations [3]. The crystal structure is shown in Fig. 1. The calculations demonstrate that the structure change due to X-ray excitation can be predicted by introducing a core-hole at specific light atoms of anion molecules with infinite lifetime. Formation of the bond-shifted structure around dicyanamide group (NC-N-CN) in the anion layer was expected as a possible irreversible molecular defect leading to permanent irradiation damage.

In this study, soft X-ray irradiation experiments in organic conductor κ-(BEDT-TTF)$_2$Cu[N(CN)$_2$]Br was carried out in order to prove the calculation results. BL2A soft X-ray beamline was used for the irradiation. Beryl crystal was used for the monochromator at the soft X-ray photon energy of 1000 eV. The energy monochromatic soft X-ray was directory irradiated to the small single crystal surface in a vacuum chamber at room temperature. Total irradiation time was 52 hours. To determine the defect sites in the crystal, change of the molecular vibration modes was measured by means of the infrared optical reflectance experiments.

Figure 2 shows the mid-infrared reflectivity spectra ($E//a$ and $E//c$) of the crystal at 300 K before (black) and after 52 hours irradiation (red). Peak structures at approximately 1390 (Fig. 2(a)) and 2150 cm^{-1} (Fig. 2(b)) have been assigned to the vibration modes related to the dicyanamide group in the anion molecules, which have been significantly suppressed by white X-ray irradiation by using the tungsten tube with 40 kV in the lab experiments [1]. In the present SR soft X-ray irradiation, however, no detectable change was observed in the both vibration modes. Some possible reasons are expected such as short irradiation time, weak intensity, small penetration depth, and so on. We will check these points carefully for making next plans, including soft X-ray absorption experiments on the crystals irradiated by using the tungsten tube in advance to detect a defect structure consisting dicyanamide group.

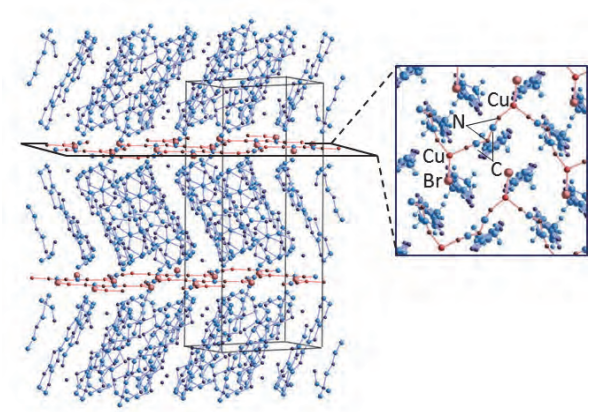

Fig. 1. Crystal structure of κ-(BEDT-TTF)$_2$Cu-[N(CN)$_2$]Br.

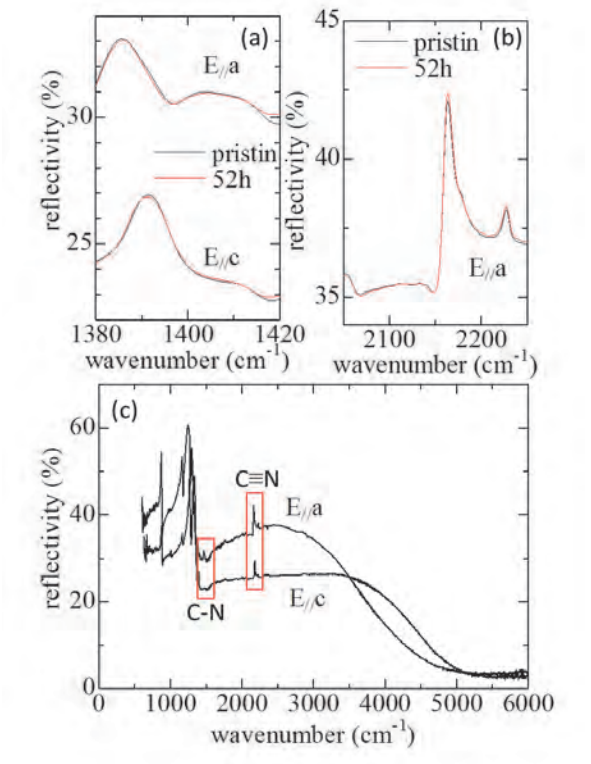

Fig. 2. IR optical reflectivity of κ-(BEDT-TTF)$_2$Cu-[N(CN)$_2$]Br before and after 52 hours soft X-ray irradiation.

[1] T. Sasaki, Crystals **2** (2012) 374.
[2] T. Furukawa *et al.,* Phys. Rev. Lett. **115** (2015) 077001.
[3] L. Kang, K. Akagi, K. Hayashi and T. Sasaki, submitted.

BL2A

Al *K*-edge XANES of AlN Films Doped with 3*d* Transition Metals

N. Tatemizo and S. Imada

Faculty of Electrical Engineering and Electronics, Kyoto Institute of Technology, Kyoto 606-8585, Japan

Recently, the doping of semiconductors with 3*d*-transition metals (3*d*-TMs) has been extensively investigated in order to realize semiconductors exhibiting additional electronic states and having improved properties. At high concentrations (~10%), the 3*d*-TMs' orbitals will start to overlap with one another, to form an impurity band. Such an impurity band well apart from the conduction band (CB) and the valence band (VB) can intermediate optical excitations of electrons from the VB to the CB when the impurity band is partially filled by electron. This is so called an intermediate band (IB) material proposed by Luque *et al.*, for use in absorption layers of solar cells to increase their conversion efficiency [1].

For wurtzite III-nitrides, such as AlN and GaN, the doped 3*d*-TMs can not only form impurity bands in the band gap but also reconstruct the intrinsic VB and CB when the 3*d*-TMs occupy III element sites due to non-centrosymmetry of the site. This can result in band gap narrowing of the semiconductors. In fact, it was reported that the band gap energy of GaN doped with 9% Cr, is 3.1 eV, whereas that of un-doped GaN is 3.4 eV [2].

Expecting both the band gap narrowing effect and sub-bandgap absorptions such as VB-IB and IB-CB, we chose AlN (*Eg* = 6.2 eV) as a base semiconductor for our study. In our previous study, it was shown that (i) the AlCrN films demonstrate distinctive optical absorption properties in the ultraviolet-visible-infrared region as shown in Fig. 1. and (ii) the top of valence band of wurtzite AlCrN (up to 17.1% Cr) contains considerable Cr *d* component via various photoemission spectroscopies and *ab initio* calculations [3].

In wurtzite AlN, main component of the bottom of the conduction band is Al *s* and *p* states, while that of the top of the valence band is N *p* [4]. To investigate effects of the 3*d*-TM doping on the conduction band of AlN, we carried out Al *K*-edge XANES measurements. Figure 2 shows Al *K*-edge XANES spectra and a differential spectrum of AlCrN with 10.46% Cr and un-doped AlN films. The electric field of the incident light was parallel to the *c*-plane of wurtzite structure. There are two features in the spectra: (i) the peak intensities of main edge (1558.5 and 1564.5 eV) in the AlCrN are lower than those of the AlN, and (ii) a small shoulder or tail is observed at around 1555eV. The former implies decrease of Al *p* local DOS in this energy region due to disorder associated with random distribution of Cr. The latter implies formation of unoccupied DOS under the bottom of the CB. Both the features in the Al *K*-edge XANES suggest that Cr atoms distribute homogeneously in the films. Further investigations such as incident angle and concentration dependences of the Al *K*-edge XANES measurements will reveal the effect of 3d-TM doping to the CB structure of the films.

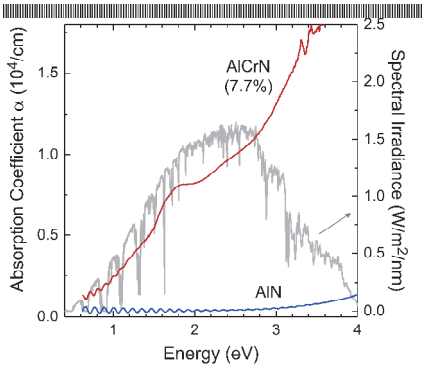

Fig. 1. Absorption coefficient α spectra of AlN and AlCrN films (7.7%) with the solar spectral irradiance for air mass of 1.5. The noise at high α region in the spectra is because of the high absorbance; transmitted light was too faint to detect.

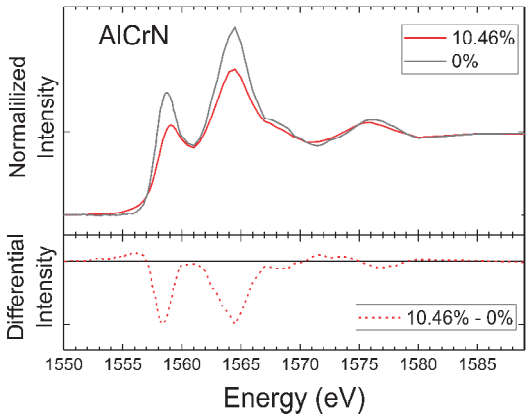

Fig. 2. Al *K*-edge XANES spectra of AlN and AlCrN (10.46%) films on SiO_2 substrates. The lower panel is differential spectra of AlCrN and AlN.

[1] A. Luque *et al.*, Phys. Rev. Lett. **78** (1997) 5014.
[2] S. Sonoda, Appl. Phys. Lett. **100** (2012) 202101.
[3] N. Tatemizo *et al.*, J. Phys.: Condens. Matter **29** (2016) 085502.
[4] E. Ruiz *et al.*, Phys. Rev. B **49** (1994) 7115.

BL2A

Evaluation of Local Structures of P for $CePO_4$

A. Nakahira[1, 2], M. Togo[1], T. Minami[1], C. Takada[1], M. Matsumoto[1], M. Iida[1] and H. Aritani [3]
[1]*Faculty of Engineering, Osaka Prefecture University, Sakai 599-8531, Japan*
[2]*Trans-Regional Corporation Center for Industrial Materials Research (IMR), Tohoku University, Sakai 599-8531, Japan*
[3]*Saitama Institute of Technology, Fukaya 369-0293, Japan*

In recent years, the research about rare earth phosphate materials with unique electronic transition are active for various application as magnetic materials, catalysts, and high performance luminescent devices etc. In special, much interest has been focused on the synthesis and luminescence of nano-sized rare earth orthophosphates for their potential application in optoelectronic devices and biological fluorescence labeling device. Among them, $CePO_4$ nanoparticles and nanowires have been expected to be used as luminescent probe for selective sensing. $CePO_4$ is one of quite unique rare earth phosphate material, hexagonal $CePO_4$ and monoclinic $CePO_4$ (natural monazite). In special, the development and research on nano-sized $CePO_4$ material (nanorods, nanowires, and nanofiber etc) with a variable size attract much attention. For example, monoclinic $CePO_4$ generally exists as natural monazite, bulk materials of which could be prepared via the solid state reaction and hydrothermal method at high temperature. In this study, the purpose was to evaluate the local structure of $CePO_4$ synthesized by hydrothermal process at 423 K and soft chemical process at room temperature. The effect of synthetic condition parameters (synthesis processing, temperature, time, aging etc) on the microstructure for various $CePO_4$ samples was investigated.

All chemicals were analytical reagent- grade, and they used without further purification. In a typical synthesis, $Ce(NO_3)_3$ solution with 0.05 mol/L concentrations were prepared. Into them, the cerium nitrate solution was added slowly to 6 mol/L of orthophosphoric acid solution while kept under stirring. The as-obtained solution with a different reactant PO_4/Ce molar ratio was transferred into a stainless steel autoclave with an inner teflon vessel (28 ml). And the hydrothermal treatment was carried out at 423 K for 24 h. Furthermore, the soft chemical process was done at 358 K and room temperature using the same chemical solutions as hydrothermal treatments. After hydrothermal process and soft chemical process, the as-synthesized precipitates were separated by filtration, washed with deionized water several times and ethanol, and dried at 343 K for 12 h. After drying, the products were ground with Al_2O_3 mortal. The final products appeared as light green solid powder. After all of the ground product powders were characterized by XRD method, FT-IR and TG-DTA. The microstructures of product powder were observed by SEM. The local structures around Si for the products of samples were characterized by measuring X-ray adsorption near edge structure (XANES) at BL02A in UV-SOR.

The evaluation of XRD done for various products. According to XRD results, products prepared by hydrothermal process at 423K was mainly composed of hexagonal $CePO_4$, although ones by soft chemical process at 358 K and room temperature were composed of monoclinic $CePO_4$. Figure 1 shows the XANES spectra of various $CePO_4$ samples. As shown in Fig. 1, XANES spectra of sample obtained by hydrothermal process and soft chemical process were quite different. Furthermore, there was slight difference for $CePO_4$ samples by soft chemical process at between 358 K and room temperature. In addition, the effect of synthetic condition parameters (processing, temperature, and PO_4/Ce on the microstructure for various $CePO_4$ samples was confirmed.

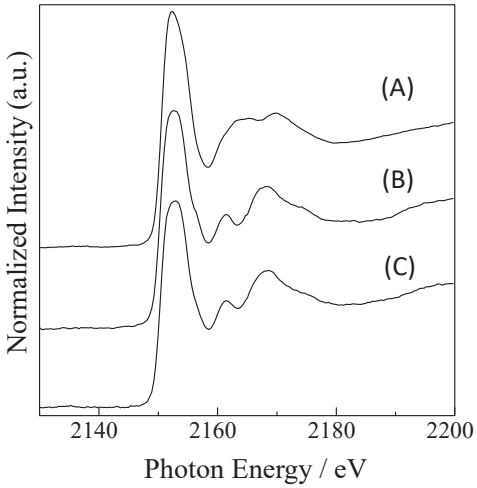

Fig. 1. P-*K* XANES spectra of various $CePO_4$ samples. (a) hydrothermal process at 423 K, (b) soft chemical process at 358 K and (c) soft chemical process at room temperature.

BL2B

Ultraviolet Photoelectron Spectra of $Lu_2@C_{90}$

T. Miyazaki[1], K. R. Koswattage[2], H. Shinohara[3] and S. Hino[4]

[1]*Faculty of Science, Research Laboratory for Surface Science, Okayama University, Okayama 701-8530, Japan*

[2]*Institutes for Molecular Science, Okazaki 444-858, Japan*

[3]*Graduate School of Science, Nagoya University, Nagoya 464-8602, Japan*

[4]*Graduate School of Science and Engineering, Ehime University, Matsuyama 790-8577, Japan*

The synthesis and separation of higher fullerenes and endohedral fullerenes are remarkable results brought by the investigation of the structure and the electronic structure. Until now, there have been a lot of attempts to synthesize and isolate endohedral fullerenes contains mono-metal atom, di-metal atoms, metal nitrides and metal–carbon clusters. This encapsulation modifies the electronic structure of the fullerene cage by changing the encapsulated atom(s). We have succeeded to measure ultraviolet photoelectron spectra (UPS) of Lu encapsulated C_{82} fullerenes: $Lu@C_{82}$, $Lu_2@C_{82}$, $Lu_2C_2@C_{82}$ [1]. In the current report, the UPS of $Lu_2@C_{90}$ will be presented.

The UPS of the endohedral fullerene were measured using a photoelectron spectrometer at BL2B of UVSOR. Energy calibration of the spectra was carried out using the Fermi edge of a gold-deposited sample disk before the UPS measurements of $Lu_2@C_{90}$. All spectra were normalized by the peak height of the structure α.

Figure 1 shows the UPS of $Lu_2@C_{90}$ obtained with hν = 25–55 eV. The spectral onset of $Lu_2@C_{90}$ was 0.99 eV below the Fermi level, which was much smaller than that of empty C_{90} (1.23 eV), which means encapsulation of metal atom inside the cage contribute to narrow the band gap of fullerene, but $Lu_2@C_{90}$ is still semi-conductive. There are 10 structures labeled A–D, α–δ, X and Y in the UPS of $Lu_2@C_{90}$. The intensity of these structures changed, when the incident photon energy was tuned, which was a typical behavior of fullerenes. From the UPS comparison of the other endohedral fullerenes, their structures α–δ appeared in the deeper binding energy region (E_b > 5 eV) of the UPS of $Lu_2@C_{82}$ is due to σ-electrons that constitute the C_{90} skeletal C–C bonds. Structures labeled A–D appeared in the upper binding energy region (E_b < 5 eV) of the UPS are derived from π-electrons. On the other hand, there are two structures X and Y in the 9–11 eV region. They are not observed when the incident photon energy is less than 35 eV, but they are distinct and their intensity becomes stronger in accordance with the increase of the incident photon energy. This behavior is quite different from that of other endohedral fullerenes and seems to be the characteristic ones to the entrapped Lu atom [1]. Possibly structures X and Y is due to $Lu4f_{7/2}$ and $Lu4f_{5/2}$. The ionization potentials of Lu $4f_{7/2}$ and $4f_{5/2}$ of Lu metal are 7.5 eV and 8.9 eV, respectively [2]. Structures X and Y of $Lu_2@C_{90}$ appear at 9.8 eV and 11.2 eV, respectively, which are higher than those of Lu metal by 2.3 eV. Lu atom is electron wanting state. Hence the ionization potential of entrapped Lu 4f levels moves to deeper level. Thus, the entrapped Lu atom donates electrons to the cage and the oxidation state of Lu atom might be +3.

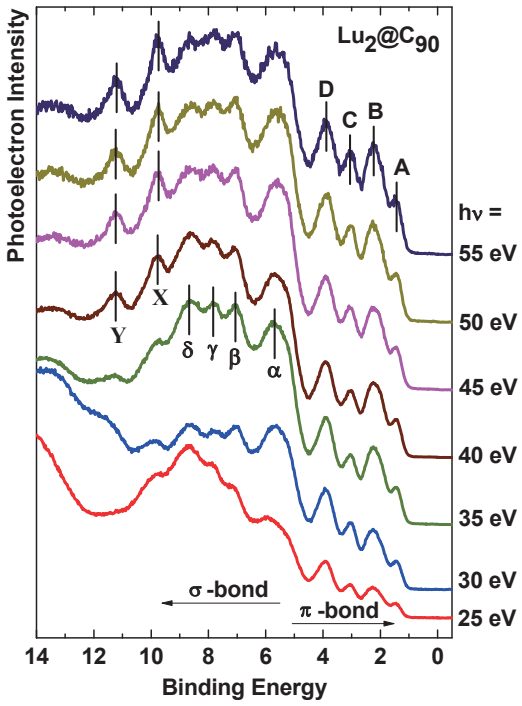

Fig. 1. The incident photon energy dependent UPS of $Lu_2@C_{90}$ at *hν* = 25–55 eV.

[1] T. Miyazaki, R. Sumii, H. Umemoto, H. Okimoto, T. Sugai, H. Shinohara and S. Hino, CPL **555** (2012) 222.

[2] M. Cardona and L. Ley (Eds.), Photoemission in Solids. I: General Principles, Springer-Verlag, Berlin, 1978.

BL3B

Radiative Decay of Intrinsic Luminescence from Self-Trapped Excitons in Orthoborates with Plural Nonequivalent BO_3^{3-} Groups upon VUV Excitation

N. Kodama, H. Kubota, M. Kudo and T. Takahashi
Graduate School of Engineering Science, Akita University, Akita 010-8502, Japan

The electronic structure of complex oxoanions, such as BO_3^{3-}, PO_4^{3-}, and SiO_4^{4-}, is expected to exhibit peculiar features. Until now, there has been very little work focusing on statistical fluctuations in the local structure of low-symmetry complex rare-earth oxides with plural nonequivalent oxoanions of the BO_3^{3-} group. We focused on three types of orthoborates with different numbers of nonequivalent BO_3^{3-} oxoanion groups. The first type includes $YSc(BO_3)_2$ (YSB) [1] and $Sr_6YSc(BO_3)_6$ (SYB) with one BO_3^{3-} group; these crystals are characterized by a statistical fluctuation in the local structure surrounding BO_3^{3-} groups caused by disorder of Y^{3+} and Sc^{3+} ions. The second type consists of rare-earth orthoborate crystals, such as $LaSc_3(BO_3)_4$ (LSB) [1] and $Ca_4LaO(BO_3)_3$ (CLOB), with two nonequivalent BO_3^{3-} groups. CLOB belongs to a class of double borates with oxygen as a foreign anion. The third type is $Ba_3Y(BO_3)_3$ (BYB) with three nonequivalent BO_3^{3-} groups.

We report on intrinsic luminescence spectra and decay characteristics of STEs in these crystals. In addition, we discuss the correlation between intrinsic luminescence bands associated with STEs and the number of nonequivalent BO_3^{3-} groups in YSB, SYB, LSB, CLOB, and BYB, from the viewpoint of the local structure, symmetry, and environment of BO_3^{3-} groups.

Luminescence and excitation spectra of STEs in YSB, SYB, LSB, CLOB, and YSB polycrystals were measured at twelve temperatures in the range of 8(11)-293 K using the undulator beamline BL3B at the UVSOR facility. The decay characteristics of the luminescence on the nanosecond scale were measured using a time corrected single photon counting method under excitation with single bunched pulses from UVSOR. The excitation spectral intensity for the orthoborates increased rapidly below about 200-210 nm. The broad excitation bands were assigned to bandgap excitations or molecular transitions of the BO_3^{3-} group. All samples were found to exhibit multiple STE luminescence bands in the UV region under VUV excitation at 70 and 160 nm.

The luminescence spectra of YSB and SYB at 11 and 8 K, respectively, consisted of two broad bands associated with STE(I) and (II) with peaks at 251 and 274 nm, and 288 and 337 nm. The spectra of LSB and CLOB at 11 K consisted of two broad bands with peaks at 245 and 303 nm, and 281 and 364 nm, respectively, again associated with STE(I) and STE(II) in two sets of nonequivalent BO_3^{3-} groups. On the other hand, as shown in Fig. 1(e), BYB exhibited three distinct broad bands at 8 K: an intense luminescence band with a peak at 306 nm, a short-wavelength shoulder with a peak at 246 nm, and a band with a long-wavelength tail and a peak at 389 nm. These three intrinsic bands are assigned to STE(I), STE(II), and STE(III) in three sets of nonequivalent BO_3^{3-} groups. In LSB, CLOB, and BYB, the number of intrinsic luminescence bands coincides with the number of nonequivalent BO_3^{3-} groups, whereas in YSB and SYB two bands appear, despite the presence of only one BO_3^{3-} group. The number of bands is inconsistent with the number of nonequivalent BO_3^{3-} groups. A possible interpretation for this discrepancy is that there are two types of BO_3^{3-} groups with different geometries, presumably caused by random disorder of Y^{3+} and Sc^{3+} ions.

Figures 1(a)-(f) show decay curves for the UV bands at 8 K for YSB, LSB, CLOB, and BYB, respectively. All samples exhibit a fast and a slow component due to high-spin and low-spin STEs associated with the two possible spin orientations for the exciton electron-hole pair of alkali halides [1]. For YSB, the decay times for STE(I) luminescence at 240 nm are 350 ps and 4.3 μs. For LSB, the decay times for STE(I) luminescence at 260 nm are 1.2 ns and 184 ns, and those for STE(II) at 330 nm are 1.8 ns and 180 ns. For CLOB, the decay times for STE(I) luminescence at 270 nm are 1.7 ns and 2.0 μs, and those at 400 nm for STE(II) are 2.0 ns and 2.0 μs. For BYB, the decay times for STE(I) luminescence at 400 nm are 1.7 ns and 2.0 μs.

The fast decay components for STE(I) in YSB and BYB originate from singlet STE states in BO_3^{3-} groups with D_3 and Cs symmetry, respectively. The fast decay components for STE(I) and STE(II) in LSB and CLOB may also originate from singlet STE states the BO_3^{3-} groups with C_1 and Cs symmetry, respectively. In contrast, the slow decay components for STE(I) in YSB, LSB, CLOB, and BYB, and those for STE(II) in LSB and CLOB are attributed to triplet STEs in BO_3^{3-} groups in which singlet STE states occur.

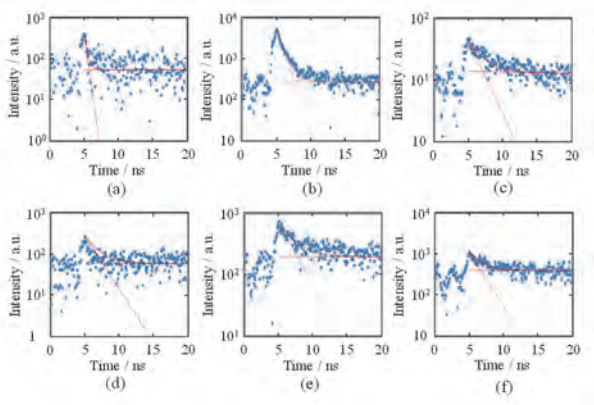

Fig. 1. Decay curves for STE luminescence at 8 K at (a) 240 nm for YSB, (b) 260 nm for LSB, (c) 330 nm for LSB, (e) 270 nm for CLOB, (e) 400 nm for CLOB, and (f) 400 nm for BYB.

[1] N. Kodama, K. Yanagidaira and T. Takahashi, UVSOR Activity Report **43** (2016) 53.
[2] T. T. Williama and K. S. Song, J. Phys. Chem. Solds. **51** (1990) 679.

BL3B

Excitation Process of Pr^{3+} Ions in $Lu_3Al_5O_{12}$ Crystals by VUV Photons

M. Kitaura[1], K. Kamada[2], S. Kurosawa[1, 2] and A. Ohnishi[1]
[1]*Faculty of Science, Yamagata University, Yamagara 990-8560, Japan*
[2]*New Industry Creation Hatchery Center, Tohoku University, Sendai 980-8579, Japan*

The impact excitation of hot photocarriers with impurity-localized electrons in crystalline solids has been studied with the use of synchrotron radiation (SR) [1]. Since a number of relaxation pathways compete under excitation with vacuum ultraviolet (VUV) photons from SR, the relaxation of hot photocarriers becomes complicated. The process of impurity-excitation by VUV photons still remains obscure, despite the basic subject concerning both sides of fundamental and applied physics.

The crystal of praseodymium-doped $Lu_3Al_5O_{12}$ (Pr:LuAG) has been utilized as the scintillator for the detection of X- or γ-rays. VUV excitation spectra for the Pr^{3+} 5*d*-4*f* luminescence in Pr:LuAG crystals have been reported [2, 3]. However, the process of Pr^{3+}-excitation by VUV photons has not been discussed in detail. The information on this process provides us hints to obtain high-quality Pr:LuAG scintillators.

The main aim of the present study is to clarify the processes of electron-hole (*e*-*h*) relaxation in undoped LuAG crystals and Pr^{3+}-excitation in Pr:LuAG crystals. The undoped LuAG and Pr:LuAG crystals were grown by the micro pulling down (μ–PD) method. The concentration of Pr^{3+} ions was set 0.8 mol%. In the present experiment, we measured excitation spectra for the excitonic luminescence peaking at 4.96 eV and the Pr^{3+} 5*d*-4*f* luminescence at 3.87 eV. The data were corrected for the distribution of excitation light source.

Figure 1 shows excitation spectra for the excitonic luminescence (blue line) and Pr^{3+} 5*d*-4*f* luminescence (red line). The fundamental absorption edge of undoped LuAG crystals was determined around 6.83 eV. The excitonic luminescence is excited in the region above the fundamental absorption edge. The intensity is almost kept constant in the 11-18 eV range, and it is gradually increased in the 18-26 eV range. The threshold energy is higher than the sum of the lowest exciton creation energy (6.83 eV) and the band-gap energy (7.93 eV [4]). In this case, hot photoelectrons have the kinetic energies enough to excite valence electrons into the conduction band minimum through inelastic scattering with them. Consequently, it is most likely that the multiplication of electronic excitations (MEEs) is realized above 18 eV. In order to obtain more detail information on the process of the MEEs, ultraviolet photoemission experiment are now in progress.

The Pr^{3+} 5*d*-4*f* luminescence is excited in the region below the fundamental absorption edge, in which the Pr^{3+} 4*f*-5*d* absorption occurs. In the region above the fundamental absorption edge, the excitation spectrum for the Pr^{3+} 5*d*-4*f* luminescence is similar to that for the excitonic luminescence mentioned above. This result indicates that no direct (elastic) excitation of Pr^{3+} ions by hot photoelectrons occurs in Pr:LuAG crystals. One may notice the spectral overlap between the excitonic luminescence and Pr^{3+} 4*f*-5*d* absorption, implying the energy transfer from the host to Pr^{3+} ions. However, the Pr^{3+} 5*d*-4*f* luminescence is observed under excitation above the fundamental absorption edge, even when the excitonic luminescence is completely quenched at 300 K. This fact excludes the possibility of the energy transfer from the host to Pr^{3+} ions. Thus, the following process is most suitable for the Pr^{3+}-excitation by VUV photons. The *e*-*h* pairs created under MEEs are captured by Pr^{3+} ions, and the excited states of Pr^{3+} ions are formed. The excited states relax into the ground states, giving rise to the Pr^{3+} 5*d*-4*f* luminescence.

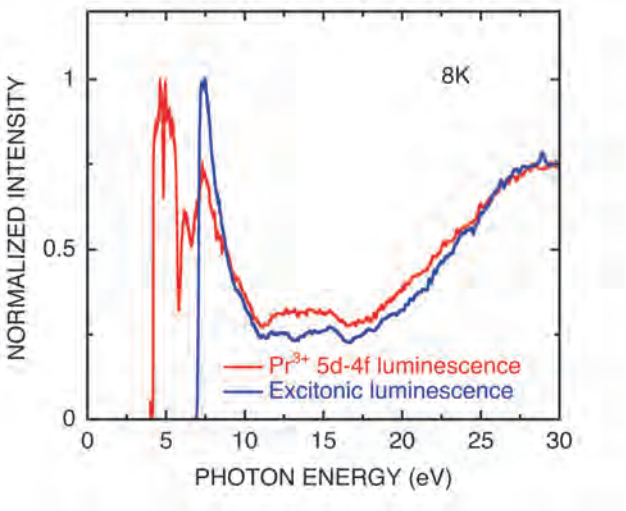

Fig. 1. Excitation spectra for the 4.96 eV (blue line) and 3.87 eV bands (red line). These data were obtained at 8 K. The former and latter correspond to the excitonic luminescence and Pr^{3+} 5*d*-4*f* luminescence, respectively.

[1] For example, M. Kitaura *et al*., J. Lumi. **172** (2016) 243.
[2] A. Yoshikawa *et al*., IEEE Tran. Nucl. Sci. **55** (2008) 1372.
[3] Y. Zorenko *et al.,* J. Lumi. **179** (2016) 496.
[4] P. Dorenbos, J. Lumi. **134** (2013) 310.

BL3B

Effects of Annealing and Mg-codoping on Luminescence Properties of Ce Doped Garnet-Based Scintillator Grown by Micro Pulling Down Method

H. Yamaguchi[1], K. Kamada[2, 3], S. Kurosawa[3], Y. Shoji[1, 2], Y. Yokota[3], Y. Ohashi[1], A. Yamaji[1] and A. Yoshikawa[1, 2, 3]

[1] *Tohoku University, Institute for Materials Research, Sendai 980-8577, Japan*
[2] *C&A Corporation, T-Biz, Sendai 980-8579, Japan*
[3] *Tohoku University, New Industry Creation Hatchery Center, Sendai 980-8579, Japan*

Recently, cations (B, Ca, Ba) codoping effects on scintillation mechanism and annealing effects on defect structures for Ce: $Gd_3Ga_3Al_2O_{12}$ (GGAG) has been reported [1], where further improvement of scintillation properties were also reported. In addition, Mg^{2+} codoping effects on shallow electron traps for Ce:GGAG by the UV-induced absorption spectroscopy against the thermoluminescence (TL) glow curve was reported [2]. In this study, we investigated the Mg codoping effect on the shallow traps of defect complexes related to oxygen vacancies for the multicomponent garnet-based scintillators by measuring the TL glow curves.

We prepared Mg codoped and non codoped Ce:$(Lu,Gd)_3Ga_3Al_2O_{12}$ single crystals grown by the micro-pulling-down method, and TL spectra for these samples were measured and evaluated within 7.5-300 K at BL3B of the UVSOR facility. The size and weight of each crystal were similar and the TL glow curves were normalized to the background intensity.

Figure 1 (a) - (b) show the TL glow curves for the Mg/non codoped Ce:$(Lu,Gd)_3Ga_3Al_2O_{12}$ single crystals under 210-190 nm excitation in the temperature range of 7.5-300K. Since absorption edge shifted from 210 nm to approximately 190 nm with increasing the Lu concentration, the 210-190 nm photons were selected as an exaction source accordingly.

2 or 3 glow peaks were observed in this temperature range of TL glow curves, which difference is most probably due to the difference of Ce concentration in the grown crystals. It was also found that the peak intensity around 300 K relatively strengthened with increasing the Lu concentration. Moreover, in case of high Lu concentrated crystals (x = 3), its intensity around 300 K significantly weakened by Mg codoping. Therefore, these results implies that Mg codoping affected the suppression of electron traps effectively in the higher Lu concentrated crystal.

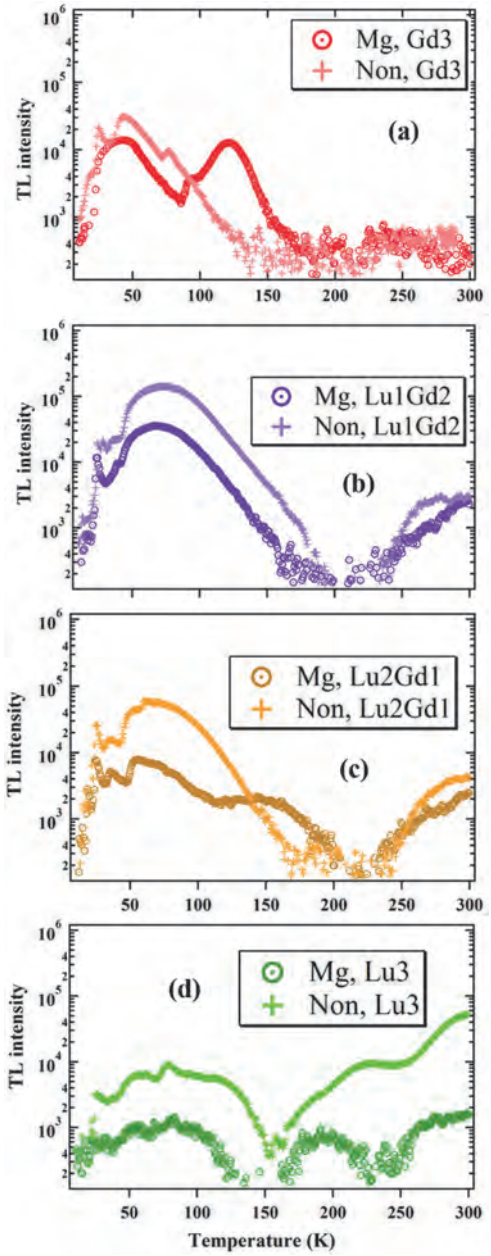

Fig. 1. The TL glow curves of Mg/non codoped Ce:$(Lu_xGd_{3-x})Ga_3Al_2O_{12}$ single crystals; (a) x = 0, (b) x = 1, (c) x = 2, (d) x = 3.

[1] M. Tyagi *et al.*, J. Phys. D; Appl. Phys. **46** (2013) 475302.
[2] M. Kitaura *et al.*, Applied Physics Express **9** (2016) 072602.

BL3B

Determination of the Bandgap Energy of Gd Admixed $Lu_2Si_2O_7$ Scintillator Crystals Using the UVSOR Facility

T. Horiai[1], S. Kurosawa[2, 3], A. Yamaji[1], H. Chiba[1], S. Kodama[1], Y. Shoji[1, 4], Y. Ohashi[1], K. Kamada[2, 4], Y. Yokota[2], A. Yoshikawa[1, 2, 4] and M. Kitaura[3]

[1]*Institute for Materials Research, Tohoku University, Sendai 980-8577, Japan*
[2]*New Industry Creation Hatchery Center, Tohoku University, Sendai 980-8579, Japan*
[3]*Department of Physics, Yamagata University, Yamagata 990-8560, Japan*
[4]*C&A Corporation, Sendai 980-8579, Japan*

Scintillator is a material that converts ionizing radiation such as alpha-rays, gamma-rays and X-ray to a visible/UV lights, and can be applied in oil well logging, high energy physics and nuclear medicine [1, 2]. Especially, pyrosilicate type scintillator, for example Ce-doped $Lu_2Si_2O_7$ (Ce:LPS), Ce-doped $Gd_2Si_2O_7$ (Ce:GPS) and Ce-doped (Gd, La)$_2Si_2O_7$ (Ce:La-GPS) were promising materials with high light output, fast scintillation decay and stable light output until high temperature (150ºC) [3-5]. These scintillation properties were good for application in oil well logging, where the scintillator is often exposed to high temperatures (~200ºC) under Earth surface.

Ce:GPS has been found to melt incongruantly, and therefore it could not be grown by conventional techniques from the melt [6]. On the other hand, the composition of Ce:LPS melts congruently and can be grown relatively easily [7]. Although Ce:LPS has large intrinsic gamma-rays background due to ^{176}Lu.

In this study, we focused on the Gd admixed Ce:LPS, because Gd is good constituents for the material without intrinsic background when compared to Lu, and estimated the bandgap energy of Gd admixed $Lu_2Si_2O_7$ scintillator crystals.

We prepared undoped $Lu_2Si_2O_7$ (LPS) and ($Lu_{0.95}$ $Gd_{0.05}$)$_2Si_2O_7$ (LPSGd5%)single crystals grown by the micro-pulling-down method, and UV absorption edge for these samples were evaluated with a photo diode (IRD, AXUV 100) at BL3B of UVSOR. The bandgap energies were calculated from the UV absorption edge.

We succeeded in growing the transparent samples by the μ-PD method (Fig. 1). From the result of the powder X-ray diffraction analysis, the crystal phase of these samples matched the previous result on LPS (JCPDS No. 35-0326). In addition, the crystalline structure of these crystals were determined to be monoclinic with space group of *C*2/*m*.

Figure 2 shows the UV absorption spectra, and the significant change due to Gd admixed was not observed. From this figure, the UV absorption edge wavelength were around 178 nm. The bandgap energy of LPS and LPSGd5% were calculated about 6.96 and 6.95 eV, respectively. Thus, the bandgap energy of LPSGd5% was remained high value, and this result suggested temperature dependence of light output was also good.

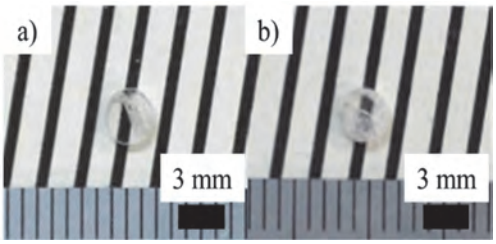

Fig. 1. Photograph of after polished samples, (a) $Lu_2Si_2O_7$, (b) ($Lu_{0.95}$ $Gd_{0.05}$)$_2Si_2O_7$.

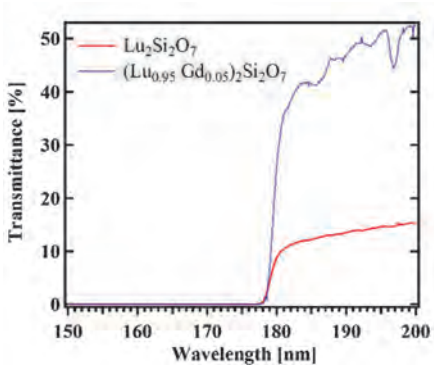

Fig. 2. UV absorption spectra.

[1] C.L. Melcher, J.S. Schweitzer, R.A. Manente and C.A. Peterson, J. Crystal Growth **109** (1991) 37.
[2] C.L. Melcher, J. Nuclear Medicine **41** (2000) 1051.
[3] L. Pidol, A. Kahn-Harari, B. Viana, E. Virey, B. Ferrand, P. Dorenbos, J.T.M. de Haas and C.W.E. van Eijk, IEEE Trans. Nucl. Sci. **51** (2004) 1084.
[4] S. Kawamura, J.H. Kaneko, M. Higuchi, T. Yamaguchi, J. Haruna, Y. Yagi, K.susa, F. Fujita, A. Homma, S. Nishiyama, K. Kurashige, H. Ishibashi and M. Furusaka, IEEE Trans. Nucl. Sci. **54** (2007) 1383.
[5] S. Kurosawa, T. Shishido, T. Sugawara, A. Nomura, K. Yubuta, A. Suzuki, R. Murakami, J. Pejchal, Y. Yokota, K. Kamada and A. Yoshikawa, Nucl. Instrum. Methods Phys. Res. A **772** (2015) 72.
[6] N.A. Toropov, F.Y. Galakhov and S.F. Konovalova Russ. Chem. Bull. **10** (1961) 497.
[7] A.N. Christensen, Zeitschrift fur Kristallographie **209** (1994) 7.

BL3B

Temperature Dependence of Luminescent Properties for Un-doped Cs_2HfCl_6

S. Kodama[1], S. Kurosawa[2, 3], A. Yamaji[1], J. Pejchal[4], R. Král[4], Y. Ohashi[1], K. Kamada[2, 5], Y. Yokota[2], M. Nikl[4] and A. Yoshikawa[1, 2, 5]

[1] *Institute for Materials Research (IMR), Tohoku University, Sendai 980-8577, Japan*
[2] *New Industry Creation Hatchery Center (NICHe), Tohoku University, Sendai 980-8579, Japan*
[3] *Faculty of Science, Yamagata University, Yamagata 990-8560, Japan*
[4] *Institute of Physics, CAS, Cukrovarnická 10, 162 00 Prague, Czech Republic*
[5] *C&A Corporation, Sendai 980-8577, Japan*

Halide scintillation materials are expected to have high light output due to smaller band gap energy than that for the oxide materials [1]. Indeed, Tl:NaI [2,3], Ce:$LaBr_3$ [4] and Eu:SrI_2 [5] have good light output. However, almost all halide materials have strong hygroscopic nature. Although these scintillators are packed in a hermetic sealing, aging degradation would be caused by remaining moisture in the package or damage of the package.

Recently, a non-hygroscopic halide material, Cs_2HfCl_6, was reported by Burger *et al.* [6], and this material has a high light output of 54,000 photons/MeV and good energy resolution of around 3 % (FWHM for 662 keV gamma-ray). Moreover, Cs_2HfCl_6 emits ~440 nm blue light under ~250 nm excitation [7]. This emission is considered to be of Zr-related defect origin while the other component of emission spectra located within 360-400 nm comes from self-trapped exciton (STE) luminescence on $[HfCl_6]^{2-}$ anion complex [8]. However, the details of its luminescence mechanism have not been investigated yet. Here, we investigated temperature dependence of photoluminescence spectra for undoped Cs_2HfCl_6.

Un-doped Cs_2HfCl_6 were synthesized from 99.9%-pure (Zr-free) $HfCl_4$ and 99.999%-pure CsCl. Then, the mixed powders were put into a quartz-glass ampoule and the crystal was grown by the vertical Bridgman growth method. The procedure is in detail described in [9].

The obtained single crystal was cut and polished to measure its photoluminescence spectra. We evaluated the temperature dependence in BL3B beamline at UVSOR. Cs_2HfCl_6 was excited by 250 nm UV light, and spectra were measured with a spectrometer (spectoropro-300i, Acton research). The chamber was cooled by liquid helium, and the spectra were measured from 8 to 300 K.

We succeeded in growing the undoped Cs_2HfCl_6 single crystal. Obtained photoluminescence spectra at 8, 100, and 300 K for Cs_2HfCl_6 are shown in Fig. 1. The intensity of luminescence decreased with decreasing temperature. We summarized the intensity versus temperature of undoped Cs_2HfCl_6 in Fig.2. In addition, emission peak shifted from 454 nm (at 300 K) to 441 nm (at 6 K). Given the fact that under 250 nm excitation rather Zr-impurity related defect emission peaking around 435 nm is excited at room temperature [7] the temperature dependence measured here is related to the same defect rather than to STE..

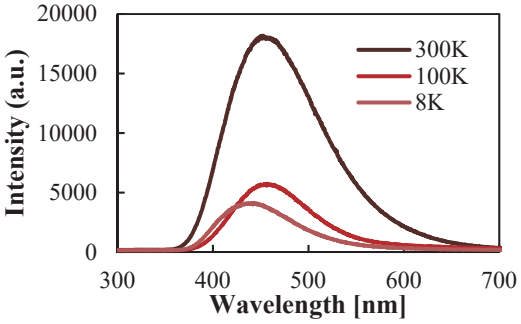

Fig. 1. Photoluminescence spectra of Cs_2HfCl_6 at 300, 100 and 6 K.

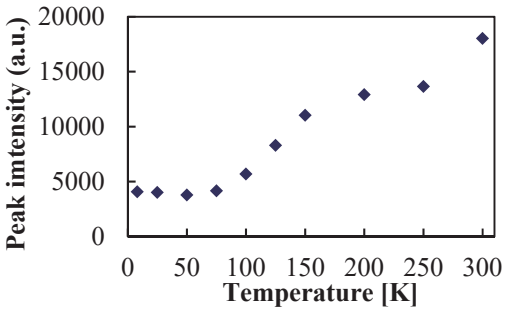

Fig. 2. Temperature dependence of emission intensity obtained as peak position at 454 nm From Fig. 1.

[1] P. Dorenbos, NIM**A486** (2002) 208.
[2] E. Sakai, IEEE TNS **1** (1987) 418.
[3] Bicron Co., physical properties of common inorganic scintillators (2001) 3101.
[4] E.V.D. van Loef *et. al.*, NIM**A486** (2002) 254.
[5] Y. Yokota *et. al.*, JCG **375** (2013) 49.
[6] A. Burger *et. al.*, App. Phys. Lett. **107** (2015) 143505.
[7] K. Saeki *et al.*, Appl. Phys. Ex. **9** (2016) 042602.
[8] B. Kang *et al.*, J. Phys. Chem. C **120** (2016) 12187.
[9] S. Kodama *et al.*, J. Lumin. in prep.

BL3B

Evaluation of Ce:$(Gd, La)_2Si_2O_7$ Scintillator Using an UVSOR Beam Line -FY2016-

S. Kurosawa[1, 2], A. Yamaji[3], T. Horiai[3], S. Kodama[3], T. Chiba[3], C. Tanaka[3], Y. Shoji[3, 4], Y. Ohashi[3], Y. Yokota[1], K. Kamada[1, 4], A. Yoshikawa[1, 3, 4] and M. Kitaura[2]

[1] *New Industry Creation Hatchery Center (NICHe), Tohoku University, Sendai 980-8579, Japan*
[2] *Faculty of Science, Yamagata University, Yamagata 990-8560, Japan*
[3] *Institute for Materials Research (IMR), Tohoku University, Sendai 980-8577, Japan*
[4] *C&A Corporation, Sendai 980-8577, Japan*

Scintillators are used in various fields such as medical imaging, astronomy, oil well ligging and so on. Recently, scintillation properties of $(Ce_{0.01}, Gd_{0.90}, La_{0.09})_2Si_2O_7$ (Ce:La-GPS) have been reported. The Ce:La-GPS crystal had a light output of approximately 35,000 photons/MeV, FWHM energy resolution of 5.0% at 662 keV [1, 2]. Moreover, the light output over 35,000 photons/MeV was found constant in the temperature range from 0 to 423 K. In addition, FWHM energy resolution of Ce:La-GPS (roughly 7–8%) at 662 keV remained constant up to 373 K [3]. Thus, this crystal can be applied to oil well logging or other radiation detection application at high temperature conditions.

Up to now, the bandgap energy of La-GPS has been not measured for La-GPS yet. In order to reveal the mechanism of the thermal quenching, the evaluation of the bandgap energy is required. Thus, in this paper, the bandgap energy was measured at low temperature (7K) using UVSOR beam line BL3B.

To evaluate the bandgap energy, pure La-GPS was prepared by the micro-pulling down method. Using this sample and the BL3B, we measured the transmittance spectrum as showin in Fig. 1. From this data, the band gap energy was estimated to be 7.13±0.01 eV. Compared with other oxide scintillators, La-GPS was found to have wider bandgap. On the other hand, the light output of Ce:La-GPS was larger than most of oxide scintillators with narrower bandgaps than La-GPS.

Light output (light yield Y) was related to bandgap energy (E_{gap}) in following equation:

$$Y = \frac{\eta E \gamma S Q}{\beta E_{gap}} \quad (0 < \eta, Q, S \leq 1),$$

where S, Q, E_γ and β are the transfer efficiency from the electron-hole pair into the luminescence center, the quantum yield of the final luminescence process in Ce^{3+} emission center, incident gamma-ray energy and the ratio between the energy needed to create one electron-hole pair and E_{gap} [4]. Usually β is used as constant (~2.5) , and η denotes generation coefficient for electron-hole pair. The value of $\eta \times S \times Q$ for Ce:La-GPS was found to be higher than for the other scintillators.

The quantum yield (Q) of Ce:-LaGPS was estimated to be around 0.8 using an integrating sphere and a spectrometer (Hamamatsu C9920-02G), and this is similar value to other oxide scintillator, where typical value of Q for oxide conventional scintillator is 0.6-0.8. Thus, it implies that Ce:La-GPS has good transfer efficiency or/and good electron-hole pair generation efficiency.

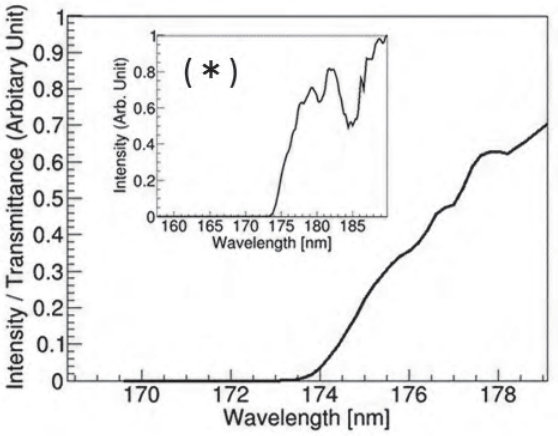

Fig. 1. Transmittance of pure La-GPS as function of wavelength. The small window marked (*) denotes enlarged view arond the absorption edge.

[1] A. Suzuki *et al.*, Applied Physics Express **5** (2012) 102601.
[2] S. Kurosawa *et al.*, Nucl. Inst. and Meth. in Phys. Res. **A774** (2014) 30.
[3] S. Kurosawa *et al.*, Nucl. Inst. and Meth. in Phys. Res. **A772** (2015) 72.
[4] R. H. Bartrama and A. Lempicki, 1996 Journal of Luminescence **68** (1996) 225.

BL3B, BL7B

Temperature Dependence of the PL Spectra of Laser Irradiated *a*-CN_x Thin Films

K. Nakamura[1], F. Sawa[1], K. Fukui[1] and K. Yamamoto[2]
[1]*Department of Electrical and Electronics Engineering, University of Fukui, Fukui 910-8507, Japan*
[2]*Far-infrared region Development Research Center, University of Fukui, Fukui 910-8507, Japan*

Amorphous carbon nitride (*a*-CN_x) is known to have interesting mechanical, electrical and optical properties. In the optical properties, *a*-CN_x shows a broad emission at visible region. Since *a*-CN_x is composed only of carbon and nitrogen, it is expected as an inexpensive white light emitting material. However, photoluminescence (PL) spectra of the samples evaporated under same conditions are, in some cases, different with each other, because the optical properties of *a*-CN_x are sensitive to the preparation conditions. Recently, it is found that laser irradiated *a*-CN_x thin films in the atmosphere after depositing show much higher PL intensity than those of as-deposited *a*-CN_x thin films, and their PL spectra have better reproducibility [1, 2]. In this report, we show temperature dependence of the PL spectra by using laser irradiated *a*-CN_x thin films.

All samples on Si substrates are deposited by the RF-sputtering method at Ryukoku University [1]. The sputtering conditions of the graphite target in each sample under low pressure nitrogen gas environment were kept constant, and the RF power was changed to 40 W, 60 W and 100 W. Beam diameter of laser-irradiation is about 1.2 mm, and irradiation time is 240 minutes by using He-Cd laser (325 nm) with 20 mW. All PL measurements have been performed at BL3B and BL7B from 10 to 320 K. The excitation energy of PL measurements is fixed at 4.6 eV, where excitation spectra of all samples have maximum intensities.

Figure 1 shows the PL spectra of RF power 60 W *a*-CN_x thin film at from 10 K to 320 K. It is found that a broad PL is observed from 1.6 to 4.0 eV, and broadness is independent on temperature. However, PL intensity gradually decreases with increasing temperature, and the peak energy of PL spectrum gradually shifts to the higher photon energy side with increasing temperature. These trends are also observed in both 40 W and 100 W *a*-CN_x thin films. They suggest that the relaxation mechanism of PL in *a*-CN_x thin films does not change at least below room temperature. However, both peak shift and intensity decreasing reveal that this broad PL peak consists of many emission bands, which are continuously distributed from 1.6 eV to 4.0 eV [2].

Figure 2 shows temperature dependence of the normalized PL intensity of 60 W *a*-CN_x at emission photon energy 2.43, 2.50, 2.55, 2.65, 2.76, 2.89, 2.97, 3.05 eV, respectively. Intensity normalization carried out to the intensity at 10 K. Temperature dependences show roughly similar with each other and relatively simple behavior, although it is difficult to explain this behavior as the resulting from single thermal quenching mechanism.

In summary, we measured temperature dependence of PL spectra of laser irradiated *a*-CN_x thin films. The *a*-CN_x thin films show a broad visible range emission band, which consist of various emission bands. However, their thermal quenching mechanisms are relatively simple.

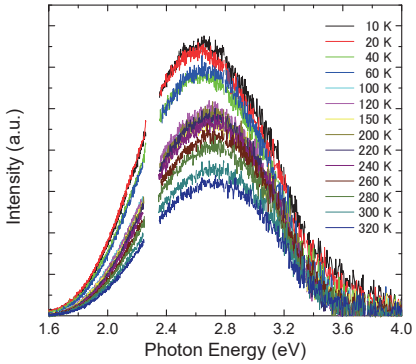

Fig. 1. Temperature dependence of the PL spectra of *a*-CN_x 60 W.

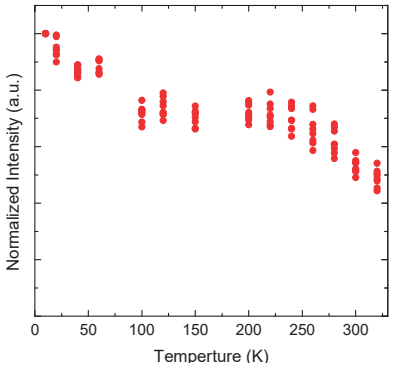

Fig. 2. Temperature dependence of the PL intensity at each emission photon energy.

[1] M. Satake *et al.*, 2013 JSAP Autumn Meeting 28p-PB3-11.
[2] K. Nakamura *et al.*, UVSOR Activity Reports **43** (2016) 61.

BL3B

Photoluminescence and Excitation Spectra of Ce^{3+}, Eu^{3+} Singly Doped $Lu_3Al_{4.75}Si_{0.25}O_{11.75}N_{0.25}$ Phosphors in VUV-Vis Region

K. Asami, K. Yasuda, J. Ueda and S. Tanabe
Graduated School of Human and Environmental Studies, Kyoto University, Kyoto 606-8501, Japan

The Ce^{3+} doped garnet phosphors are attracting much attention in the application for white light emitting diodes (LEDs) and scintillators [1]. Commercial white LED is composed of a blue LED and yellow phosphor such as $Y_3Al_5O_{12}:Ce^{3+}$ (YA*G*:Ce) [2]. YA*G*:Ce phosphor has strong absorption in the range of blue LED wavelength (λ:~ 450 nm) and shows broad yellow luminescence with high quantum yield (~90%). However, the generated whit light exhibits a low color rendering and high color temperature due to color deficiency in the red spectral region. In order to realize the redshift of emission, there are many reports to expand crystal field splitting of Ce^{3+} by substitution of the cation at each site [3]. Recently, it is reported that N^{3-} ligands which is lower electronegativity than O^{2-} ligands incorporate into YAG and $Lu_3Al_5O_{12}$ (LuA*G*) hosts to replace O^{2-} anions and Si^{4+} was used as a charge compensation [4]. Setlur et al. have proven that $Lu_3(Al,Si)_5(O,N)_{12}:Ce^{3+}$ phosphor shows a very broad and warmer emission spectrum and the lower thermal quenching [5]. To investigate the electronic structure of $Lu_3Al_{4.75}Si_{0.25}O_{11.75}N_{0.25}$ (LuASON*G*), we measured photoluminescence and excitation (PL & PLE) spectra of both Ce^{3+} and Eu^{3+}- singly doped phosphors at UVSOR BL3B. Ce^{3+}, Eu^{3+} singly doped LuASON*G* phosphors are prepared by solid state reaction method with N_2 atmosphere. Samples are identified as garnet structure by XRD.

Figure 1 shows the PLE and PL spectra of Ce^{3+}- doped LuASON*G* phosphor at 10 K. In PLE spectrum, the host exciton peaks are observed at around 170 nm and three bands derived from Ce^{3+} are observed at 220 nm (4f-$5d_{3,4,5}$), 350 nm (4f-$5d_2$) and 450 nm (4f-$5d_1$). From the host exciton peak, the bandgap energy is estimated to be 7.92 eV, which is almost the same as that of LuA*G* (7.94 eV) [5]. In PL spectrum, two emission bands are observed at around 500 and 560 nm, which are attributed to $5d_1$-$4f(^2F_{5/2})$ and $4f(^2F_{7/2})$, respectively. These emission bands are longer wavelength than that of LuA*G* slightly. From there results, the substitution of Si^{4+}-N^{3-} bonds for Al^{3+}-O^{2-} bonds increases crystal field strength and causes redshift of emission.

Figure 2 shows PLE and PL spectra of Eu^{3+}- doped LuASON*G* phosphor at 10 K. The strong broad band is located at around 230 nm, which is attributed to charge transfer transition (CTS) of Eu^{3+}. The sharp emission peaks ($^5D_0$-$^7F_{1,2,4}$ and $^5D_1$-$^7F_4$) due to the intra-4f transitions of Eu^{3+} are observed in the range of 580-720 nm. CTS energy of LuASON*G* (5.26 eV) is lower than that of LuA*G* (5.53~5.65 eV) [6,7]. CTS energy is equivalent to the bandgap between Eu^{2+} 4f ground state and valence band edge which *p* state of anion forms. By substitution of Si^{4+}-N^{3-}, p state of N^{3-} interacts with the top of VB. Therefore, CTS energy of oxynitride garnet is lower than that of oxide garnet.

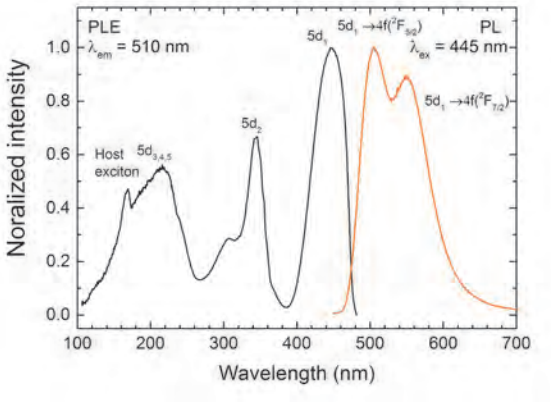

Fig. 1. PLE and PL spectra of LuASON*G* :Ce^{3+}.

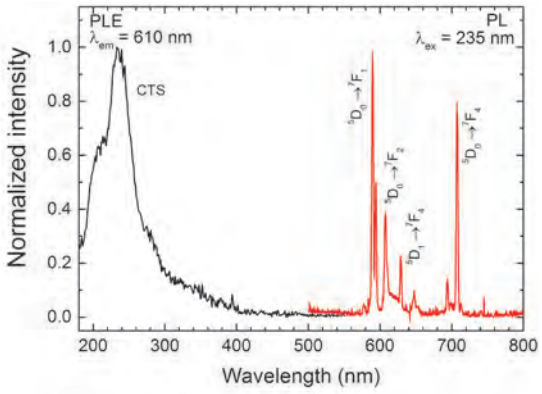

Fig. 2. PLE and PL spectra of LuASON*G* :Eu^{3+}.

[1] Z. Xia and A. Meijerink, Chem. Soc. Rev. **46** (2017) 275.
[2] G. Blasse and A. Bril, Appl. Phys. Lett. **11** (1967) 53.
[3] C. C. Chiang, M. S. Tsai and M. H. Hon, J. Electrochem. Soc. **155** (2008) B517.
[4] J. Liu, X. Wang, T. Xuan, C. Wang, H. Li and Z. Sun, J. Lumin. **158** (2015) 322.
[5] A. A. Setlur, W. J. Heward, M. E. Hannah and U. Happek, Chem. Mater. **20** (2008) 6277.
[6] P. Dorenbos, J. Lumin. **134** (2013) 310.
[7] L. Li and S. Zhang, J. Phys. Chem. B **110** (2006) 21438.

BL3B, BL7B

Total Photoelectron Yield Spectroscopy on 3*d* Transition Metal Doped AlN Films

N. Tatemizo[1], S. Imada[1], F. Sawa[2], S. Hirata[2] and K. Fukui[2]
[1]*Faculty of Electrical Engineering and Electronics, Kyoto Institute of Technology, Kyoto 606-8585, Japan*
[2] *Faculty of Electrical and Electronics Engineering, University of Fukui, Fukui 910-8507, Japan*

It is well known that 3*d*-transition metals (3*d*-TMs) can form impurity levels in the band gap of a semiconductor and these levels can accept and/or donate electrons when irradiated with light of appropriate energy. At high concentrations, the 3*d*-TMs' orbitals will start to overlap with one another, to form an impurity band. Such an impurity band well apart from the conduction band (CB) and the valence band (VB) in a heavily doped semiconductor can intermediate optical excitations of electrons from the VB to the CB. This is so called an intermediate band (IB) material proposed by Luque *et al*., for use in absorption layers of solar cells to increase their conversion efficiency [1].

Based on this hypothesis, we have synthesized and investigated 3*d*-TM-doped AlN films for artificial photochemical system. It is indispensable to reveal potential energies of VB, IB and CB with respect to the vacuum level if the potentials have ability for the water oxidation and hydrogen reduction potentials.

To investigate the potentials of the electron occupied states (VB and/or a part of IB), we carried out total photoelectron yield spectroscopy (TPYS) [2] for the 3*d*-TM doped AlN films deposited on Ti metal substrates. As show in Fig. 1. electrical contacts with the film were made both back (thorough the Ti substrate) and front (a Cu metal plate with hole). A photoelectron corrector was set in front of the film with around 1mm interspace. A negative bias was applied to the sample against the grounded photoelectron corrector. The number of photoelectrons was obtained by measuring the current needed to compensate for the photoexcited holes at the sample with an ammeter. The photoemission yield was measured as a function of incident photon energy.

Figure 2 shows TPY spectra of AlCrN with 17.3, 9.3 and 2.2% Cr and un-intentional doped AlN films. It is clear that the AlCrN films with high Cr concentrations have threshold at around 5.5 eV. This result agrees well with the level of $Cr^{4+/3+}$ [3, 4] and imply a partially filled IB is formed in the energy gap of AlN. We have obtained different thresholds for different 3d-TM elements, which means the potential of IB can be controlled via choice of 3*d*-TM elements, and adjust the band structure for the effective photoconversion. To reveal all potentials of the electron occupied band of the films, we will extend the energy region of the measurements to larger one.

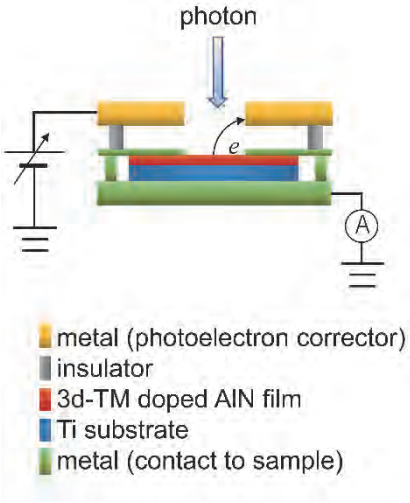

Fig. 1. Schematic of sample setting for the TPYS measurements.

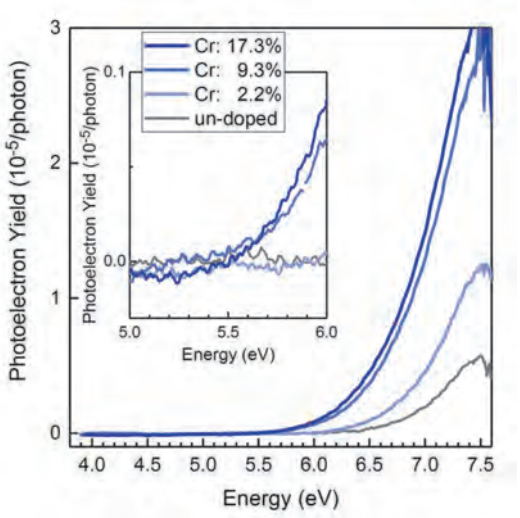

Fig. 2. Total photoelectron yield spectra of AlCrN (Cr: 17.3, 9.3 and 2.2 %) and un-intentional doped AlN films deposited on Ti metal substrates. The inset is magnified view of near thresholds of AlCrN films.

[1] A. Luque *et al*., Phys. Rev. Lett. **78** (1997) 5014.
[2] M. Honda *et al*., J. Appl. Phys. **102** (2007) 103704.
[3] U. Gerstmann *et al*., Phys. Rev. B **63** (2001) 1.
[4] N. Tatemizo *et al*., J. Phys.: Condens. Matter **29** (2017) 085502.

BL3B

Optical Properties of Ag^- Centers Doped in NaI Crystals

T. Kawai and S. Watanabe
Graduate School of Science, Osaka Prefecture University, Sakai 599-8531, Japan

Ag^- centers doped in alkali halide crystals belong to the family of the so-called Tl^+-type centers and exhibit the optical bands called A, B, and C, which are attributed to intra-ionic transitions from the $^1A_{1g}$ ground state to the $^3T_{1u}$, $^3T_{2u}$ +^3E_u, and $^1T_{1u}$ excited states, receptively [1-3]. Though optical studies on the Ag^- centers doped in various alkali halide crystals have been widely performed, no study on the Ag^- centers doped in NaI crystals has been reported until now. In this study, optical properties of the NaI:Ag^- crystals have been investigated at low temperature.

NaI:Ag^+ crystals were grown by the Bridgman method from NaI powders containing AgI powders. The conversion from the Ag^+ to Ag^- ions in the crystals was achieved by an electrolytic coloration technique. The optical measurements were performed at the BL-3B line of UVSOR.

Figure 1 shows the absorption and luminescence spectra of the NaI:Ag^- crystals at 6 K. A remarkable absorption band with a half-width of 0.15 eV is observed at 3.96 eV. The Ag^- centers doped in KI, RbI, and CsI crystals exhibit the C absorption bands at 3.985, 3.888, and 3.770 eV, respectively [1, 2]. As compared with these values, the band peaking at 3.96 eV in NaI:Ag^- is assigned to the C absorption band.

In the NaI:Ag^- crystals, the excitation on the C absorption band induces the two luminescence bands peaking at 2.50 and 3.48 eV at 6K. The excitation spectra for the 2.50 and 3.48 eV luminescence bands are shown in Fig. 2. Both luminescence bands are efficiently excited at the C absorption band. Therefore, the 2.50 and 3.48 eV luminescence bands are assigned to the A' and C' luminescence bands which are attribute to the radiative transitions from the relaxed excited states of $^3T_{1u}$ and $^1T_{1u}$, respectively. In addition to the C band, the excitation spectrum for the A' luminescence band has an excitation band around 2.92 eV. The excitation band would correspond to the A band due to the transition from the $^1A_{1g}$ to $^3T_{1u}$ states. The energy positions of the A, B, and C bands of the Ag^- centers doped in alkali iodide crystals are summarized in Table 1.

It should be noted that the band-shapes of the excitation spectra around the C absorption band are different between the A' and C' luminescence. The excitation band for the A' luminescence roughly reflect the C absorption band, while that for the C' luminescence is located on the slightly lower energy side of the C absorption band. The difference of the excitation band-shape would be concerned with the relaxation processes from the excited states of $^3T_{1u}$ and $^1T_{1u}$. Further studies will probably be necessary.

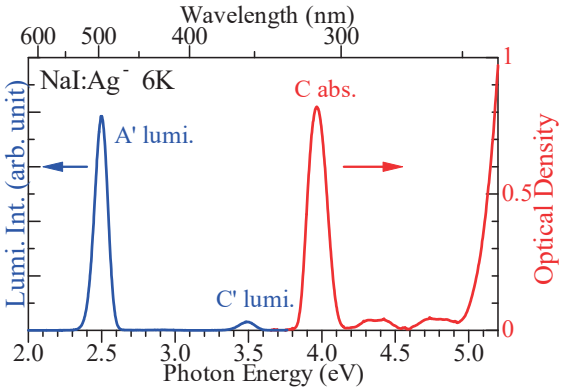

Fig. 1. Luminescence (blue) and absorption (red) spectra of NaI:Ag^- crystals at 6 K.

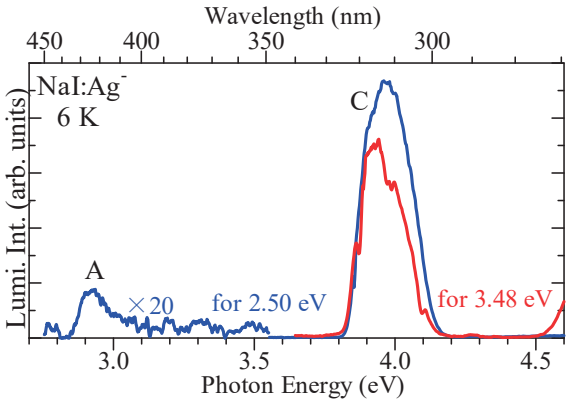

Fig. 2. Excitation spectra detected at 2.50 eV (blue) and 3.48 eV (red) of NaI:Ag^- crystals at 6 K.

Table 1. Energy positions (eV) of the bands of the Ag^- centers doped in alkali iodide crystals.

crystal	A	B	C	Ref.
NaI	2.92	–	3.96	this work
KI	2.878	2.981	3.985	[2]
RbI	–	–	3.888	[1]
CsI	2.776	2.865	3.770	[2]

[1] W. Kleemann, Z. Physik **214** (1968) 285.
[2] W. Kleemann, Z. Physik **248** (1970) 362.
[3] S. Shimanuki, J. Phys. Soc. Jpn. **35** (1973) 1680.

BL3B

Energy Transfer from I^- Centers to Eu^{2+} Centers in Co-Doped NaCl:I^-,Eu^{2+} Crystals

O. Yagi and T. Kawai

Graduate School of Science, Osaka Prefecture University, Sakai 599-8531, Japan

Alkali halide crystals have the wide band-gap up to the vacuum ultraviolet energy region and are suitable candidate hosts for doping of impurity ions. Though many experimental investigations have been performed on alkali halide crystals doped with impurity ions, energy transfer between two kind of impurity ions in co-doped alkali halide crystals is comparatively less studied [1, 2]. In this study, we have investigated the energy transfer from I^- centers to Eu^{2+} centers in NaCl crystals co-doped with I^- and Eu^{2+} ions.

Figure 1 shows the absorption spectrum of NaCl:Eu^{2+} and the luminescence spectrum of the NaCl:I^-. NaCl:Eu^{2+} produces two broad absorption bands in the uv-visible energy region, which are due to transitions from the $4f^7$ ground state to the t_{2g} and e_g components of the $4f^6 5d$ excited state [3]. The samples were annealed for 2h at 600ºC and quenched to disperse precipitations, because Eu^{2+} ions in the alkali halides are well-known to produce precipitations. NaCl:I^- shows the luminescence band appearing around 5.2 eV, which is called the NE luminescence band and comes from the one-center type exciton localized mainly on the central site of a substituted I^- impurity with small lattice relaxation [4]. The NE luminescence band in NaCl:I^- has a large overlap with the absorption band due to the e_g component in NaCl:Eu^{2+}. This fact indicates the potential of the energy transfer from the I^- centers to the Eu^{2+} centers in co-doped NaCl: I^-,Eu^{2+} crystals. According to the Förster model [5, 6], the critical distance between both centers for resonant energy transfer is estimated to be about 1.8 nm from the overlap with the luminescence and absorption bands.

Figure 2 shows the excitation spectra in NaCl:I^-, NaCl:Eu^{2+}, and co-doped NaCl:I^-,Eu^{2+} crystals. The NE luminescence band in NaCl:I^- is efficiently excited in the energy region around 6.7 eV, which corresponds to the absorption band of the I^- centers. In NaCl:Eu^{2+}, the luminescence band at 2.9 eV, which comes from the Eu^{2+} centers, is efficiently excited at the absorption bands of the Eu^{2+} centers.

In the co-doped NaCl:I^-,Eu^{2+} crystals, the excitation spectrum for the 2.9 eV luminescence band of the Eu^{2+} centers has the broad band around 6.7 eV in addition to the absorption bands of the Eu^{2+} centers. This result implies the existence of the energy transfer from the I^- centers to the Eu^{2+} centers in the co-doped NaCl:I^-,Eu^{2+} crystals. In order to clarify the energy transfer mechanism from the I^- centers to the Eu^{2+} centers in the co-doped NaCl:I^-,Eu^{2+} crystals, the measurements of the decay kinetics of the luminescence are needed.

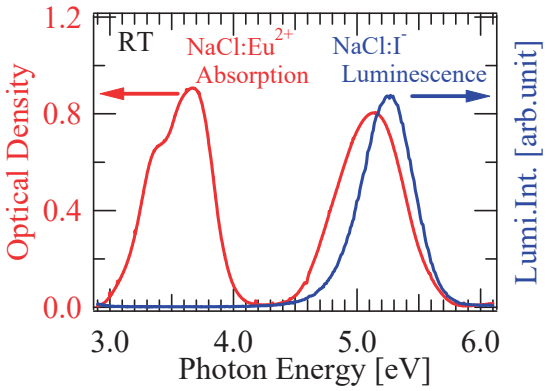

Fig. 1. Luminescence spectrum (blue) of NaCl: I^- and absorption spectrum (red) of NaCl: Eu^{2+} at RT.

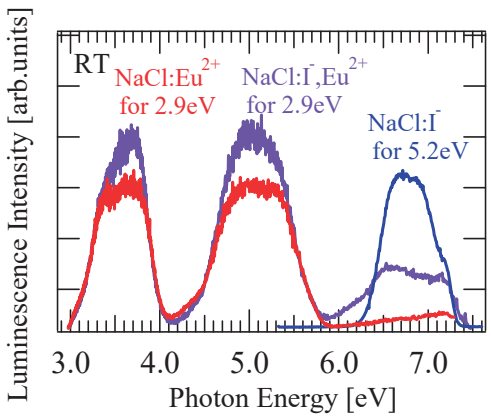

Fig. 2. Excitation spectra of NaCl: Eu^{2+} (red), NaCl: I^- (blue), and co-doped NaCl: I^-, Eu^{2+} (purple) at RT.

[1] A. F. Muñoz and J. O. Rubio, Phys. Rev. B **38** (1988) 9980.
[2] A. Méndez *et al*., J. Lumin. **79** (1998) 269.
[3] J. E. Muñoz-Sautiuste and J. Garcia-Sole, Phys. Rev. B **38** (1988) 10874.
[4] I. Akimoto *et al*., Phys. Status Solidi C **6** (2009) 342.
[5] T. Förster, Disc. Faraday Soc. **27** (1959) 7.
[6] D. L. Dexter, J. Chem. Phys. **21** (1953) 836.

BL3B

Luminescence and Photoexcitation Spectra of TlBr-TlI Mixed Crystals

N. Ohno[1] and K. Matsui[2]

[1]*Fundamental Electronics Research Institute, Osaka Electro-Communication University, Neyagawa 572-8530, Japan*

[2]*Graduate School of Engineering, Osaka Electro-Communication University, Neyagawa 572-8530, Japan*

Thallous halide crystals are compound semiconductors attractive for fabrication of γ ray detectors. They exhibit high stopping power due to high atomic number and high density [1]. TlCl and TlBr crystalize in cubic CsCl-type structure, while the stable form of TlI is orthorhombic structure below 170ºC [2] and is cubic CsCl-type one above it [3, 4]. Therefore, it is difficult to grow a large-sized single crystal of TlI under atmospheric conditions. In the present study, mixed crystals of TlBr-TlI in cubic CsCl-type structure have been grown and examined to reveal the optical properties such as absorption, reflection spectra, and photoluminescence, luminescence excita- tion spectra at low temperatures.

The crystals $TlBr_xI_{1-x}$ were grown by the Bridgeman method from appropriate amounts of TlBr and TlI after distillation and purification. A plate of the sample cut from as-grown crystals was polished with alumina abrasive plastic film, then etched in methyl alcohols containing dilute bromine. The optical measurements were made at 10 K at the BL3B station.

Figure 1 shows luminescence spectra (blue curves) of $TlBr_xI_{1-x}$ mixed crystals of different compositions at 10 K. On exciting $TlBr_xI_{1-x}$ with light at the energy above the indirect absorption edge [4, 6], a Stokes-shifted broad luminescence bands are observed for each crystal. Photoecitation spectra for the luminescence band are shown by black curves in the figure. The luminescence bands are found to be efficiently stimulated at the energy between the fundamental absorption edge transition and the direct exciton transition by indicated by arrows. As clearly seen in Fig.1, the excitation edge for the luminescence band moves to the lower energy with increasing iodine concentration x. In pure TlBr (x=1.0), the excitation edge at 2.64 eV is ascribed to the indirect-forbidden exciton transition [5]. At x=0.4, the absorption edge is located at around 2.0 eV. Below $x \leq 0.3$, no luminescence band was observed, which is caused by the phase transition of the crystal; in iodine-rich mixed crystal, the cubic phase is unstable below the room temperature [4].

In TlBr (x=1.0), the spectral shape of the broad luminescence band is almost Gaussian as previously observed in lightly doped TlBr [5]. The broad band has been identified as annihilation of relaxed excitons due to the impurity-induced self-trapping. It is worth noting that the amount of the Stokes shift and the width of the observed luminescence band in mixed crystals becomes small as the iodine concentration x is increased as clearly seen in the figure. Therefore, with adding iodine ions in TlBr, the lattice relaxation of the self-tapped excitons becomes small, which is ascribed to the weak exciton-phonon interaction.

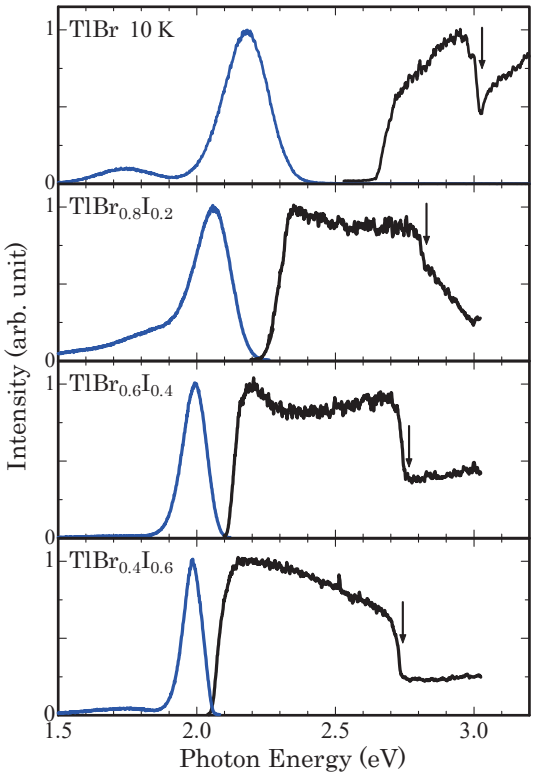

Fig. 1. Luminescence (blue) and photoexcitation (black) spectra of $TlBr_xI_{1-x}$ at 10 K.

[1] K. Hitomi, T. Shoji and K. Ishii, J. Crystal Growth **379** (2013) 93.
[2] N. Ohno and M. Itoh, J. Phys. Soc. Jpn. **62** (1993) 2966.
[3] K. Heidrich, W. Staude, J. Treusch and H. Overhof, Solid State Commun. **16** (1975) 1043.
[4] A. Fujii, J. Phys. Soc. Jpn. **58** (1989) 2173.
[5] K. Takahei and K. Kobayashi, J. Phys. Soc. Jpn. **44** (1978) 1850.
[6] N. Ohno and K. Matsui, UVSOR Activty Report **43** (2016) 65.

BL4U

Improved Photoelectrochemical Performance of Au@TiO_2-coated Fe_2O_3 Nanorods Studied by Scanning Transmission X-ray Microscopy

Y. R. Lu[1, 2], Y. F. Wang[1], Y. C. Huang[1, 2], J. W. Chiou[3], C. L. Dong[1], W. F. Pong[1], T. Ohigashi[4] and N. Kosugi[4]

[1]*Department of Physics, Tamkang University, Tamsui 251, Taiwan*
[2]*Department of Electrophysics, National Chiao Tung University, Hsinchu 300, Taiwan*
[3]*Department of Applied Physics, National University of Kaohsiung, Kaohsiung 811, Taiwan*
[4]*Institute for Molecular Science, Okazaki 444-8585, Japan*

Since Fujishima and Honda had found the photoelectrochemical (PEC) water splitting could be made directly by TiO_2 under UV irradiation thirty years ago, this direct solar fuel conversion is regarded as one of the most promising clean and renewable energy resource. The main drawback of TiO_2 is the bandgap is too large so it can only absorb the UV light. Hematite (α-Fe_2O_3) is a promising material for solar water splitting owing to its smaller band gap energy about 2.1-2.3 eV, which can capture 40% of incident sunlight. However, it is only suitable for oxygen evolution half reaction and electron-hole recombines very easily due to its intrinsic short hole diffusion length and poor electron conductivity. Doping is an effective way to adjust the band edge and overcome the charge transfer ability in hematite.[1-2] In addtion, by taking advantage of plasmonic effect caused by metal nanocrystals, the PEC performance could be further improved. In this work, the hematite nanorods coated with a thin layer of TiO_2 with/without Au nanoparticles embbeded in between have been studied by STXM to elucidate the correlation between the PEC properties and interfacial electonic structures.

Figures 1 present the O *K*-edge (left panel) and Fe *L*-edge (right panel) STXM stack mappings of selected single nanorod of bare-, TiO_2 coated and Au embedded TiO_2-coated Fe_2O_3. The stack mappings display yellow, red and green areas, corresponding to the different regions that are associated with different regions and chemical properties of the nanorods. Figures 1 also present the XANES spectra, which correspond to their stack mappings. While there is no significant difference of XANES of Ti L-edge (not shown here) could be revealed, the variation of both O K-edge and Fe L-edge are observed. Spectroscopic results indicate the surface region contains more defects compared with core region, which enhance the density of states both in O and Fe sites. However, the TiO_2 layer and embedded Au nanoparticles may inhibit the charge recombination.

The enhanced PEC performance of TiO_2-coated Fe_2O_3 with Au nanoparticles embedded is likely to be not only the plasmonic effect caused by Au nanoparticles, but also the intrinsic improvement of charge transfer ability that is attributable to embedded Au nanoparticles.

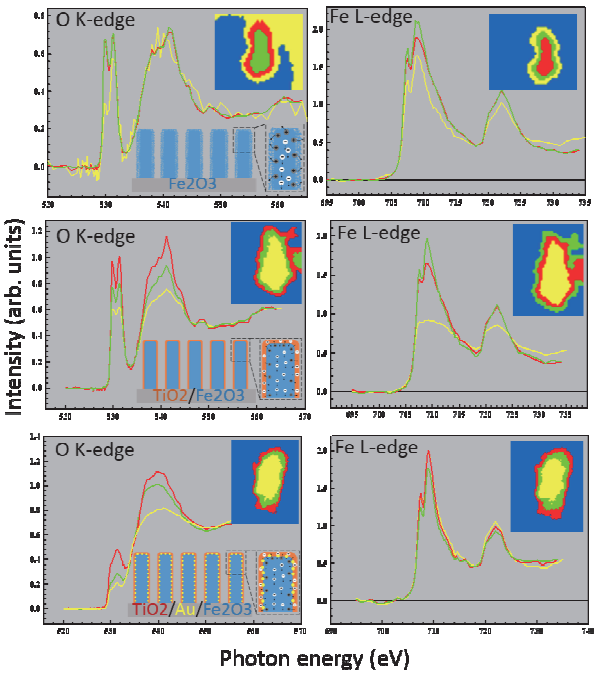

Fig. 1. O *K*-edge (left panel) and Fe *L*-edge (right panel) scanning transmission X-ray microscopy image and its corresponding stack mappings of selected single (top) bare-, (middle) TiO_2-coated, and (bottom) TiO_2/Au- coated Fe_2O_3 nanorod.

[1] Y. Fu *et al.*, Chem Nano Mat **2** (2016) 704.
[2] Y. Fu *et al.*, Phys. Chem. Chem. Phys. **18** (2016) 5203.
[3] Y. R. Lu *et al.*, to be submitted.

BL4U

Structural Identification of Cellulose Nanocrystal/Nanofibril Hybrids and Composites Using Soft X-ray Techniques

M. Y. Ismail[1], M. Huttula[2], M. Patanen[2], H. Liimatainen[1], T. Ohigashi[3] and N. Kosugi[3]
[1]*Fibre and Particle engineering unit, University of Oulu, P.O. Box 3000, 90014 University of Oulu, Finland*
[2]*Nano and Molecular Systems unit, University of Oulu, P.O. Box 3000, 90014 University of Oulu, Finland*
[3]*UVSOR Synchrotron, Institute for Molecular Science, Okazaki 444-8585, Japan*

Nanocellulose hybrids are high strength materials consisting of cellulose nanofibrils or nanocrystals embedded in a continuous biopolymeric matrix with additives such as mineral nanoparticles. In the present work, the structure of the hybrid formed of nanosilica, nanocellulose (cellulose nanofibrils) and chitosan matrix is studied. The critical factors affecting the mechanical performance of these materials are the interaction between the constituents and their spatial distribution. So far, these properties have mainly been analysed using electron microscopy techniques (TEM and SEM), but they possess limited ability to localize nanocellulose and biopolymers within the hybrid structure (e.g. to determine interactions between minerals and nanocelluloses). Therefore, novel methods are desired to better address the structural details of the hybrids. Previously, soft X-ray spectroscopy has shown to be able to identify the localized distribution of biopolymers, but based on our best knowledge this methodology has not been used for nanocellulose hybrids. This report shows significant new outcomes on structural characteristics of nano-scale hybrids based on nanocelluloses.

Chitin is one of the most abundant natural biopolymers and it is used for the production of chitosan by deacetylation [1]. Chitosan is antibacterial, non-toxic, and biodegradable; thus, it can be used for the production of biodegradable films which are potential green alternatives for commercially available synthetic counterparts. However, poor mechanical and thermal properties of chitosan restrict its wide spread applications. Consequently, hybrids fabricated from chitosan matrix reinforced by nanofibers are attractive materials to develop sustainable products [2].

The aim of the present work was to obtain a nano-scale spatial distribution of constituents within the hybrid. The hybrids had constant nanocelluloses: chitosan ratio of 50:50, and variable nanosilica content (5-30%). The samples (thickness of 100 nm) were prepared from solution casted hybrid films using an ultramicrotome. Pure nanocellulose, nanosilica and chitosan samples were used as references.

The samples were exposed to soft X-ray radiation at BL4U beamline at UVSOR synchrotron. The absorption at carbon 1s-edge was recorded for investigation of the nanocellulose and the matrix distribution, with photon energies between 280 and 300 eV. The Si 2p absorption edge around 100 to 130 eV was utilized for the same spatial parts of the sample for observing the distribution of nanosilica on the hybrid.

Figure 1 presents examples of the image data of the 30% nanosilica sample. In the first preliminary interpretation the nanosilica (Si2p on leftmost) appears to be concentrated on the fiber bundles of the sample. The nanocellulose fibers were found to provide somewhat characteristic absorption structure (Fig.2.), matching the intense absorption patterns on the Fig.1. Similarly the appearance of smaller “dots” of nanosilica on the fibers were also found in the sample containing only 5% of the nanosilica.

The obtained data seem to provide a strong evidence of the agglomeration of the nanosilica at the nanofibers. Indications on the spectral changes in the Si rich regions suggest also possible chemical binding mechanism of the nanoselluloce and nanosilica. The present data will give valuable information of behavior of the additive mineral which will affect the mechanical properties of composite hybrid materials.

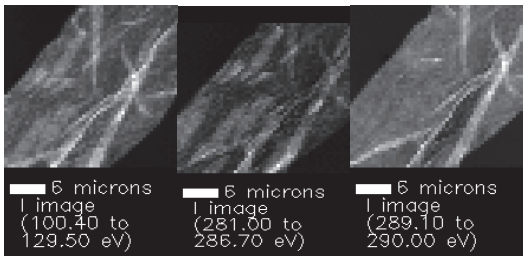

Fig. 1. STXM images for 30% nanosilica sample.

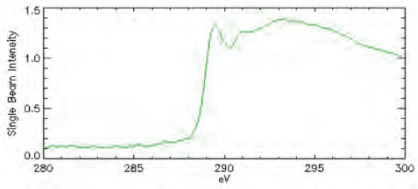

Fig. 2. The C1s absorption reference for nanocellulose fibers.

[1] Abdul Khalil H.P.S. Chaturbhuj K. Saurabha, Adnan A.S., *et al*., Carbohydrate Polymers **150** (2016) 216.
[2] R. J. Moon, A. Martini, J. Nairn, J. Simonsen and J. Youngblood, Chemical Society Reviews **40** (2011) 3941.

BL4U

Dopant Effect of Lead(II) Thiocyanate ($Pb(SCN)_2$) for $FA_{0.9}Cs_{0.1}PbI_3$ Perovskite Solar Cells

M. W. Lin[1], M. H. Li[2], H. W. Shiu[1], Y. L. Lai[1], T. Ohigashi[3], N. Kosugi[3], P. Chen[2] and Y. J. Hsu[1, 2]

[1]*National Synchrotron Radiation Research Center, Hsinchu 300, Taiwan*
[2]*Department of Photonics, National Cheng Kung University 701, Tainan, Taiwan*
[3]*Institute for Molecular Science, Okazaki 444-8585, Japan*

Thiocyante ($Pb(SCN)_2$), as a dopant in perovskite $FA_{0.9}Cs_{0.1}PbI_3$ (FA: $HC(NH)_2$), and mesoscopic titania (mp-TiO_2) as scaffold/electron-transport layer show high power conversion efficiencies (PCEs) up to 15.1%. Herein we studied the origin of such high PCEs in terms of morphology and chemical structure of mp-TiO_2/$Pb(SCN)_2$ doped- $FA_{0.9}Cs_{0.1}PbI_3$ heterojunction by scanning electron microscopy (SEM) and scanning transmission X-ray microscopy (STXM).

In SEM studies (Fig. 1), the $Pb(SCN)_2$ doped-$FA_{0.9}Cs_{0.1}PbI_3$ displays much larger perovskite crystalline than $FA_{0.9}Cs_{0.1}PbI_3$. More than 70% of the larger crystals in 5% $Pb(SCN)_2$ doped- $FA_{0.9}Cs_{0.1}PbI_3$ crystals exhibit a size distribution in the range of 0.8-1 μm size. Increasing $Pb(SCN)_2$ dopant to 10% in $FA_{0.9}Cs_{0.1}PbI_3$, the size of perovskite crystals decrease to the 0.5 μm and display homogeneous distribution. The large crystals in the perovskite bulk film are beneficial for charge transport in the perovskite,[1] that is possible to explain 5% $Pb(SCN)_2$ doped- $FA_{0.9}Cs_{0.1}PbI_3$ has best PECs than the others.

To further examine the effects of adding $Pb(SCN)_2$ on the crystalline morphology, chemical maps of N *K*-edge and Ti *L*-edge were acquired to obtain the distributions of micro-aggregates of SiN/mp-TiO_2/5% and 10% $Pb(SCN)_2$ doped- $FA_{0.9}Cs_{0.1}PbI_3$ by STXM. Figure 2 displays the STXM images of SiN/mp-TiO_2/5% $Pb(SCN)_2$ doped- $FA_{0.9}Cs_{0.1}PbI_3$ (Fig. 2(a)), and SiN/mp-TiO_2/10% $Pb(SCN)_2$ doped-$FA_{0.9}Cs_{0.1}PbI_3$ (Fig. 2(b)) which are optical density (OD) maps obtained at 403.5 eV for N *K*-edge and 457 eV for Ti *L*-edge, the characteristic absorption peaks of $FA_{0.9}Cs_{0.1}PbI_3$ and mp-TiO_2, respectively. The N mapping on above samples show similar distribution in morphology and size to SEM results. The 5% $Pb(SCN)_2$ doped- $FA_{0.9}Cs_{0.1}PbI_3$ shows grain size of ~1 μm, and decrease to 0.5 μm when 10% $Pb(SCN)_2$ doped. However, we notice some additional line shape and large aggregation as shown in red color in the composite images, that is determined as TiO_2 nanoparticles which are in a uniform diameter of 2–5 μm and appear to be more uniformly dispersed in the sample of 5% $Pb(SCN)_2$ doped- $FA_{0.9}Cs_{0.1}PbI_3$. It suggests 5% $Pb(SCN)_2$ dopant has effective charge transfer between perovskite and TiO_2. Fig. 2(c) and (d) show the micro-scpectra of N *K*-edge and Ti *L*-edge extracted from 5% and 10% $Pb(SCN)_2$ doped-$FA_{0.9}Cs_{0.1}PbI_3$ film. We notice that both N and Ti spectra exhibit dissimilar in peak ratio and shape between 5% and 10% $Pb(SCN)_2$ doped sample. It implies that the interaction between mp-TiO_2 and perovskite may be play a key role in determining the PCEs performance.

In conclusion, STXM results clear show that morphology variation attributed by TiO_2 and $Pb(SCN)_2$, and also illustrate that an important chemical interaction between mp-TiO_2 and perovskite.

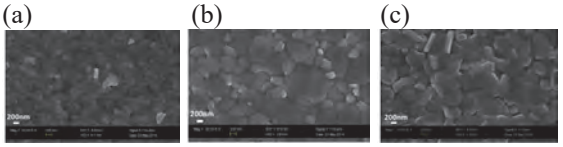

Fig. 1. The SEM image of (a) $FA_{0.9}Cs_{0.1}PbI_3$, (b) 5% $Pb(SCN)_2$ doped- $FA_{0.9}Cs_{0.1}PbI_3$, and (c) 10% $Pb(SCN)_2$ doped- $FA_{0.9}Cs_{0.1}PbI_3$.

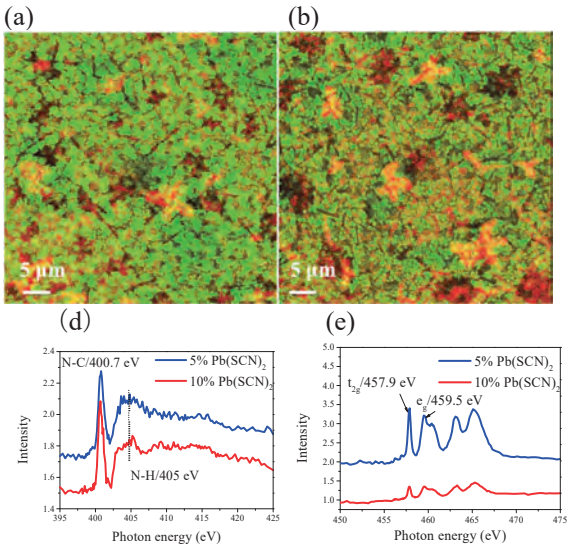

Fig. 2. OD mapping of Ti *L*-edge (red) and N *K*-edge (green) of (a) SiN/mp-TiO_2/5% $Pb(SCN)_2$ doped-$FA_{0.9}Cs_{0.1}PbI_3$, and (b) SiN/mp-TiO_2/10% $Pb(SCN)_2$ doped- $FA_{0.9}Cs_{0.1}PbI_3$. (c) and (d) micro-spectra of N *K*-edge and Ti *L*-edge extracted from (a) and (b), respectively.

[1] Z. Xiao, *et al.*, Adv. Mater. **26** (2014) 6503.
[2] M.-W. Lin, *et al.*, Adv. Mater. Interfaces **3** (2016) 1600135.

BL4B

Valence State Analysis of Fe Ions in $LaGaO_3$

Y. Osada[1] and T. Yamamoto[1, 2]
[1]*Faculty of Science and Engineering, Waseda University, Tokyo 169-8555, Japan*
[2]*Institute of Condensed-Matter Science, Waseda University, Tokyo 169-8555, Japan*

Solid Oxide Fuel Cell (SOFC) has been widely studied because of its importance as one of the energy sources. Among the SOFCs, $LaGaO_3$ has been extensively investigated because of its high oxygen ion conductivity. In order to increase its ionic conductivity, incorporation of Sr^{2+} and Mg^{2+} ions in $LaGaO_3$ were proposed, so-called LSGM, which can produce oxygen vacancies in the material to keep the charge neutrality. It was reported that additional incorporation of Co ions in LSGM increase ionic conductivity. [1] Although it is quite important to know the charge state of such transition elements in LSGM for the understanding of increase of ionic conductivity owing to the additional ion incorporation, such investigations have not yet been carried out. In the current study, valence state of the Fe ions in $LaGaO_3$ was examined as a proto-type experiment by measuring the Fe-L_3 X-ray absorption spectrum (XAS).

All the samples were synthesized with the conventional solid-state reaction method changing the concentration of Fe ions, i.e., x = 0, 0.05, 0.1 and 0.15 in LaGa1-xFexO3. High purity powders of La2O3, Ga2O3 and Fe2O3 were used as starting materials. For precise weighing, La2O3 were dried at 773 K for 30 min. in air prior to weighing. These powders were mixed in an agate mortar for 30 min., which were calcined in air at 1273 K for 6 hours. Resultant powders were ground again in an agate mortar, which were pressed into a pellet form (10 mmϕ). Finally, these pellets were sintered in air at 1773 K for 6 hours.

The synthesized specimens were characterized by the powder X-ray diffraction with Cu-Kα X-ray irradiation, which showed all the samples were crystallized in a single-phased orthorhombic perovskite structure.

Cell volumes were obtained from the observed XRD patterns, which are shown in Fig. 1. As shown in this figure, cell volumes increase as increment of Fe concentration, which suggests that Fe ions substitute at Ga^{3+} site as divalent or trivalent ions from a viewpoint of ionic radius. [2]

Fe-L_3 XAS were recorded at BL-4B with the total electron yield method. Incident beam was monochromatized with the varied-space grating (800 lines/mm), which was irradiated onto the sample. Sample powders were put on the carbon adhesive tape, which was attached on the first dinode of the electron multiplier.

Observed Fe-L3 XAS of Fe ions incorporated in LaGaO3 were shown in Fig. 2 together with those of Fe oxides. Fe-L3 profile of Fe ions in LaGaO3 are quite similar, which suggests that local environment and valence state of the Fe ions are almost identical. In addition, the profile is close to that of α-Fe_2O_3, which can confirm the valence state of Fe ions in $LaGaO_3$ is trivalent.

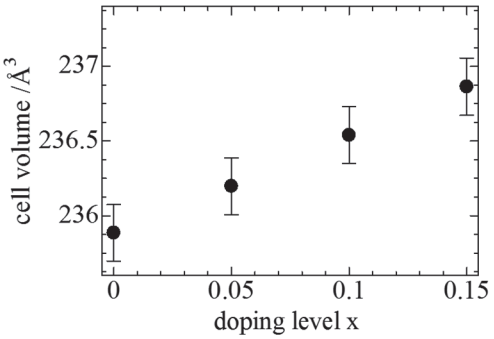

Fig. 1. Cell volumes of Fe incorporated $LaGaO_3$, $LaGa_{1-x}Fe_xO_3$.

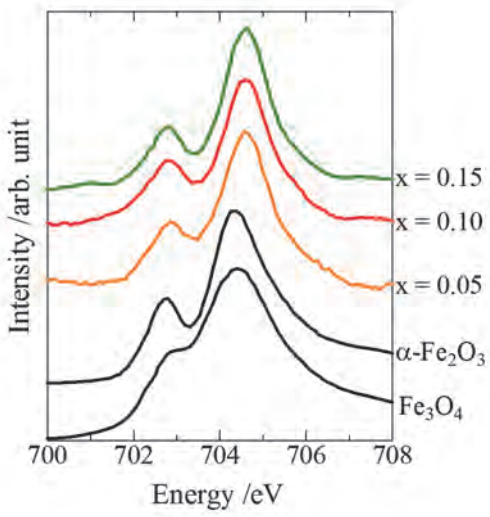

Fig. 2. Observed Fe-L_3 XAS spectra of Fe doped $LaGaO_3$ and Fe oxides.

[1] T. Ishihara *et al.*, Chem. Mater. **11** (1999) 2081.
[2] R.D. Shanon, Acta Crystallogr. **A32** (1976) 751.

BL4B

Thickness Dependence of Spin and Orbital Magnetic Moment of Ultrathin Magnetic Films: Au/Fe/Au and MgO/Fe/Au

S. Yamamoto[1], K. Yamamoto[1], Y. Hirata[1], K. Fukuta[2], D. Oshima[3], T. Kato[2], S. Iwata[3], H. Wadati[1] and I. Matsuda[1]

[1] *Institute for Solid State Physics, The University of Tokyo, Kashiwa 277-8581, Japan*
[2]*Department of Electrical Engineering and Computer Science, Nagoya University, Nagoya 464-8603, Japan*
[3]*Nagoya University, IMaSS, Nagoya 464-8603, Japan*

Interface magnetism has been one of the central topics for investigating fundamental magnetic properties. They range from the relation between the dimensionality and the magnetic structure to the control of magnetism by the electric field rather than by electric current or magnetic field. Thinner magnetic film systems have a larger contribution from the interface to the magnetism. Furthermore, it is expected that an interfacial spin-orbit interaction enhances the perpendicular magnetic anisotropy (PMA) of magnetic layers. However the effect of spin-orbit interaction on interface magnetism has not been investigated systematically so far [1].

In our previous study, we have investigated interfacial perpendicular magnetic anisotropy (PMA) energy of an ultrathin magnetic system, Au/Fe/Au, comparing with a reference system, MgO/Fe/Au [2]. By utilizing a torque magnetometer, it was revealed that PMA energy in the Au/Fe/Au system had a smaller interfacial PMA energy (455 μJ/cm^2) than that in the MgO/Fe/Au system (696 μJ/cm^2). In order to reveal the origin of the interfacial PMA for both systems, we measured thickness dependence of Fe 2*p* X-ray absorption spectroscopy (XAS) and X-ray magnetic circular dichroism (XMCD) at BL4B in UVSOR.

Samples were fabricated using a molecular beam epitaxy method before the beamtime. All of the layers were evaporated at room temperature using electron beam evaporator in an ultrahigh vacuum (7.0E-8 Pa). The epitaxial growth was confirmed by observing RHEED pattern during evaporation for both magnetic systems. The sample structure is Au(2 nm)/Fe(0.29 – 1.4 nm)/Au(25 nm)/Cr(5 nm)/MgO(001) (substrate, 0.5 mm) for Au/Fe/Au system. The top Au layer avoids oxidation of magnetic layer. The MgO/Fe/Au system has a similar structure except for being MgO layer with a thickness of 2 nm inserted between top Au and Fe layer. We confirmed that the Fe layer had not oxidized in the measurement by Fe 2*p* XAS measurements.

Measurements were conducted with a total-electron yield mode at 10 K. The samples were cooled down with a liquid He. External magnetic field, ± 2 T was applied parallel to the incident light. The sample surface was perpendicular to the incident light. The XAS (XMCD) was extracted from the sum (difference) of absorption spectra measured under applying positive and negative external field. By applying magneto-optical sum-rule for 2*p* edge XMCD, the spin and orbital magnetic moment were extracted. The Fe thickness dependence of the magnetic moment is shown in Fig. 1. In the figure, magnetic moment is expressed in the unit of μ_B/hole. We adopted this notation because in the ultrathin magnetic films, the hole number is not trivial. Furthermore, spin magnetic moment (m_{spin}^{eff}) includes magnetic dipole moment. It indicates that in both systems, larger orbital moments were observed with reducing Fe film thickness with respect to the value of bulk bcc Fe. On the other hand, the spin magnetic moment does not depend on the Fe film compared to the orbital moment. It was shown that the PMA originates from the orbital moment in both systems. The variation of orbital magnetic moment of Au/Fe/Au was smaller than that of MgO/Fe/Au system, which was consistent with our previous measurements of interfacial PMA energy.

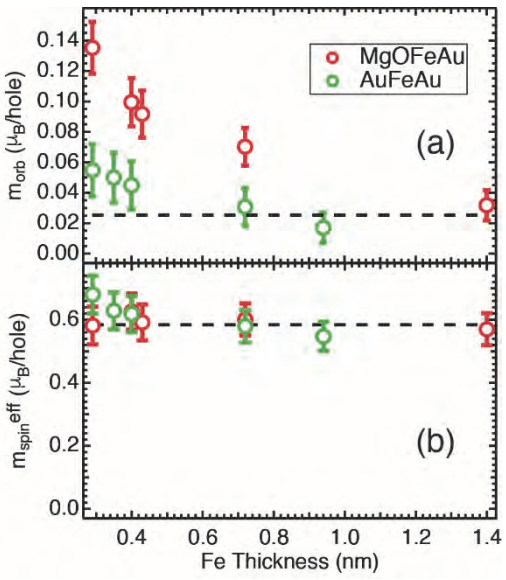

Fig. 1. Fe thickness dependence of (a) orbital (m_{orb}) and (b) spin (m_{spin}^{eff}) magnetic moment. The dashed line shows correspondent value for bulk bcc Fe.

[1] C. A. F. Vaz *et al.*, Rep. Prog. Phys. **71** (2008) 056501.
[2] J. Okabayashi *et al.*, Appl. Phys. Lett. **105** (2014) 122408.

BL5U

Electronic Structure of $Ba_{0.75}K_{0.25}Fe_2As_2$ Observed by ARPES

S. Ideta[1], M. Nakajima[2] and K. Tanaka[1]

[1]*National Institutes of Natural Science, Institute for Molecular Science, Okazaki, 444-8585, Japan*

[2]*Department of Physics, Graduate School of Science, Osaka University, Toyonaka 560-0043, Japan*

Iron-based superconductors have a complex phase diagram with the antiferromagnetic (AFM) transition and the structural phase transition. Recently, nematicity, defined as broken rotational symmetry [a trigonal(C_4)-to-orthorhombic (C_2) structural transition], has shed light on the understanding of the mechanism on the iron-based superconductivity [1-4]. In hole-doped $BaFe_2As_2$ (Ba122) system, inelastic neutron diffraction experiments of $Ba_{1-x}Na_xFe_2As_2$ and $Ba_{1-x}K_xFe_2As_2$ (K-Ba122) have shown the magnetic order without C_4 symmetry breaking [5, 6]. This indicates that the magnetism can survive even in the absence of orbital order. Besides, the superconductivity is suppressed between the superconductivity and the C_4-magnetic phase. The electronic structure at the C_4 magnetic phase has been unclear yet, and it would give us a great interest to elucidate the mechanism of the hole-doped Ba122.

Here, we have investigated the electronic structure of detwinned $Ba_{0.75}K_{0.25}Fe_2As_2$ to elucidate the occupied d_{xz} and d_{yz} states, reflecting the nematic ordering [3, 4]. As a first step, we demonstrated an angle-resolved photoemission spectroscopy (ARPES) experiment to confirm the electronic structure of the twinned K-Ba122 ($x \sim 0.25$) with the C_4-magnetic phase as shown in Fig. 1(a).

High-quality single crystals of $Ba_{0.75}K_{0.25}Fe_2As_2$ ($T_c \sim 25$ K) were grown by self-flux technique. ARPES experiments were carried out at BL 5U of UVSOR using the linearly polarized light of $h\nu$ = 32 eV-60 eV photons. Temperature was set at T = 5 and 45 K and clean sample surfaces were obtained for the ARPES measurements by cleaving single crystals *in-situ* in an ultrahigh vacuum better than 1×10^{-8} Pa.

In order to confirm the electronic structure of K-Ba122 ($x \sim 0.25$) in the k_z direction, we have performed FS mapping as shown in Fig. 1(b). From the three-dimensional shape of the FS, we found that the inner potential is $V_0 \sim 15.6$ eV which is similar to the previous ARPES study [7].

Figure 1(c) shows the ARPES intensity mapping in the two-dimensional k_x-k_y plane taken at $h\nu$ = 60 eV corresponding to the Z point. The electronic structure does not show clearly the band folding due to the spin-density-wave formation. We consider that we would need to study the temperature dependence and understand the band folding in detail.

In summary, we have performed an ARPES study of K-Ba122 ($x \sim 0.25$) and measured in- and out-of-plane ARPES intensity maps. We found that the inner potential is V_0 = 15.6 eV which is similar to the previous ARPES study and the electronic structure shows almost the same. We will demonstrate an ARPES study in detail using detwinned K-Ba122 and the temperature dependence in future work.

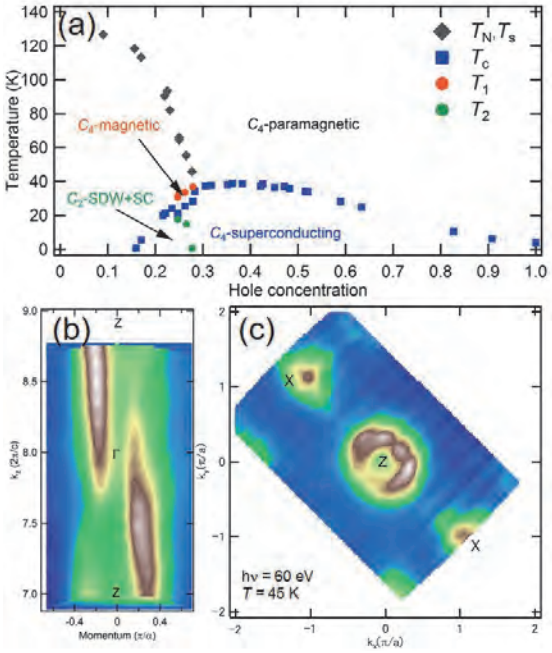

Fig. 1.(a) Phase diagram of hole-doped $Ba_{1-x}K_xFe_2As_2$ taken from Ref. [6]. T_N, T_s, and T_c denote the temperature of the magnetic, structural, and superconducting phase transition, respectively. T_1 and T_2 show the C_4-magnetic phase and superconductivity-induced reentrance of the C_2-SDW phase, respectively. (b) ARPES intensity map taken at $h\nu$ = 60 eV (T = 45 K), corresponding to the Z point (left) and FS mapping in the $k_{\parallel}$-k_z mapping taken from $h\nu$ = 32 eV–56 eV (right) (T = 5 K).

[1] R. M. Fernandes *et al.*, Nat. Phys. **10** (2014) 97.
[2] R. M. Fernandes *et al.*, Phys. Rev. Lett. **111** (2013) 127001.
[3] T. Shimojima *et al.*, Phys. Rev. B **90** (2014) 12111 (R).
[4] Y. Ming *et al.*, PNAS **108** (2011) 6878.
[5] L. Wang *et al.*, Phys. Rev. B **93** (2016) 014514.
[6] A. E. Böhmer *et al.*, Nat. Commun. **6** (2015) 7911.
[7] Y. Zhang *et al.*, Phys. Rev. Lett. **105** (2010) 117003.

BL5U

Electronic Structure of MAX Phase Compound Cr_2AlC Studied by Angle-resolved Photoemission Spectroscopy

T. Ito[1, 2], T. Fujita[2], D. Pinek[3], M. Nakatake[4], S. Ideta[5], K. Tanaka[5] and T. Ouisse[3]

[1]*Synchrotron Radiation Research Center, Nagoya University, Nagoya 464-8603, Japan*
[2]*Graduate School of Engineering, Nagoya University, Nagoya 464-8603, Japan*
[3]*Université Grenoble-Alpes, CNRS, LMGP, F-38000 Grenoble, France*
[4]*Aichi Synchrotron Research Center, Seto, 489-0965, Japan*
[5]*Institute for Molecular Science, Okazaki 444-8585, Japan*

MAX phase compounds, i.e., $M_{n+1}AX_n$ where M is a transition metal, A belongs to groups 13-16 and X is the C or N element, have recently attracted much attention due to their possible application to the production of a new class of two-dimensional systems called MXenes, obtained by removing the A atom planes [1]. On the other hand, the bulk electronic structure of MAX phase has been studied mostly through *ab initio*, density functional theory (DFT) calculations, mainly due to a lack of single crystalline samples. In this study, we have for the first time performed angle-resolved photoemission spectroscopy (ARPES) on single crystals of the MAX phase compound Cr_2AlC [2] in order to directly investigate the bulk electronic structure of this system.

ARPES measurements were performed at the beamline BL5U of UVSOR-III. Clean surfaces were obtained by *in situ* cleaving.

Figure 1 shows the Fermi surface of Cr_2AlC along ΓMK plane obtained by using hν = 65 eV photons. The photon energies corresponding to high-symmetry k_z points were obtained by using normal-emission ARPES, where the inner potential has been estimated to be 15.5 eV. The band structure along the ΓK cut (orange line in Fig. 1) is shown in Fig. 2(a) together with the band calculation (Fig. 2(b) [3]). From the present ARPES study, it has been found that the electronic structure near the Fermi level (E_F) of Cr_2AlC consists of a few closed electron-like Fermi surfaces (FS's) around the Γ point (e, e') as well as hole-like FS around the M point (h). From the comparison with the band structure calculations [3], we have found that the observed Fermi surface topology seems to be consistent with the calculation. On the other hand, we have found the qualitative difference of the band width of the electron pockets, possibly due to some mass enhancement ($m^*/m_{cal.} \sim 2$) of the carriers.

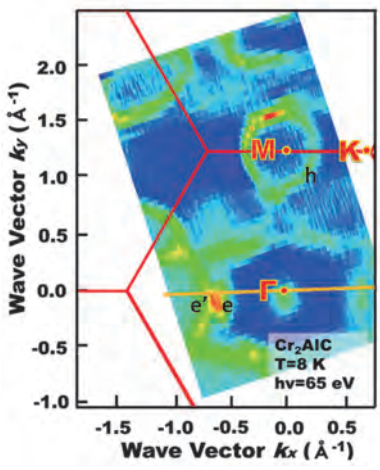

Fig. 1. Fermi surface image of Cr_2AlC along ΓMK plane. Orange line corresponds to ARPES cut shown in Fig. 2 (a).

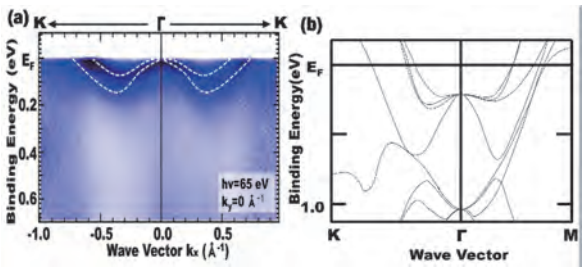

Fig. 2. (a) Band structure of Cr_2AlC along ΓK line. Dashed lines are guide for the eye. (b) Band structure calculations of Cr_2AlC [3].

[1] M. Barsoum, *MAX phases* (Wiley, Weinheim, 2013).
[2] T. Ouisse *et al.*, J. Cryst. Growth **384** (2013) 88.
[3] S. Cui *et al.*, J. Solid State Chem. **191** (2012) 147.

BL5U

Search for a Nematic State in the Cuprate Superconductor Bi2212 by Angle-resolved Photoemission Spectroscopy

S. Nakata[1], M. Horio[1], K. Koshiishi[1], K. Hagiwara[1], C. Lin[1], S. Ideta[2], K. Tanaka[2], D. Song[3], Y. Yoshida[3], H. Eisaki[3] and A. Fujimori[1]

[1]*Department of Physics, University of Tokyo, Tokyo 113-0033, Japan*
[2]*UVSOR Facility, Institute for Molecular Science, Okazaki 444-8585, Japan*
[3]*National Institute of Advanced Industrial Science and Technology (AIST), Tsukuba 305-8568, Japan*

In cuprate superconductors, to understand the origin of the pseudogap region in the phase diagram remains a most significant issue. Recently, experimental evidence for several kinds of order (e.g. charge density wave, spin density wave, electronic nematic order) has been reported in the pseudogap region [1]. Electronic nematicity, which does not break the translational symmetry but breaks the fourfold rotational symmetry of the lattice, has been reported below the pseudogap temperature and may play an important role in the pseudogap region [2]. For instance, evidence for electronic nematicity appeared in $YBa_2Cu_3O_{6+x}$ from transport [3, 4], neutron scattering [5] and magnetic susceptibility [6] measurements and in $Bi_2SrCaCu_2O_{8+\delta}$ from resistivity measurement [7].

Electronic nematicity has been discussed also in Fe-based superconductors [8] and studied by angle-resolved photoemission spectroscopy (ARPES) [9], which is the most direct way to reveal the electronic structure. However, at the moment, there has been no report that reveals the electronic nematicity in cuprates by ARPES. We performed ARPES measurements in order to study the electronic nematicity in cuprates. Furthermore, by ARPES one can investigate whether the electronic nematicity is specific to the pseudogap state or remains in the superconducting state.

$Bi_{1.7}Pb_{0.5}Sr_{0.9}CaCu_2O_{8+\delta}$ (Pb-Bi2212) single crystal samples were grown by the floating-zone method. It was nearly optimally doped sample and T_c was 91 K. ARPES measurements were carried out at UVSOR BL5U. We used linearly polarized light with $h\nu$ = 60 eV. The total energy resolution was set at 10 meV. The samples were cleaved *in-situ* under the pressure of ~ 2 × 10^{-8} Pa. In order to obtain big signals of electronic nematicity, mechanical strain was applied in the direction of the Cu-O bond.

Figure 1 shows Fermi surface plots determined from momentum distribution curves at the Fermi level taken at 200 K, 100 K, 50 K and 5 K. In order to detect the possible anisotropy of the Fermi surface, we used tight-binding fitting function with x and y axis anisotropy ($\varepsilon(k_x,k_y)$ = $-2t[(1+\delta)\cos k_x+(1-\delta)\cos k_y]$ – $4t'\cos k_x\cos k_y$ $-2t''(\cos 2k_x+\cos 2k_y)$ + E_0). Figure 2 shows the temperature dependence of the anisotropy parameter δ, representing anisotropy in the tight-binding parameter. So far, we have not been able to identify definitive evidence for electronic nematicity due to the lack of accuracy. Further measurements with improved accuracy are necessary.

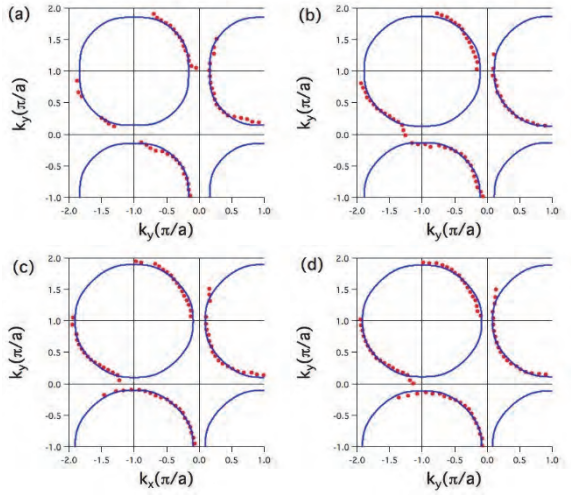

Fig. 1. Fermi surface plots (red points) and fitting curves (blue line) at (a) 200 K, (b) 100 K, (c) 50 K and (d) 5 K, respectively.

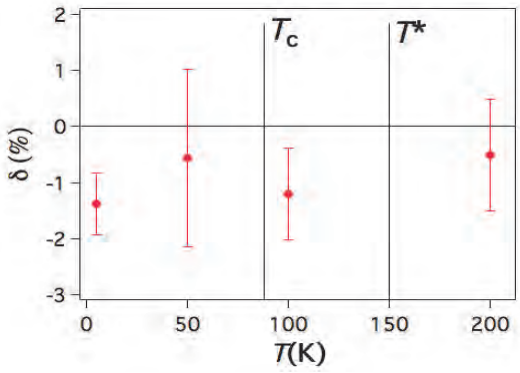

Fig. 2. Temperature dependence of δ representing the anisotropy of the nearest-neighbor tight-binding parameter *t*.

[1] B. Keimer *et al.*, Nature **518** (2015) 179.
[2] S. A. Kivelson *et al.*, Nature **393** (1998) 550.
[3] Y. Ando *et al.*, Phys. Rev. Lett. **88** (2002) 137005.
[4] R. Daou *et al.*, Nature **463** (2010) 519.
[5] V. Hinkov *et al.*, Science **319** (2008) 597.
[6] Y. Sato *et al.*, JPS fall meeting (2016) 14pJC-5.
[7] K. Ishida *et al.*, JPS fall meeting (2016) 14pJC-12.
[8] S. Kasahara *et al.*, Nature **486** (2012) 382.
[9] M. Yi *et al.*, PNAS **108** (2011) 6878.

BL5U

Preparation of Au(111) Reconstructed Surfaces Toward the Understanding of Fe/Au Spin-orbit Coupled Interfaces

J. Okabayashi[1*], S. Ideta[2] and K. Tanaka[2]
[1]*Research Center for Spectrochemistry, University of Tokyo, Tokyo 113-0033, Japan*
[2]*UVSOR, Institute of Molecular Science, Okazaki 444-8585, Japan*

The gold Au(111) surfaces are investigated extensively by means of scanning tunneling microscopy and angle-resolved photoemission spectroscopy (ARPES) because this surface exhibits the large Rashba-type spin-orbit splitting. Large spin-orbit interaction in the heavy element of gold brings the wide varieties for the topological physics and spin-orbit coupled sciences not only in the bulk but also in the surface and interfaces. The Rashba splitting of 110 meV in Au(111) surface was reported firstly by LaShell *et al.* [1]. Recently, the interfaces between Au(111) and other heavy elements such as Bi or Ag have been researched extensively [2, 3]. On the other hand, the interfaces between Au(111) and functional molecules are also investigated [4]. Here, we focus on the interfaces between ferromagnetic materials and Au(111) interfaces because the thin Fe layers on the heavy elements exhibit the perpendicular magnetic anisotropy (PMA) through the spin-orbit interaction.

In the research fields of *spintronics*, the spin-orbit coupling between the ferromagnetic 3*d* transition metal Fe or Co and 5*d* heavy elements of non-ferromagnetic materials such as Pt and Au has been utilized for the PMA through the proximity at the interfaces. It is believed that the future researches concerning not only spins but also orbitals are recognized as the *orbitornics*. Therefore, to clarify the origin of the PMA at these interfaces is a crucial role for future *spin-orbitronics*. The relationship between Au(111) Rashba-type spin-orbit interaction and PMA in 3*d* TMs has not been clarified explicitly. In order to investigate the orbital-resolved states in the Fe films showing the PMA, ARPES at the interfaces becomes the powerful techniques through the photon-energy and polarization dependences in each 3*d* orbital. By using ARPES, we aim to understand the orbital-resolved electronic structures at the magnetic interfaces on Au(111) Rashba-type surfaces in order to develop the researches of novel PMA using spin-orbit coupled interfaces.

In the project proposed in 2016, we planned to prepare the clean Au(111) surface for the deposition of Fe. The single-crystalline 200-nm-thick Au(111) films grown on mica (Phasis, Switzerland) were used as substrates. At the beamline 5U in UVSOR, we performed the Ar-ion sputtering at 1 kV accelerating voltage and subsequent annealing at 500 °C under the high vacuum conditions with repeated cycles. After the preparation, the samples were transferred to the ARPES chamber. We performed ARPES at 160 K using the photon energy of 45 eV because of the large cross-section of Au(111) surface states.

We successfully detected the band dispersions in the Au(111) surface states are shown in Fig. 1. The parabolic dispersions derived from the surface states are observed. Clear Rashba splitting in the mapping of surface states can be observed.

Considering this experiment, we plan to detect more precise band dispersions and the modulation of these bands by the ultra-thin Fe deposition. In order to achieve the purpose, we will perform the following tasks;

(i) the preparation of clear Au(111) surface and the observation of low-energy diffraction patterns
(ii) the determination of precise Fe deposition rates
(iii) Au deposition onto the Fe layers.

After performing above tasks, the spin and electronic states in the Rashba-type spin-orbit coupled interfaces combining both ARPES and X-ray magnetic circular dichroism are clarified.

We acknowledge the fruitful comments and discussion with Assistant Professor H. Yamane in IMS.

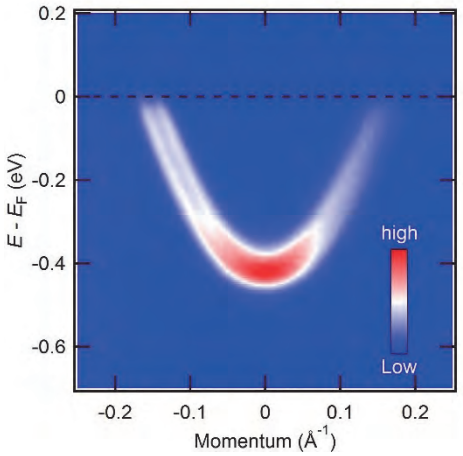

Fig. 1. ARPES of Au (111) surface states near the Fermi level.

[1] S. LaShell *et al.*, Phys. Rev. Lett. **77** (1996) 3419.
[2] C. Tusche *et al.*, Ultramicroscopy **159** (2015) 620.
[3] B. Yan *et al.*, Nature Commun. **6** (2015) 10167.
[4] H. Yamane, Molecular Science **9** (2015) A0078.

*e-mail: jun@chem.s.u-tokyo.ac.jp

BL5U

Photoemission Study on Sm-oxide Thin Films Prepared by Molecular Beam Epitaxy

H. Miyazaki[1], Y. Sakai[1], K. Yoshikawa[2] and N. Nishino[1]

[1]*Department of Physical Science and Engineering, Nagoya Institute of Technology, Nagoya 466-8555, Japan*

[2]*Department of Environmental and Materials Engineering, Nagoya Institute of Technology, Nagoya 466-8555, Japan*

Topological insulators are materials which exhibit a fundamentally new physical phenomena that were first predicted by theorists [1]. Recently, SmO is predicted to have a topological nontrivial ground state at ambient pressure [2], and we succeeded to fabricate SmO thin films by molecular beam epitaxy method controlled precisely adjusting the substrate temperature and oxygen partial pressure. However, the valence state of Sm is important for whether it is a topological insulator. In this report, we have performed *in-situ* photoemission spectroscopy (PES) on SmO thin films.

Sm-metal and Sm-oxide thin films have been grown by molecular beam epitaxy (MBE) method. We evaporated Sm-metal and Sm-oxide thin films onto Y-stabilized ZrO_2 (100) substrates at 800 °C without oxygen gas and under the oxygen pressure of 1.0 x 10^{-5} Pa, respectively. The PES measurements were performed at the beamline 5U of UVSOR-III, the Institute for Molecular Science, combined with the molecular beam epitaxy system, as shown in Fig. 1.

Figure 2 shows the PES spectra of Sm-metal and Sm-oxide thin films recorded at $h\nu$ = 60 eV and 180 eV. The experimental spectra are normalized with respect to their integrated intensity on the whole valence band up to E_B = 15 eV. The peaks and shoulder observed around 7.5, 10, and 12 eV at $h\nu$ = 180 eV are steeper than those at $h\nu$ = 60 eV. If the photon energy is increased from 60 to 180 eV, the atomic cross-sections of the O 2*p* and Sm 4*f* states change by 0.07 and 0.5 times, respectively [3]. As a result, the partial DOS originated from the Sm 4*f* state is expected to be enhanced compared with that from the O 2*p* state and the peaks and shoulder observed around 7.5, 10, and 12 eV are attributed to the Sm 4*f* state and the peak around 6.0 eV is attributed to the O 2*p* state. This hypothesis is consistent with the past PES results of Sm_2O_3 and the valence state of Sm 4*f* state is the $4f^{3+}$ state.

Sm $4f^{3+}$ valence state originates from Sm_2O_3 have been observed in PES, despite Sm $4f^{2+}$ valence state from SmO expected from the results of X-ray diffraction measurement. There is a contradiction between the results of PES and XRD measurements. Considering that the surface of the Sm-metal thin film is oxidized, one possibility is that the surface of the thin films has been oxidized during the transfer of the sample from MBE chamber to PES system. In order to discuss the essential surface electronic structure of thin films, further MBE system improvements are needed.

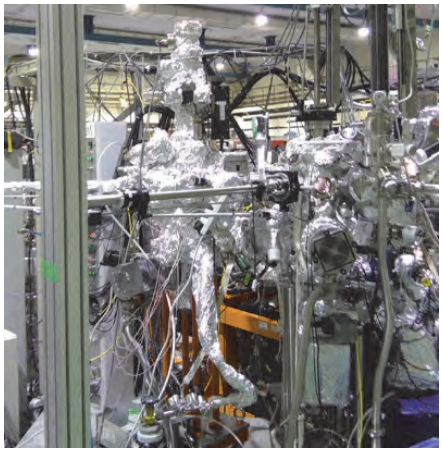

Fig. 1. Photo of the *in-situ* MBE system combined to UVSOR-III BL5U beamline.

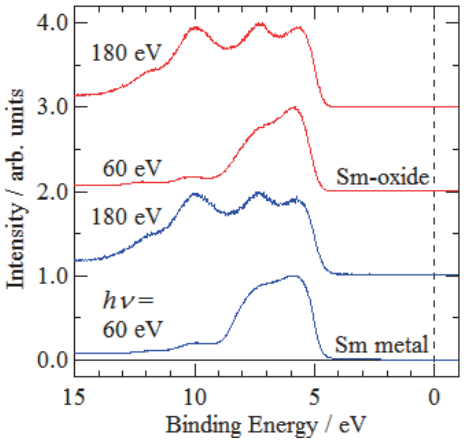

Fig. 2. Photon-energy dependence of the photoemission spectra of Sm-metal and Sm-oxide thin films.

[1] C. L. Kane and E. J. Mele, Phys. Rev. Lett. **95** (2005) 146802.
[2] D. Kasinathan *et al.*, Phys. Rev. B. **91** (2015) 195127.
[3] J. J. Yeh and I. Lindau, At. Data Nucl. Data Tables **32** (1985) 1.
[4] G. Dufour *et al.*, Chem. Phys. Lett. **42** (1976) 433.

BL5U

Angle Resolved Photoemission Spectroscopy Study of Fermi Surface and Superconducting Gap in NdFeAs(O,F)

Z. H. Tin[1], T. Adachi[1], A.Takemori[1], S. Ideta[2, 3], K. Tanaka[2, 3], S. Miyasaka[1] and S. Tajima[1]

[1]*Department of Physics, Graduate School of Science, Osaka University, Toyonaka 560-0043, Japan*

[2]*UVSOR Facility, Institute for Molecular Science, Okazaki 444-8585, Japan*

[3]*School of Physical Sciences, The Graduate University for Advanced Studies (SOKENDAI), Okazaki 444-8585, Japan*

Since the discovery of iron-based superconductors in 2008, intensive research has been going on in order to find out the origin of superconductivity. Among various families of Fe-based superconductors, 1111 system such as *R*FeAs(O,F) (*R*=rare-earth elements) achieves the highest T_c~ 55K [1]. In spite of highest T_c, 1111 system is not the popular research target among iron-based superconductors. The main reason is that it is very difficult to synthesize the single crystal of 1111 system. In our previous study, we have been able to grow the single crystal of NdFe(P,As)(O,F) and observe the evolution of Fermi surfaces with the isovalent doping of As site to P. In order to clarify the pairing mechanism, we have measured the superconducting gap of NdFeAs(O,F) single crystal by using angle resolved photoemission spectroscopy (ARPES) method.

The single crystals of NdFeAs(O,F) were grown by self-flux method under high pressure [2]. T_c of the single crystal was 41K. The ARPES were measured at BL5U in UVSOR facility.

Figure 1 shows the mapping of the Fermi surfaces (FSs) around Γ point, in horizontal (*P*) and vertical (*S*) polarized photon configurations. In these mapping, two hole FSs (inner and outer) were clearly observed around Γ point. Figure 2 shows k_z dependence of both FSs. Both of the FSs showed less dispersive feature along the k_z direction, which is consistent with the band calculation [3].

Superconducting gap was measured in k_x-k_y momentum space around Γ point. Figure 3 shows the angle dependence of superconducting gap values on the inner and outer FSs around Γ point. Both two hole FSs have a nodeless superconducting gap of ~17.0meV - 27.7meV on the outer FS and ~16.1meV - 23.3meV on the inner FS. These correspond to large gap ration, $2\Delta/kT_c$ = 8-12 and 9-15, respectively.

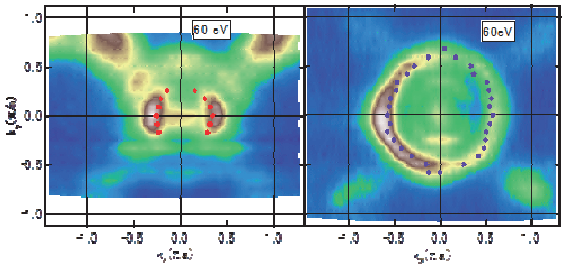

Fig. 1. Fermi surface mapping around Γ point in NdFeAs(O,F) single crystal in *S* (left panel) and *P* (right panel) polarization configurations, respectively.

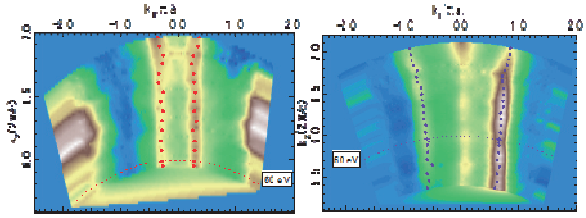

Fig. 2. The k_z dependence of Fermi surfaces in NdFeAs(O,F) single crystal in *S* (left panel) and *P* (right panel) polarization configurations, respectively.

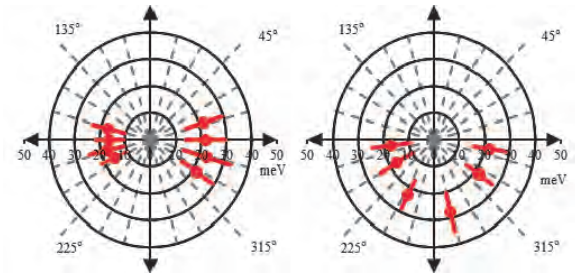

Fig. 3. The angle dependence of superconducting gap values on the inner (left panel) and outer Fermi surfaces (right panel) around Γ point, respectively.

[1] Ren Zhi-An *et al*., Chinese Phys. Lett. **25** (2008) 2215.
[2] A. Takemori *et al*., JPS Conf. Proc. **1** (2014) 012111.
[3] H. Usui *et al*., Supercond. Sci. Tech. **25** (2012) 084004.

BL6B

UV-Induced Absorption Spectra for Cerium-doped $Gd_3Al_{5-x}Ga_xO_{12}$ Crystals

M. Kitaura[1], K. Kamada[2], S. Kurosawa[1, 2], A. Ohnishi[1] and K. Hara[3]
[1]*Faculty of Science, Yamagata University, Yamagata 990-8560, Japan*
[2]*New Industry Creation Hatchery Center, Tohoku University, Sendai 980-8579, Japan*
[3]*Research Institute of Electronics, Shizuoka University, Hamamatsu 432-8011, Japan*

The cerimu-doped $Gd_3Al_2Ga_3O_{12}$ (Ce:GAGG) crystal is known one of high performance scintillators [1]. This material is characterized by high light yield and good energy resolution, and the scintillation properties are superior to other inorganic scintillators. However, there is a serious problem for Ce:GAGG that Ce^{3+} emission accompanies not only phosphorescence but also afterglow [2]. Since these components impede scintillation application requiring high-speed response, they must be suppressed as small as possible.

Most of scintillator crystals necessarily include lattice imperfections, which are unavoidably introduced in the process of the crystal growth. Such imperfections create donor- and acceptor-like levels near valence and conduction bands, and they act as traps for photocarriers. The traps are responsible for the occurrence of phosphorescence and afterglow. It is therefore necessary to clarify the origin of the traps degrading the scintillation response.

Recently, we have demonstrated that the defect complexes including oxygen vacancies form trapped electron centers in Ce:GAGG crystals [3]. We also explained that the trapped electron centers are introduced as charge compensators for cation deficiency. However, the origin of the trapped electrons center remains unsolved.

We show absorption spectra of cerium-doped $Gd_3Al_{5-x}Ga_xO_{12}$ mixed crystals induced under irradiation with UV-light at 375 nm for 10 min. The data allow us to see the effect of x on the electronic structure of trapped electron centers, and they are available to identify the origin of trapped electron centers. In the present experiment, we used the single crystals of $Ce:Gd_3Al_{5-x}Ga_xO_{12}$ grown by the micro-puling down (μ-PD) method. The concentration of cerium ions was set 1.0 mol%. The single crystals of $x < 2.5$ could not be obtained, because they contain the secondary phase with perovskite structure. The absorption spectra were measured under UV-irradiation and non-UV-irradiation. Here, the difference between the two is called as UV-induced absorption spectrum.

The UV-induced absorption spectra for x=3.0, 3.5, 4.0, and 5.0 are shown in Fig. 1. The data were obtained at 12 K. The absorption spectra cannot be obtained in the range below 1500 cm^{-1}, because of strong Reststrahlen reflection. The UV-induced absorption spectrum for x=3 exhibits a prominent band at around 12000 cm^{-1}. This feature is good agreement with our previous data in Ref. 3, in which the prominent band was assigned to trapped electron centers associated with oxygen vacancies. This band is weakened for x=3.5. Another band also appears in the range below 4000 cm^{-1}, together with the 12000 cm^{-1} band. This band is gradually increased with x.

The present results reveal that two kinds of absorption bands are replaced with increasing x. This fact suggests that gallium and aluminum ions are also essential for the formation of trapped electron centers, together with oxygen vacancies. The disappearance of the 12000 cm^{-1} band may occur also by the lowering of the conduction band minimum with increasing x [4]. Further investigations are needed to clarify the origin of the trapped electron centers responsible for the UV-induced absorption bands.

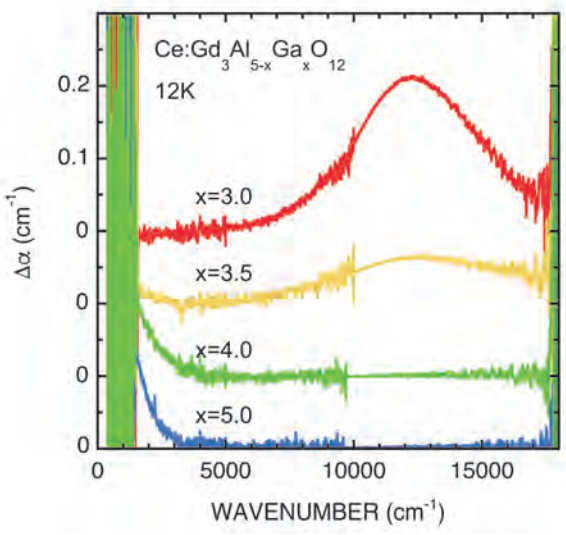

Fig. 1. UV-induced absorption spectra of $Ce:Gd_3Al_{5-x}Ga_xO_{12}$ crystals (x=3.0, 3.5, 4.0, and 5.0) measured at 12 K. The longitudinal axis represents the difference in absorption coefficient between the absorption spectra measured under UV-irradiation and non-UV-irradiation.

[1] K. Kamada *et al*., J. Cryst. Growth **352** (2012) 88.
[2] M. Kitaura *et al*., J. Appl. Phys. **115** (2014) 083517.
[3] M. Kitaura *et al*., Appl. Phys. Express **9** (2016) 072602.
[4] P. Dorenbos, J. Lumi. **134** (2013) 310.

BL6B

Ground-State Splitting of Ultrashallow Thermal Donors in Silicon

A. Hara and T. Awano
Department of Electronic Engineering, Tohoku Gakuin University, Tagajo 985-8537, Japan

We had found ultrashallow thermal donors (USTDs) in carbon-doped and hydrogen-doped Czochralski silicon (CZ Si) crystals.[1] To the best of our knowledge, these are the shallowest energy levels among previously reported donors in Si crystals. We found new peaks with increasing measurement temperature.

To evaluate the relationship between the absorption coefficient of the new peaks and the measurement temperature, we analyzed the temperature dependence of the absorption coefficient. We assumed that absorption coefficient at 15 K to be zero to simplify the analysis, and that absorption coefficient is proportional to $N_0 \times \exp(-\Delta E/k_B T)$, where ΔE, N_0, and k_B are the activation energy for occupying the new peak state, the total population, and the Boltzmann constant, respectively. Figure 1(a) plots ln[Trans.(T)/Trans.(15 K)] at various measurement temperatures T (in units of kelvin), where Trans.(T) represents the transparent coefficient at T K. Figure 1(b) shows a magnification around spectral peaks A and B. Because we assumed the absorption coefficient of the new peaks at 15 K to be zero, the vertical values are correlated with their absorption coefficient at T K. Figure 2 plots the variation of the intensity of peak B in Fig. 1(b) as a function of 1/T. The vertical axis expresses ln{-ln[Trans.(T)/Trans.(15 K)]}. The gradient of this curve is $-\Delta E/k_B$, implying ΔE = 6 meV. This magnitude is reasonable because we observed the new peaks with a thermal energy of $k_B T$ (T = 20–40 K), of 2–4 meV. The reduction of the absorption coefficient above 40 K is attributed to the excitation of electrons to the conduction band.

We propose the following model to explain the origin of the new peaks (A and B). These lines are associated with the excitation of electrons from the upper level of the ground state to the original $2p_0$, $2p_{+-}$, and $3p_{+-}$ states of the USTDs, arising from the level splitting of the ground-state. This model is consistent with the thermal excitation energy of 6 meV required to generate new peaks because the optical energy-level splitting between the upper level of the ground state and the ground state is approximately 4 meV.

Ground-state splitting indicates that the wave functions of the ground state of the USTDs are composed of linear combinations of the wave functions of the conduction-band minimum.

In summary, the ground-state splitting of the USTDs was observed. This is the direct evidence that the ground state of the USTDs is composed of linear combinations of wave functions of the conduction band minimum.

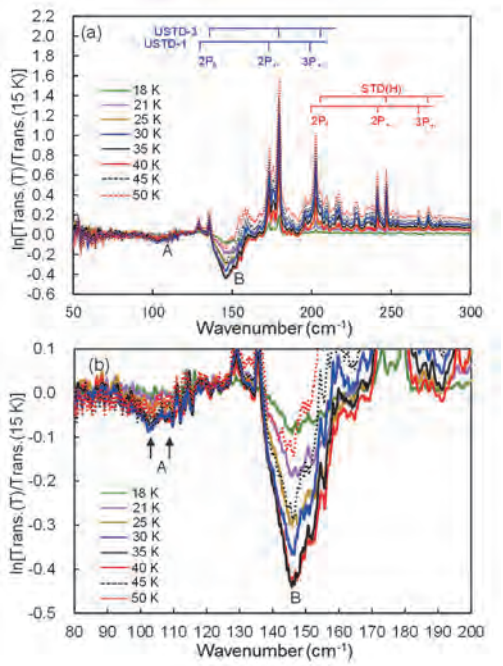

Fig. 1. Temperature dependence of the absorption coefficient. The vertical axis is ln[Trans.(T)/Trans.(15 K)], where Trans.(T) represents the transmittance at temperature T K. (b) Magnified image of spectra A and B.

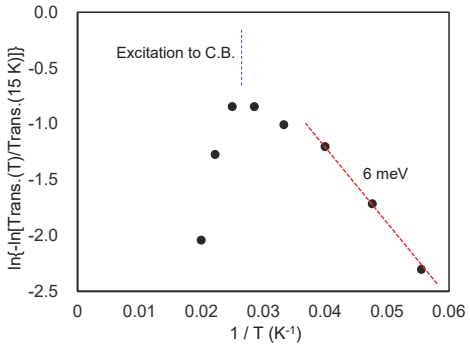

Fig. 2. Temperature dependence of the absorption coefficient of the new shallow donor. The vertical axis is ln{-ln[Trans.(T)/Trans.(15 K)]}. The gradient reflects the thermal activation energy.

[1] A. Hara, T. Awano, Y. Ohno and I. Yonenaga, Jpn. J. Appl. Phys. **49** (2010) 050203.

BL6B

Far-Infrared Reflective Analysis for Unipolar Fatigued Alkali Niobate Piezoceramics

H. Nishiyama, N. Matsubara, K. Yoshida, D. Ando, T. Fuchigami and K. Kakimoto
Graduate School of Engineering, Nagoya Institute of Technology, Nagoya 466-8555, Japan

Electromechanical property of piezoceramics changes due to a long-term and repeated exposure to high unipolar electric fields. Although some fatigue mechanisms of the electromechanical property have been discussed based on a change of domain structure [1], an experimental fact has not been showed directly. Previously, we have reported that it is possible to clarify the difference in permittivity ε' of piezoceramics by analyzing IR reflectivity spectra [2]. In this study, we thought it was possible to clarify the change of domain structure before/after fatigue experiment by investigating the difference of the permittivity in alkali niobate piezoceramics with far-infrared (FIR) reflectivity analysis. Especially, we focused on ionic polarization in perovskites because FIR analysis has been used to explain soft-mode theory for displacive type of ferroelectric perovskites [3].

Alkali niobate piezoceramic, $Li_{0.06}Na_{0.52}K_{0.42}NbO_3$ with additives (Li_2CO_3, SiO_2, $MnCO_3$, and $SrZrO_3$) (NKN-additive), was polarized in silicon oil under DC field up to 4 kV/mm. Fatigue tests was carried out for specimens under unipolar triangle waves up to 10^6 cycles by applying electric field of 0 - 3 kV/mm with a frequency of 50 Hz. FIR measurement was conducted by a FT-IR spectrometer (Bruker, VERTEX 70v). A beam splitter and detector were used a Mylar 6 μm and Si bolometer, respectively. The spectra were fitted to obtain complex permittivity according to Drude-Lorentz equation:

$$\varepsilon(\omega) = \varepsilon_\infty + \sum_j \frac{\omega_{jp}^2}{\omega_{jTO}^2 - \omega^2 - n\gamma_j\omega} \quad (1)$$

where, ε_∞ is the high-frequency dielectric constant, ω_p and ω_{TO} are the plasma and transverse optic frequencies, and γ is the damping constant. The complex dielectric function $\varepsilon^*(\omega) = \varepsilon'(\omega) - i\varepsilon''(\omega)$ is related to the reflectivity R by Fresnel equation:

$$R(\omega) = \left|\frac{\sqrt{\varepsilon^*(\omega)} - 1}{\sqrt{\varepsilon^*(\omega)} + 1}\right|^2 \quad (2)$$

Figure 1 shows FIR reflectivity spectra for NKN-additive. Peak shifts and a change of waveforms were observed in all wavenumber range after polarization (As-poled) and fatigue treatment (Fatigued). Figure 2 shows real part (ε') and imaginary part (ε'') of permittivity calculated from the FIR reflectivity spectra shown in Fig.1. The ε'' peak shifted from 88.2 cm^{-1} to 53.8 cm^{-1} with increasing intensity from 54.9 to 450.5 after polarization treatment. After the fatigue treatment, the peak shifted to 65.4 cm^{-1} with decreasing intensity to 109.3. A similar tendency was observed in the ε'. On the assumption that the ε'' peak relates to the Slater mode (Nb-O vibrations), these results imply reduction of Nb-O ionic polarization getting back to the virgin state. Thus, we believe that FIR analysis is useful as an experimental method to reveal the fatigue mechanisms of the electromechanical property.

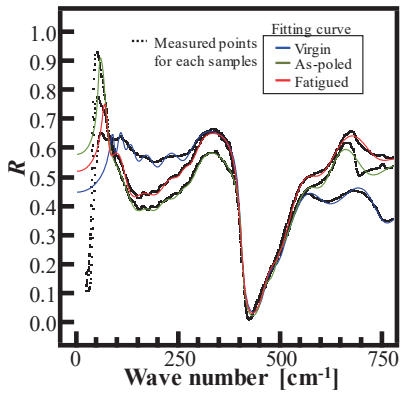

Fig. 1. FIR reflectivity spectra for NKN-additive. Dot lines indicate measured points. Colored lines indicate fitting curves for each measured points.

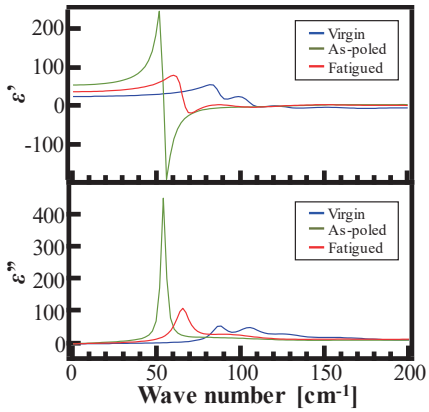

Fig. 2. Real and imaginary part of permittivity for NKN-additive calculated from FIR reflectivity spectra.

[1] F-Z. Yao *et al.*, Appl. Phys. Lett. **103** (2013) 192907.
[2] Y. Taniguchi and K. Kakimoto, Jpn. J. Appl. Phys. **54** (2015) 10ND09.
[3] J. L. Servoin and F. Gervais, Phys. Rev. B **21** 5 (1980) 2038.

BL7U

ARPES Study of Possible Topological Superconductor $Tl_{0.5}Bi_2Te_3$

C. X. Trang[1], Z. Wang[2], D. Takane[1], K. Nakayama[1], S. Souma[3, 4], T. Sato[1, 4], A. A. Taskin[2], Y. Ando[2] and T. Takahashi[1, 3, 4]

[1]*Department of Physics, Tohoku University, Sendai 980-8578, Japan*
[2]*Institute of Physics II, University of Cologne, Köln 50937, Germany*
[3]*WPI Research Center, Advanced Institute for Materials Research, Tohoku University, Sendai 980-8577, Japan*
[4]*Center for Spintronics Research Network, Tohoku University, Sendai 980-8577, Japan*

The discovery of topological insulators (TIs), in which a gapless topological surface state (SS) with a Dirac-cone energy dispersion appears at the edge or surface, has stimulated intensive investigations into an even more exotic state of matter, a topological superconductor (TSC). TSCs generically possess a gapless Andreev bound state at the edge or surface which consists of Majorana fermions [1]. Owing to the peculiar characteristics of Majorana fermions and the potential application to a fault-tolerant quantum computer, TSC is one of the emergent topics in current condensed-matter physics. It has been suggested that a superconductor derived from a TI is a promising candidate for a TSC because of the strong spin-orbit coupling that would lead to unconventional electron pairing. However, only a limited number of candidate materials, such as $Cu_xBi_2Se_3$, $Cu_x(PbSe)_5(Bi_2Se_3)_6$, and $Sr_xBi_2Se_3$, have been discovered and their topological properties are still under intensive debate. It is thus of great importance to explore new platforms of TSCs and establish the electronic structure to investigate the possible topological superconductivity.

In this study, we report high-resolution angle-resolved photoemission spectroscopy (ARPES) on a new TSC candidate, $Tl_{0.5}Bi_2Te_3$ (T_c = 2.28 K) [2], which is derived from thallium (Tl) doping into a prototypical TI, Bi_2Te_3. By utilizing energy-tunable photons from synchrotron radiation, we determined the bulk and surface electronic states and found that $Tl_{0.5}Bi_2Te_3$ provides an excellent platform to realize topological superconductivity [3].

Figure 1(a) shows the experimental Fermi surface (FS) measured with $h\nu$ = 21 eV whose k cut nearly crosses the Z point of the bulk Brillouin zone. The FS consists of three large and three small pockets slightly away from the Z point. These FSs commonly have a hole-like character as recognized from the Fermi level (E_F) crossing of the valence band (VB) in Fig. 1(b). This demonstrates that Tl doping leads to a direct hole doping into the VB top. Besides the M-shaped VB feature, we found a V-shaped electron-like band in the vicinity of E_F inside the valley of the VB. This tiny feature is assigned to a topological SS. This indicates that the band-inverted nature is conserved even upon Tl doping. As shown in Fig. 1(c), we were able to trace the dispersion of the SS up to ~0.2 eV above the VB top simply by keeping the samples in a vacuum of 2 × 10^{-10} Torr for 12 h, which resulted in a significant downward surface band bending. Since the surface chemical potential can be systematically controlled by the surface-aging technique, it is possible to well isolate the topological SS from the bulk bands in both the k space and the energy axis by controlling the strength of the surface band bending. This is in favor of the realization of 2D topological superconductivity in the topological SS through the proximity effect from the SC bulk. In this regard, the $Tl_xBi_2Te_3$ system provides an excellent platform to realize the 2D topological superconductivity.

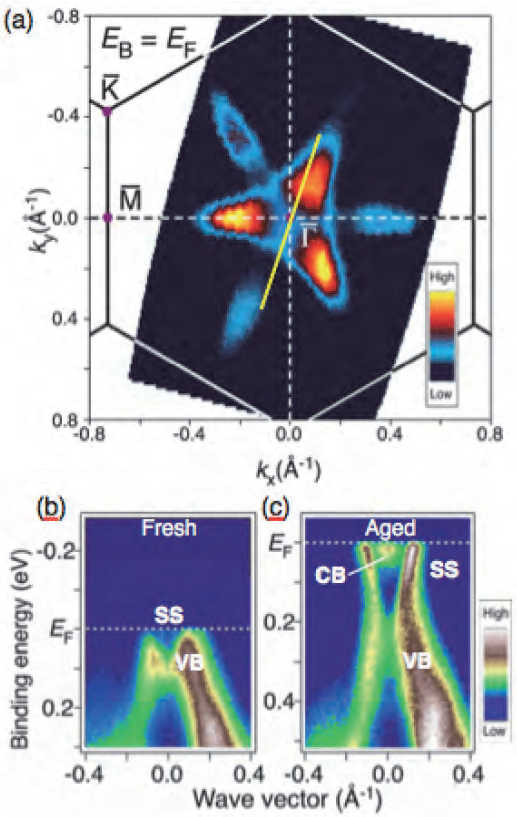

Fig. 1. (a) APRES intensity at E_F in $Tl_{0.5}Bi_2Te_3$ plotted as a function of 2D wave vector. (b) and (c) Experimental band dispersion along yellow line in (a) measured just after cleaving (fresh) and 12 h after cleaving (aged), respectively.

[1] Y. Ando, J. Phys. Soc. Jpn. **82** (2013) 102001.
[2] Z. Wang *et al.*, Chem. Mater. **28** (2016) 779.
[3] C. X. Trang *et al.*, Phys. Rev. B **93** (2016) 241103(R).

BL7U

Slater to Mott Crossover in the Metal to Insulator Transition of $Nd_2Ir_2O_7$

M. Nakayama[1], T. Kondo[1], Z. Tian[1], J. J. Ishikawa[1], M. Halim[1], C. Bareille[1], K. Kuroda[1], T. Tomita[1], S. Ideta[2], K. Tanaka[2], M. Matsunami[3], S. Kimura[4], L. Balents[5], S. Nakatsuji[1] and S. Shin[1]

[1]*ISSP, University of Tokyo, Kashiwa 277-8581, Japan*
[2]*UVSOR Facility, Institute for Molecular Science, Okazaki 444-8585, Japan*
[3]*Toyota Technological Institute, Nagoya 468-8511, Japan*
[4]*Graduate School of Frontier Biosciences, Osaka University, Suita 565-0871, Japan*
[5]*Kavli Institute for Theoretical Physics, Santa Barbara, California 93106, USA*

The 5*d* iridium oxides (iridates), having comparable scales for their kinetic energy, Coulomb interaction, and spin-orbit coupling, provide an excellent platform for studying new types of strongly correlated phenomena. Amongst them, the pyrochlore iridates ($Ln_2Ir_2O_7$, where *Ln* is a lanthanide), endowed with frustrated geometry and cubic symmetry, have a particularly fascinating phase diagram. $Pr_2Ir_2O_7$, with the largest *Ln* ion, is a metallic spin liquid and exhibits an anomalous Hall effect. For *Ln* ions with a smaller ionic radius, an antiferromagnetically ordered insulating phase appears at low temperature.

Theoretically, topological band structures have been ascribed to the $Ln_2Ir_2O_7$ series. The metallic phase is predicted to exhibit quadratically, dispersing conduction and valence bands touching at the Γ point close to the Fermi level (E_F). We have recently identified this structure by angle-resolved photoemission spectroscopy (ARPES) in $Pr_2Ir_2O_7$ [1]. Theory predicts that such a quadratic Fermi node state may be converted into various topological states such as a topological insulator or a Weyl semimetal by appropriate symmetry breaking.

Antiferromagnetism in these materials is of the Ising type, consisting of an "all-in–all-out" (AIAO) configuration of Ir moments on alternating tetrahedra. This can be considered an "octupolar" spin order which breaks time-reversal but preserves cubic symmetry, and does not enlarge the unit cell. Early density functional studies predicted the magnetic state to be a Weyl semimetal, and general arguments imply that, if a quasiparticle picture applies at low energy in the antiferromagnetic phase, and the magnetic ordering is weak, it must exhibit Weyl points and cannot have a true gap. Nevertheless, optical and transport measurements indicate a gapped insulating ground state for $Nd_2Ir_2O_7$, despite its low antiferromagnetic–metal-insulator (MI) transition temperature $T_{MI} \approx 30$ K and proximity to metallic $Pr_2Ir_2O_7$. This begs the question of whether the weakness of the order, the quasiparticle assumption, or both, break down in this system. More generally, we seek to understand the influence of the MI transition on the conduction electrons.

We use ARPES to investigate the evolution of the electronic structure through the MI transition in $Nd_2Ir_2O_7$, which is the most suitable member of the series for such study because its low T_{MI} minimizes thermal broadening. Although the layered iridates have been extensively studied by photoemission, ours is the first study across a MI transition in any iridate, since the latter occurs only in the pyrochlores. Using high-quality single crystals, we are able to directly measure both the single particle excitations of the metallic and insulating phases. Our data in Fig. 1 indicate that $Nd_2Ir_2O_7$ displays a dramatic Slater to Mott crossover with reducing temperature [2]. This implies that Weyl fermions, if they exist, may do so only in a narrow region of temperature slightly below T_{MI}, in which the order is, indeed, weak and quasiparticles can survive.

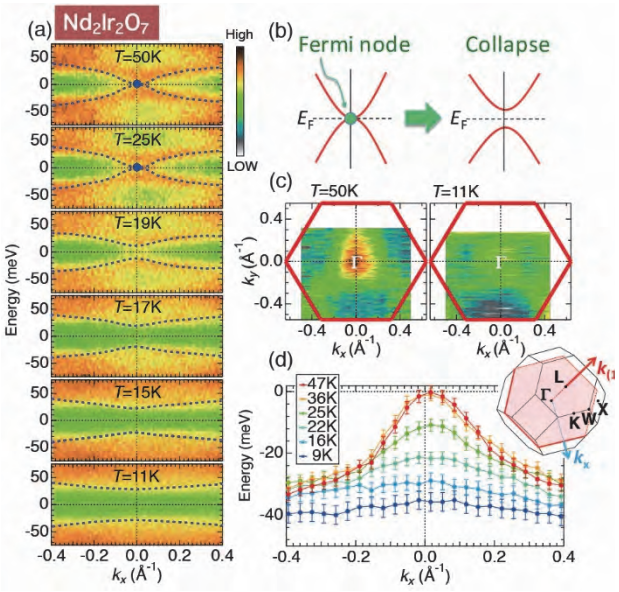

Fig. 1. Temperature evolution of ARPES dispersion map across Γ showing a quadratic Fermi node state in the metallic phase of $Nd_2Ir_2O_7$, and its destruction upon cooling below T_{AF}.

[1] T. Kondo *et al.*, Nat. Commun. **6** (2015) 10042.
[2] M. Nakayama *et al.*, Phys. Rev. Lett. **117** (2016) 056403.

BL7U

d-wave Superconducting Gap Observed in the Protect-annealed Electron-doped Cuprate Superconductor $Pr_{1.3-x}La_{0.7}Ce_xCuO_4$

M. Horio[1], K. Koshiishi[1], S. Nakata[1], K. Hagiwara[1], S. Ideta[2], K. Tanaka[2], A. Takahashi[3], T. Konno[3], T. Ohgi[3], T. Adachi[4], Y. Koike[3] and A. Fujimori[1]

[1]*Department of Physics, University of Tokyo, Tokyo 113-0033, Japan*
[2]*UVSOR Facility, Institute for Molecular Science, Okazaki 444-8585, Japan*
[3]*Department of Applied Physics, Tohoku University, Sendai 980-8579, Japan*
[4]*Department of Engineering and Applied Sciences, Sophia University, Tokyo 102-8554, Japan*

The symmetry of the superconducting (SC) gap provides a strong clue for the origin of unconventional superconductivity. As for the electron-doped cuprate superconductors, most of the previous studies have supported *d*-wave symmetry [1, 2], and large contribution of antiferromagnetic (AF) spin fluctuations to the superconductivity has been proposed.

Recently, a new annealing method, which is called protect-annealing, has enabled superconductivity in electron-doped cuprates with lower Ce concentration than that in previous studies [3]. This is probably because the impurity apical oxygen atoms which stabilize short-range antiferromagnetic (AF) order have been efficiently removed by the improved annealing. Our recent ARPES study on protect-annealed $Pr_{1.3-x}La_{0.7}Ce_xCuO_4$ (PLCCO, x = 0.10) has revealed strong suppression of the AF pseudogap, suggesting a dramatic reduction of the AF spin correlation length and/or the magnitude of the fluctuating magnetic moments [4]. In order to investigate the nature of the SC state with a high T_c and suppressed antiferromagnetism, we have performed ARPES measurements on protect-annealed PLCCO (x = 0.10, 0.15) single crystals and directly observed a momentum-dependent SC gap.

Single crystals of PLCCO with x = 0.10 (samples #1-#3) and 0.15 (samples #4 and #5) were synthesized by the traveling-solvent floating-zone method and were protect annealed for 24 hours at 800 °C. After the annealing, samples with x = 0.10 and x = 0.15 showed T_c's of 27 K and 22 K, respectively. ARPES measurements were performed at beamline 7U of UVSOR facility. Linearly polarized light with $h\nu$ = 16.5 eV was used for the measurements. The total energy resolution was set at 8 meV. Considering the relatively quick surface degradation which is typical for electron-doped cuprates, ARPES spectra were recorded within 4 hours after cleavage at only one momentum position at two temperatures below and above T_c for each sample.

Figure 1(a) shows energy distribution curves (EDCs) of PLCCO (x = 0.10) at the Fermi wave vector (k_F) near (π/2, π/2) and (0.3π, π), which are in the nodal and antinodal regions, respectively, in the case of d_{x2-y2}-wave paring. We compared the spectra taken above and below T_c and estimated the magnitude of the leading-edge shift Δ_{shift} caused by the opening of SC gap. EDCs near (π/2, π/2) taken above and below T_c cross almost at E_F and Δ_{shift} is as small as 0.3 meV. On the other hand, those near (0.3π, π) cross appreciably below E_F and a leading-edge shift of 1.3 meV was observed, which is also confirmed in the measurements on another x = 0.10 sample as shown in Fig. 1(b). The same tendency also applies to the x = 0.15 samples (Fig. 1(c)).

The present result suggests that d_{x2-y2}-paring, which is associated with strong electron correlation and AF spin fluctuations, persists after the strong reduction of AF correlation length and/or magnitude of the fluctuating magnetic moment by protect annealing. The short-range AF order induced around the apical oxygen atoms is harmful for superconductivity, but it is still possible that electron correlation itself drive the d_{x2-y2}-wave SC state in the electron-doped cuprates.

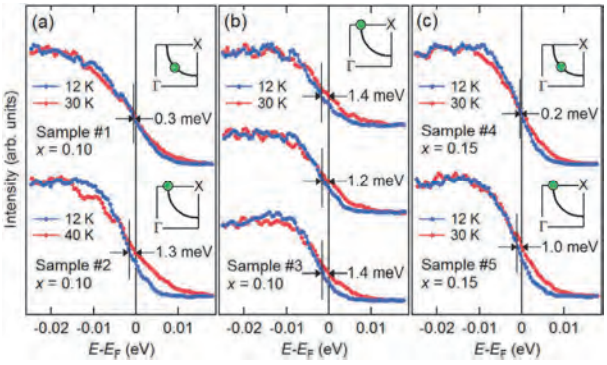

Fig. 1. Leading-edge shift observed in PLCCO samples. EDCs of (a) samples #1 and #2 with x = 0.10, (b) sample #3 with x = 0.10, and (c) samples #4 and #5 with x = 0.15 measured at temperatures above (red curves) and below (blue curves) T_c. Insets indicate the k_F positions where the EDCs were taken.

[1] G. Blumberg *et al.*, Phys. Rev. Lett. **88** (2002) 107002.
[2] H. Matsui *et al.*, Phys. Rev. Lett. **95** (2005) 017003.
[3] T. Adachi *et al.*, J. Phys. Soc. Jpn. **82** (2013) 063713.
[4] M. Horio *et al.*, Nat. Commun. **7** (2016) 10567.

BL7U

Electronic Structure of FeS

J. Miao[1], X. H. Niu[1], D. F. Xu[1], Q. Yao[1], Q. Y. Chen[1], T. P. Ying[1], S. Y. Li[1,2], Y. F. Fang[3], J. C. Zhang[3], S. Ideta[4], K. Tanaka[4], D. L. Feng[1,2] and F. Chen[3]

[1]*State Key Laboratory of Surface Physics, Department of Physics, and Laboratory of Advanced Materials, Fudan University, Shanghai 200433, People's Republic of China*

[2]*Collaborative Innovation Center of Advanced Microstructures, Nanjing, 210093, China*

[3]*Materials Genome Institute, Shanghai University, Shanghai 200444, People's Republic of China*

[4]*UVSOR Synchrotron Facility, Institute for Molecular Science, Okazaki 444-8585, Japan*

Among all the iron-based superconductors, the iron-chalcogenide FeSe has the simplest layered structure yet extraordinarily rich physics [1]. The most remarkable one is the interfacial superconductivity as high as 65 K in FeSe monolayer thin film grown on $SrTiO_3$ (001) substrate, which has attracted great attention of the community [2].

As a counterpart, the bulk FeSe processes a superconducting transition temperature of about 8K. It will be further enhanced by hydrostatic pressure, surface dosing or liquid gating to around 40K [3-5]. Element substitution in the bulk is another effective way to explore the properties of FeSe. Recently, it was found that by dilute S doping, the transition temperature of $FeSe_{1-x}S_x$ is first enhanced, then decreases upon further substitution. The end member of this series, FeS, is still superconducting with a T_c of 4.5 K[6-7]. The presence of superconductivity in FeS is quite surprising, since S substitution is expected to significantly reduce the electron correlations which are crucial for the unconventional superconductivity. To address this surprise, we performed angle-resolved photoemission spectroscopy (ARPES) at BL7U to examine the electronic structure of FeS.

Here we report the electronic structure of FeS. Our high-resolution ARPES studies show two hole-like (α and β) and two electron-like (η and δ) Fermi pockets around the Brillouin zone center and corner, respectively, all of which exhibit moderate dispersion along k_z. However, a third hole-like band (γ) is not observed, which is expected around the zone center from band calculations and is common in iron-based superconductors. Since this band has the highest renormalization factor and is known to be the most vulnerable to impurities, its absence in our data is likely due to impurity scattering and yet superconductivity can exist without coherent quasiparticles in the γ band. This may help resolve the current controversy on the superconducting gap structure of FeS. Moreover, by comparing the β bandwidths of various iron chalcogenides, including FeS, $FeSe_{1-x}S_x$, FeSe, and $FeSe_{1-x}Te_x$, we find that the β bandwidth of FeS is the broadest. However, the band renormalization factor of FeS is still quite large, when compared with the band calculations, which indicates sizable electron correlations. This explains why the unconventional superconductivity can persist over such a broad range of isovalent substitution in $FeSe_{1-x}Te_x$ and $FeSe_{1-x}S_x$.

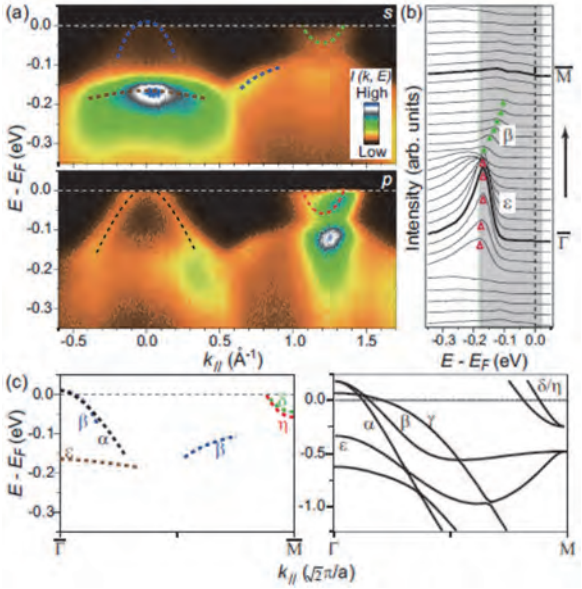

Fig. 1. (a) Photoemission intensity distributions along the Γ-M direction taken with *s*- and *p*-polarized photons, respectively. (b) Corresponding energy distribution curves of data in panel (a) taken with s-polarized photons. (c) Left panel: the band structure of FeS measured by ARPES. Right panel: the calculated FeS band structure along Γ-M reproduced from Ref. [8]. All the ARPES data were taken with 30 eV photons.

[1] F. C. Hsu, J. Y. Luo, K. W. Yeh, *et al.*, Proc. Natl. Acad. Sci. U.S.A. **105** (2008) 14262.
[2] Q. Y. Wang, Z. Li, W. H. Zhang, *et al.*, Chin. Phys. Lett. **29** (2012) 037402.
[3] S. Medvedev, T. M. McQueen, I. A. Troyan, *et al.*, Nature Mater. **8** (2009) 630.
[4] B. Lei, J. H. Cui, Z. J. Xiang, *et al.*, Phys. Rev. Lett. **116** (2016) 077002.
[5] C. H. P. Wen, H. C. Xu, C. Chen, *et al.*, Nat. Commu. **7** (2016) 10840.
[6] X. F. Lai, H. Zhang, Y. Q. Wang, *et al.*, J. Am. Chem. Soc. **137** (2015) 10148.
[7] U. Pachmayr, N. Fehn, and D. Johrendt, Chem. Commun. **52** (2016) 194.
[8] A. Subedi, *et al.*, Phys.Rev. B **78** (2008) 134514.

BL7U

High-Resolution ARPES Study of Topological Line-Node Semimetal HfSiS

D. Takane[1], Z. Wang[2], S. Souma[3, 4], K. Nakayama[1], C. X. Trang[1], T. Sato[1, 4], Y. Ando[2] and T. Takahashi[1, 3, 4]

[1]*Department of Physics, Tohoku University, Sendai 980-8578, Japan*
[2]*Institute of Physics II, University of Cologne, Köln 50937, Germany*
[3]*WPI Research Center, Advanced Institute for Materials Research, Tohoku University, Sendai 980-8577, Japan*
[4]*Center for Spintronics Research Network, Tohoku University, Sendai 980-8577, Japan*

Topological semimetals are recently attracting a great deal of attention. In contrast to conventional semimetals with a finite band overlap between valence band (VB) and conduction band (CB), topological semimetals are categorized by the band- contacting nature between the VB and CB in the Brillouin zone (BZ); point-contact (Dirac/Weyl semimetals) or line-contact (line-node semimetals; LNSMs). The existence of three-dimensional Dirac semimetals was first confirmed in Cd_3As_2 and Na_3Bi, where the VB and CB contact each other at the point (Dirac point) protected by rotational symmetry of the crystal. Recent studies on noncentrosymmetric transition-metal monopnictides (TaAs family) have clarified pairs of bulk Dirac-cone bands and Fermi-arc surface states, supporting their Weyl-semimetallic nature. While the existence of Dirac/Weyl semimetals with point nodes has been confirmed experimentally, the experimental studies of LNSMs with line nodes are relatively scarce despite many theoretical calculations.

Recently, it was theoretically proposed that ZrSiO with PbFCl-type crystal structure (space group *P*4/*nmm*) and its isostructural family *WHM* [*W* = Zr, Hf, or La; *H* = Si, Ge, Sn, or Sb; *M* = O, S, Se and Te; see Fig.1 (a) for crystal structure] may host the LNSM phase protected by a glide-mirror symmetry of the crystal [1]. In this study, we performed high-resolution angle-resolved photoemission spectroscopy (ARPES) on HfSiS. By utilizing energy-tunable photons from synchrotron radiation, we determined the overall VB structure and revealed the LNSM nature of HfSiS.

HfSiS crystal consists of a stack of S-Hf-Si-Hf-S five square nets along *c* axis. A natural cleaving plane is indicated by an orange square in Fig. 1(a). The low-energy electron diffraction (LEED) measurement on the cleaved surface shows a clear 1×1 pattern [see Fig. 1(b)], demonstrating high-quality nature of the cleaved surface. Figures 1(c) and 1(d) show the ARPES-intensity plot and the corresponding second-derivative-intensity plot, respectively, in the VB region as a function of wave vector and binding energy (E_B) measured along the ΓM cut at $h\nu = 21$ eV with linear polarization. One can notice several dispersive bands; hole-like bands (α) at the Γ point with the top of dispersion at 3 eV, an undulating band (β) with the top of dispersion at 1.6 eV midway between Γ and M, and linearly dispersive bands (γ, δ) within 1.6 eV of the Fermi level (E_F). These bands are well reproduced in the band calculation [1]. According to the band calculation, the γ and δ bands are attributed to the electron-like Hf 5*d* and the hole-like Si 3*p* bands at Γ, respectively. These bands intersect each other near E_F to form line nodes in the case of negligible spin-orbit coupling (SOC) [1]. In fact, through the band-structure mapping over entire BZ, we have observed the diamond-shaped quasi-two-dimensional Fermi surface hosting line nodes. Therefore the present observation supports the LNSM nature of HfSiS.

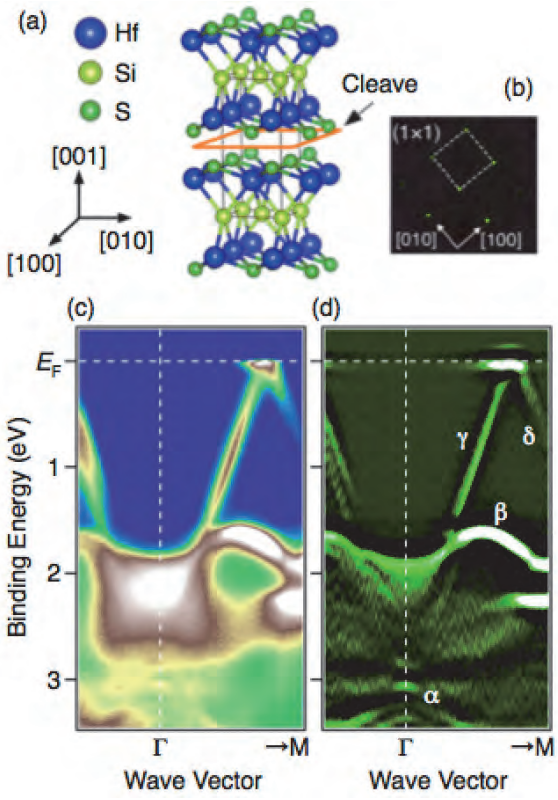

Fig. 1. (a) Crystal structure of HfSiS. (b) LEED pattern on a cleaved surface measured with a primary electron energy of 90.5 eV. (c) and (d) Plots of ARPES intensity and corresponding second- derivative intensity, respectively, in the VB region measured at T = 40 K along the ΓM line with linearly polarized 21-eV photons.

[1] Q. Xu *et al.*, Phys. Rev. B **92** (2015) 205310.

BL7U

Electronic Structure of Triple-layer Cuprate Superconductor $Bi_2Sr_2Ca_2Cu_3O_{10+\delta}$ Observed by ARPES

S. Ideta[1], T. Yoshida[2], S. Ishida[3], K. Takashima[4], S. Uchida[3, 4], A. Fujimori[4] and K. Tanaka[1]

[1]*National Institutes of Natural Science, Institute for Molecular Science, Okazaki, 444-8585, Japan*
[2]*Graduate School of Human and Environmental Studies, Kyoto University, Kyoto 606-8501, Japan*
[3]*National Institute of Advanced Industrial Science and Technology (AIST), Tsukuba 305-8568, Japan*
[4]*Department of Physics, University of Tokyo, Tokyo 113-0033, Japan*

Effects of interlayer interaction between CuO_2 planes which may contribute the enhancement of critical temperature (T_c) in the multi-layer high-T_c cuprate superconductors (HTSCs) have been investigated to elucidate the mechanism of superconductivity [1]. While it has been well known that the number of doped carriers and the number of CuO_2 planes are one of the essential factors to control the T_c of cuprates, unexpectedly T_c does not decrease in the overdoped $Bi_2Sr_2Ca_2Cu_3O_{10+\delta}$ (Bi2223) [2]. In spite of extensive studies both experimentally and theoretically [3-7], the microscopic origin of the high-T_c superconductivity in the triple-layer HTSCs still remains unclear.

We reported that the electronic structure of Bi2223 by ARPES showed two bands originating from the outer and inner CuO_2 planes [8-10], and recently we also observed the third band caused by the triple-layer splitting [11]. Here, we report an ARPES study on overdoped Bi2223 using low-energy photons and the linearly polarized synchrotron light. In this study, we found that each band shows a superconducting (SC) gap with different magnitude.

Single crystals of Bi2223 (T_c ~ 110 K) were grown by the travelling solvent floating zone method. ARPES experiments were carried out at BL 7U of UVSOR using $h\nu$ = 7 eV - 8.5 eV photons. The total energy resolution was set at 7 - 8 meV. Temperature was set at T = 12 K and clean sample surfaces were obtained by cleaving single crystals *in-situ* in an ultrahigh vacuum better than 7×10^{-9} Pa. The samples were aligned by Laue diffraction and set so that the direction of Cu-O [(π, 0)-(π, π)] was perpendicular to the electric field direction of the incident light.

In order to estimate the SC gap of overdoped Bi2223, symmetrized energy-momentum (*E*-*k*) plots in the offnodal region taken at different photon energies are presented in Fig. 1. Black bars show the peak position of the energy-distribution curve (EDC) indicating the SC gap size. The SC gap estimated along the Fermi surface (FS) is plotted as a function of the *d*-wave order parameter in Fig. 1(c). The SC gaps of the inner-plane band (IP) and outer-plane-antibonding band (OP-AB) show almost the same magnitudes (Δ_{IP} ~ 50 meV and $\Delta_{OP\text{-}AB}$ ~ 40 meV) as the previous ARPES study [8]; however, that of the outer-plane-bonding band (OP-BB) shows a smaller gap size at the antinode ($\Delta_{OP\text{-}BB}$ ~ 20 meV). This result indicates that the large SC gap of OP-AB may contribute to the higher T_c in the overdoped Bi2223.

As future work, we need to investigate the Fermi arc length in order to determine how much these three bands contribute to the superconductivity. Also, theoretical work to interpret the different SC gap magnitude of the three bands should be done.

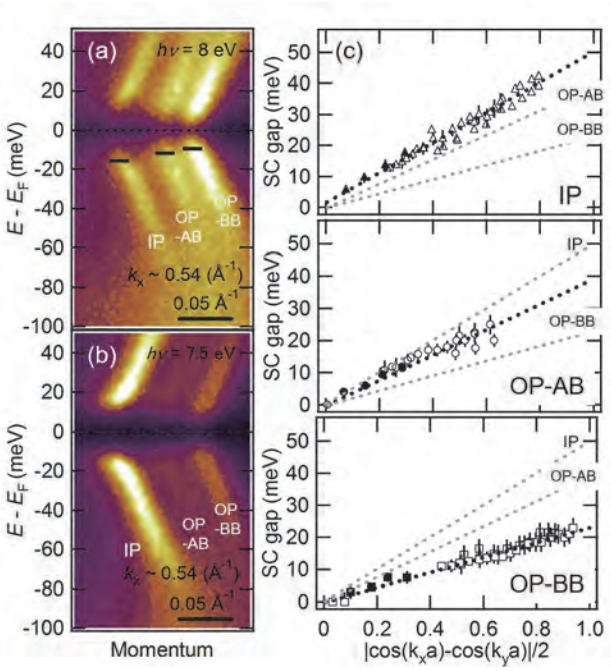

Fig. 1. Symmetrized *E*-*k* plots in the Cu-O bond direction taken at $h\nu$ = 8 and 7.5 eV (T = 12 K) and SC gap anisotropy. IP, OP-AB, and OP-BB indicate the inner, middle, and outer bands, respectively.

[1] J. M. Wheatley *et al*., Nature **333** (1988) 121.
[2] T. Fujii *et al.,* Phys. Rev. B **66** (2002) 024507.
[3] E. Pavarini *et al*., Phys. Rev. Lett. **87** (2001) 047003.
[4] S. Chakravarty *et al*., Nature **428** (2004) 53.
[5] S. Okamoto *et al*., Phys. Rev. Lett. **101** (2008) 156401.
[6] D. L. Feng *et al*., Phys. Rev. Lett. **88** (2002) 107001.
[7] T. Sato *et al*., Phys. Rev. Lett. **91** (2003) 157003.
[8] S. Ideta *et al*., Phys. Rev. Lett. **104** (2010) 227001.
[9] S. Ideta *et al*., Phys. Rev. B **85** (2012) 104515.
[10] S. Ideta *et al*., Physica C **470** (2010) S14-S16.
[11] S. Ideta *et al.*, Activity repot **43** (2015) 45.

BL7U

Self-Energy in the Superconducting States of the High-T_c Cuprates $Bi_2Sr_2CaCu_2O_{8+\delta}$

D. Ootsuki[1], K. Yamawaki[1], D. Shimonaka[1], D. Shibata[1], H. Eisaki[2], T. Sasagawa[3], A. Fujimori[4], S. Ideta[5], K. Tanaka[5] and T. Yoshida[1]

[1]*Graduate School of Human and Environmental Studies, Kyoto University, Kyoto 606-8501, Japan*
[2] *National Institute of Advanced Industrial Science and Technology (AIST), Tsukuba 305-8562, Japan*
[3]*Materials and Structures Laboratory, Tokyo institute of Technology, Yokohama 226-8503, Japan*
[4]*Department of Physics, University of Tokyo, Tokyo 113-0033, Japan*
[5]*UVSOR Facility, Institute for Molecular Science, Okazaki 444-8585, Japan*

Angle-resolved photoemission spectroscopy (ARPES) can directly detect the spectral function $A(\boldsymbol{k},\omega)$ and, hence, one can determine the self-energy $\Sigma(\boldsymbol{k},\omega)$. From the discovery of the kink structure in the high T_c-cuprate superconductors, a considerable number of studies have been conducted on the self-energy in the nodal region where the superconducting gap closes [1, 2]. On the other hand, the self-energy in the anti-nodal region in the superconducting states also has many information of the formation of Cooper paring. Several studies have reported the self-energy in the anti-nodal region in the superconducting state and pointed out that there is a bosonic structure [3, 4]. However, the origin of the bosonic mode has not been clarified yet.

In the present study, we have performed an ARPES study of the over-doped $Bi_{2-x}Pb_xSr_2CaCu_2O_{8+\delta}$ (Pb-Bi2212) in order to determine the self-energy in the superconducting state. Here, we have applied Kramars-Kronig relation to $A(\boldsymbol{k},\omega)$ for deducing the self-energy $\Sigma(\boldsymbol{k},\omega)$ in a wide energy range [3, 5]. ARPES experiment was carried out at BL7U of UVSOR. All the data were taken with the photon energy $h\nu$ = 22.7 eV. The total energy resolution was ~10 meV. The single crystal Pb-Bi2212 was cleaved in the pressure better than 1.6×10^{-8} Pa. The measurement temperature were T = 16 K and 110 K.

Figure 1 shows the spectral function $A(\boldsymbol{k},\omega)$, the real part $\mathrm{Re}\Sigma(\boldsymbol{k},\omega)$ and the imaginary part $\mathrm{Im}\Sigma(\boldsymbol{k},\omega)$ of the self-energy deduced from ARPES spectra using the Kramers-Kronig transformation. A sharp quasiparticle peak appears corresponding to the gap opening in the superconducting state in Fig.1 (a). In the imaginary part of the self-energy $\mathrm{Im}\Sigma(\boldsymbol{k},\omega)$, the peak at E_F increases from the nodal to anti-nodal regions, which indicates the d-wave superconducting gap. In the anti-nodal region, the dip structure around 50 meV are observed in the spectral function, compared with that in the normal state. This dip structure in $A(\boldsymbol{k},\omega)$ corresponds to the drop in the imaginary part $\mathrm{Im}\Sigma(\boldsymbol{k},\omega)$ and is suppressed in going from the anti-nodal region to the nodal region. Also, the same energy scale ~50 meV appears in the $\mathrm{Re}\Sigma(\boldsymbol{k},\omega)$ below T_c, particularly in the anti-nodal direction.

In summary, we have deduced the self-energy in the superconducting states and found a characteristic energy scale ~50 meV, corresponding to the peak-dip hump structure of the spectral function. Since the characteristic structure evolves in the anti-nodal region, the observed energy scale may be relevant to the signal of the Cooper paring.

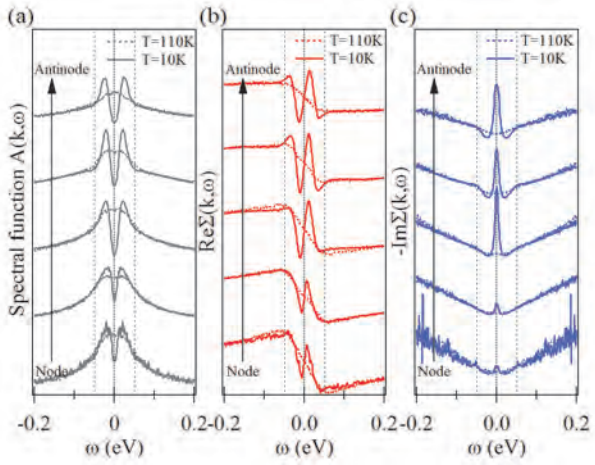

Fig. 1. (a) Spectral function $A(\boldsymbol{k},\omega)$ for the over-doped Pb-Bi2212. (b),(c) The real part $\mathrm{Re}\Sigma(\boldsymbol{k},\omega)$ and imaginary part $\mathrm{Im}\Sigma(\boldsymbol{k},\omega)$ of the self-energy deduced from the ARPES spectra using the Kramers-Kronig transformation.

[1] P. D. Johnson *et al.*, Phys. Rev. Lett. **87** (2001) 177007.
[2] A. Lanzara *et al.*, Nature **412** (2001) 510-514.
[3] M. R. Norman *et al.*, Phys. Rev. B **60** (1999) 7585.
[4] J. M. Bok *et al.*, Sci. Adv. **2** (2016) e1501329.
[5] S. Aizaki *et al.*, Phys. Rev. Lett. **109** (2012) 056401.

BL7U

Superconducting Gap of $Sr_{1-x}Ca_xFe_2(As_{1-y}P_y)_2$ (x = 0.08, y = 0.25) Revealed by Angle Resolved Photoemission Spectroscopy

T. Adachi[1], S. Ideta[2, 3], K. Tanaka[2, 3], Z. H. Tin[1], S. Miyasaka[1] and S. Tajima[1]

[1]*Graduate School of Science, Department of Physics, Osaka University, Toyonaka 560-0043, Japan*

[2]*UVSOR Facility, Institute for Molecular Science, Okazaki 444-8585, Japan*

[3]*School of Physical Sciences, The Graduate University for Advanced Studies (SOKENDAI), Okazaki 444-8585, Japan*

It is essential for elucidating the superconducting mechanism to evaluate the anisotropy of superconducting gap sizes in k-space. In our measurement performed last year, the topology of Fermi surfaces and the superconducting gap sizes on some points of Fermi surfaces in $Sr_{1-x}Ca_xFe_2(As_{1-y}P_y)_2$ (x = 0.08, y = 0.25) have been clarified. In this material, we have detected the gap minimum, which is possibly a node, in the outer electron Fermi surface around X point [1]. On the other hand, according to tight binding model + RPA calculation [2], it has been pointed out that there are superconducting gap nodes in the outermost hole Fermi surface among three hole Fermi surfaces around Z point in phosphorus doped 122 systems.

In this measurement, we observed the electronic structure, particularly the superconducting gap structure of hole Fermi surfaces near Z point of $Sr_{1-x}Ca_xFe_2(As_{1-y}P_y)_2$ (x = 0.08, y = 0.25, T_{cmax}=32K). Figure 1(a) shows Fermi surface mapping around Z point. We observed three hole Fermi surfaces around Z point, indicated by broken lines in Fig. 1(a). The superconducting gap values have been estimated at the points on these Fermi surfaces, which are indicated by dots in Fig. 1(a).

Figure 1(b) shows the superconducting gap value around Z point as a function of Fermi surface angle θ_{FS}. Here, θ_{FS} is restricted between 0 and 90 degrees reflecting the C_4 rotational symmetry of the crystal structure. The superconducting gaps on hole Fermi surface show small anisotropy but any node like behavior has not been detected. Considering the present and previous our results, only spin fluctuation due to Fermi surface nesting is not sufficient to explain the superconducting gap structures of phosphorus doped 122 systems. Our experimental results indicate that it is needed to take into account of the hybridization between the two electron pockets which makes the interlayer hopping finite, or the multiorbital effects such as orbital fluctuation due to interorbital quadrupole interaction [3, 4].

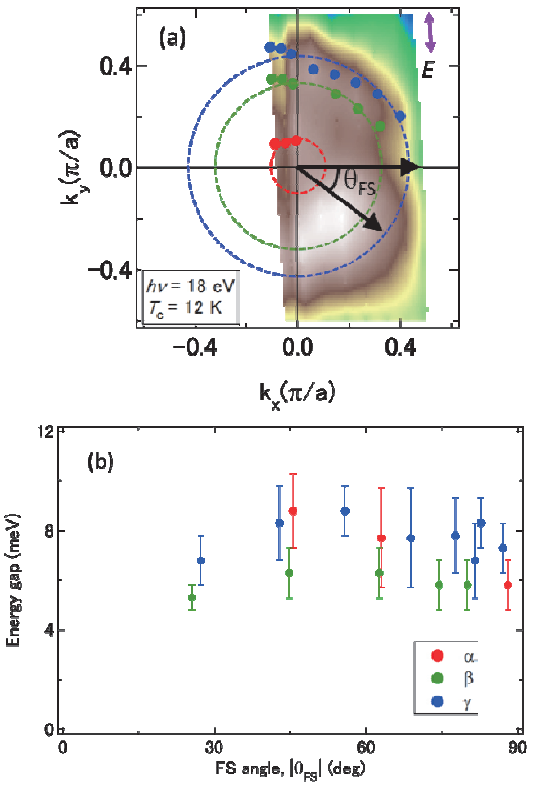

Fig. 1. (a) Fermi surface mapping around Z point in $Sr_{1-x}Ca_xFe_2(As_{1-y}P_y)_2$ (x = 0.08, y = 0.25). Three hole Fermi surfaces are indicated by the broken lines. The dots indicate the point, where the superconducting gap is estimated. θ_{FS} is Fermi surface angle. (b) Superconducting gaps around the Z point as a function of θ_{FS}.

[1] T. Adachi *et al.*, UVSOR activity report **43** (2016).
[2] K. Suzuki *et al.*, J. Phys. Soc. Jpn. **80** (2011) 013710.
[3] M. Khodas *et al.*, Phys. Rev. B **86** (2012) 144519.
[4] T. Saito *et al.*, Phys. Rev. B **88** (2013) 045115.

BL7B

Luminescence Properties of Ce- or Nd-doped $SrAl_2O_4$ Crystals with Vacuum Ultraviolet Excitation

D. Nakauchi[1], M. Koshimizu[2], T. Yanagida[1], G. Okada[1], Y. Fujimoto[2] and K. Asai[2]
[1]*Nara Institute of Science and Technology, Ikoma 630-0101, Japan*
[2]*Graduate School of Engineering, Tohoku University, Sendai 9808579, Japan*

Luminescence materials based on $SrAl_2O_4$ have extensively studied from a viewpoint of long-term persistent phosphors. In such usage, trap sites for electron-hole pairs are introduced by co-doping strategy. On the other hand, we recently reported excellent scintillation properties of Ce-, Eu-, or Nd-doped $SrAl_2O_4$ [1–3]. The band gap energy of $SrAl_2O_4$ is reported to be 6.5 eV, which corresponds to the energy of a photon with wavelength of 190 nm [4]. Therefore, vacuum ultraviolet (VUV) light is a suitable tool for analyzing the luminescence properties in the case of host excitation. In this report, we present the luminescence properties of Ce- or Nd-doped $SrAl_2O_4$ crystals with an emphasis on those with VUV excitation.

Undoped, Ce-doped, and Nd-doped crystals were grown in a floating zone method. Luminescence spectra with VUV excitation were measured at the Beamline 7B at UVSOR. X-ray-induced radioluminescence (RL) spectra were obtained using a CCD detector equipped with a monochromator.

Figure 1 shows the X-ray-induced RL spectrum of 1.0% Ce-doped $SrAl_2O_4$ crystal. A broad emission band at 380 nm is attributed to 5d-4f transition of Ce^{3+} ions. Figure 2 shows the excitation spectrum of a 1.0% Ce-doped $SrAl_2O_4$ crystal. The monitored wavelengths correspond to the 5d-4f transition of Ce^{3+} ions. 4f-5d transitions are clearly observed at 120 and 150 nm, in addition to a band-edge at 180 nm.

Figure 3 shows the photoluminescence spectra of undoped and Nd-doped $SrAl_2O_4$ crystals with excitation at 160–180 nm. The observed bands for the Nd-doped samples can be attributed to self-trapped excitons perturbed by Nd^{3+} ions.

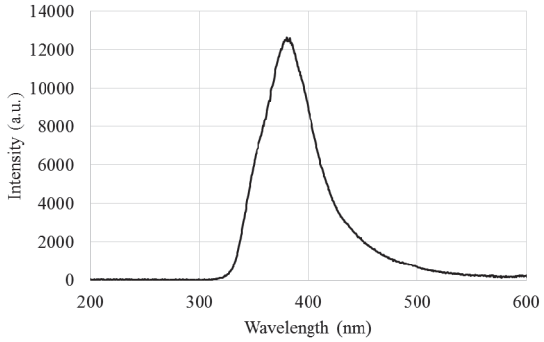

Fig. 1. X-ray-induced RL spectra of 1.0% Ce-doped $SrAl_2O_4$ crystal.

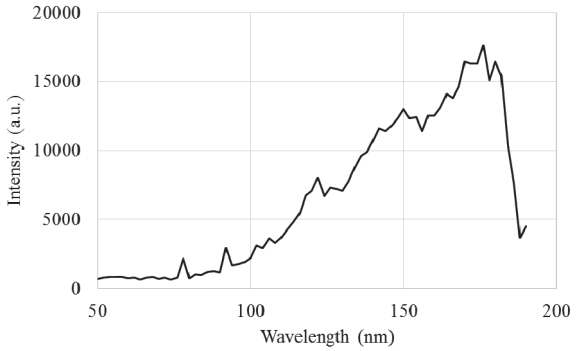

Fig. 2. Excitation spectra of 1.0% Ce-doped $SrAl_2O_4$ crystal. The monitored wavelengths correspond to the 5d-4f emission of Ce^{3+} ions.

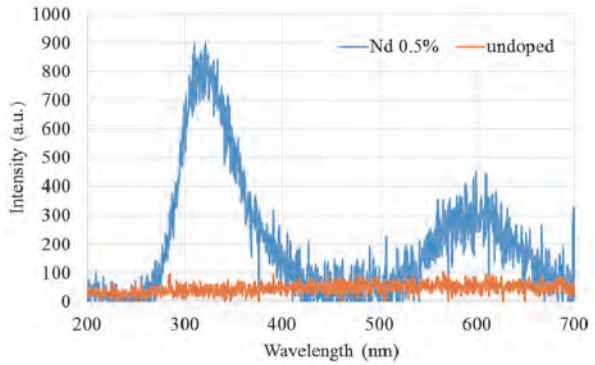

Fig. 3. Photoluminescence spectra of undoped and Nd-doped $SrAl_2O_4$ crystals with excitation at 160–180 nm.

[1] D. Nakauchi, G. Okada, M. Koshimizu and T. Yanagida, Nucl. Instrum. Methods Phys. Res. B **377** (2016) 89.
[2] D. Nakauchi, G. Okada, M. Koshimizu and T. Yanagida, J. Lumin. **176** (2016) 342.
[3] D. Nakauchi, G. Okada, M. Koshimizu and T. Yanagida, J. Rare Earths **34** (2016) 757.
[4] D. Jia, X.-J. Wang, W. Jiad and W. M. Yen, J. Lumin. **122–123** (2007) 311.

BL7B

Optical Properties of Pr^{3+} and Ce^{3+} Co-doped APLF Glass as a Fast Neutron Scintillator

T. Shimizu[1], Y. Minami[1], M. J. F. Empizo[1], M. V. Luoug[1], T. Taniguchi[1], A. Shiro[1], J. Watanabe[1], K. Yamanoi[1], N. Sarukura[1] and T. Murata[2]

[1] *Institute of Laser Engineering, Osaka University, Suita 565-0871, Japan*

[2] *Faculty of Education, Kumamoto University, Kumamoto 860-8555, Japan*

Neutron detection plays an important role in our society. Several characteristic parameters can be obtained by measuring neutrons which are generated by the fusion reaction and then elastically scattered in the high-density fusion plasma. On the other hand, neutron detection is considered as one of the non-destructive methods to inspect forms of infrastructure. Scintillator materials which are able to detect and discriminate neutrons should then be developed to be able to satisfy the demand.

The complex fluoro-oxide glass, $20Al(PO_3)_3$-80LiF (APLF) has been investigated as a candidate neutron scintillator material due to its high ^6Li content and fast decay times [1]. APLF glasses doped with Pr and Ce ions exhibit less than 30-ns decay times with optical, x-ray, and radioactive excitation. With broadband energy neutron excitation from ^{252}Cf, Pr-doped and Ce-doped APLF glasses have fast decay times of 5.3 and 28.9 ns, respectively, which are faster than a conventional scintillator, GS2 [2]. But like most scintillator materials, the fast lifetimes come at the expense of the emission intensities. To achieve fast decay times and high conversion efficiencies, we then devise a way to co-dope APLF glass with Pr and Ce. In this study, we investigate the optical properties of Pr/Ce-doped APLF glasses with different concentrations using the BL7B of UVSOR.

The optical properties of the Pr/Ce-doped APLF glasses were characterized using room-temperature photoluminescence (PL) and photoluminescence excitation (PLE) spectroscopies. Three samples were prepared, namely: (1) APLF glass doped with 1.0 mol% Pr and 2.0 mol% Ce (APLF+1.0Pr/2.0Ce); (2) APLF glass doped with 1.5 mol% Pr and 1.5 mol% Ce or (APLF+1.5Pr/1.5Ce); and, (3) APLF glass doped with 2.0 mol% Pr and 1.0 mol% Ce or (APLF+2.0Pr/1.0Ce). All samples were cut into 20-mm diameter cylinders with 8-mm thickness and were polished on both sides to an optical finish.

Figure 1 shows the PL spectra of the Pr/Ce-doped APLF glasses with 200-nm excitation. The emission peaks, which shift to lower wavelengths with decreasing Ce concentration, correspond to the inter-configurational 5d-4f transition of Ce^{3+}. In addition, all samples exhibit small emission peaks, which correspond to the 4f5d → $^3H_4$, $^1S_0$ → $^3F_4$, and $^1S_0$ → $^1G_4$ transitions of Pr^{3+}. The intensity of these emission peaks increases with increasing Pr concentration.

Figure 2 shows the PLE spectra of the Pr/Ce-doped APLF glasses monitored at their dominant peak emissions (~ 340 nm). This glasses exhibits a broad excitation channel and a peak at 270 nm regardless of the Pr and Ce concentration. These results suggest that the ~ 340-nm emission (5d-4f Ce^{3+} transition) has efficient excitation with 270 nm as evidenced by the PL spectra of the Pr/Ce-doped APLF glasses with 270-nm excitation in Fig. 2. On the other hand, the PLE spectra monitored at around the emissions corresponding to the Pr^{3+} transitions are not recorded because of their weak intensities.

The effect of co-doping on the optical properties of APLF will be elucidated in the future.

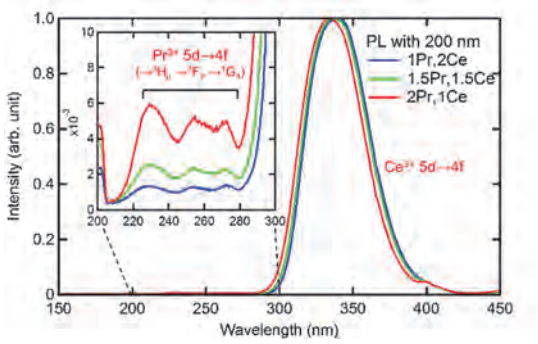

Fig. 1. PL spectra of Pr/Ce-doped APLF glasses with 200-nm excitation.

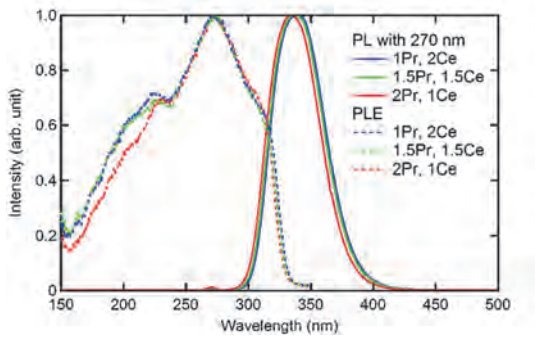

Fig. 2. PLE monitored at ~ 340 nm and PL spectra with 270-nm excitation of Pr/Ce-doped APLF glasses.

[1] Y. Arikawa *et al.*, Rev. Sci. Instrum. **80** (2009) 113504.

[2] Y. Arikawa *et al.*, Rev. Sci. Instrum. **81** (2010) 106105.

BL7B

Excitation and Emission Spectra of Pr-doped SrY_2O_4

M. Yoshino, S. Nishiki and S. Watanabe
Graduate School of Engineering, Nagoya University, Nagoya 464-8603, Japan

The trivalent lanthanide ions (e.g., Ce^{3+}, Nd^{3+}, Er^{3+}) in oxide crystals have drawn attentions due to their application for luminescent materials in NIR to UV regions such as solid-state lasers, phosphors or scintillators. The trivalent praseodymium ion, Pr^{3+}, has also attracted attentions as luminescence centers. In this work, the excitation spectra and emission spectra for Pr^{3+} in SrY_2O_4 crystal have been measured. The Pr-doped SrY_2O_4 samples are synthesized by solid state reactions. The samples are annealed in N_2-H_2 atmosphere in order to reduce Pr^{4+} to Pr^{3+}. The concentration of Pr in the samples are 0.2, 1.0 and 5.0 mol%.

The excitation spectrum monitored at 518 nm emission is shown in Fig. 1. The peak near 200 nm relates the absorption from the optical transition around the band edge in SrY_2O_4. This corresponds to the peak in the spectrum monitored at 423 nm in pure SrY_2O_4 [1]. The absorption around 315 nm and 273 nm originate the 4*f*-5*d* transitions of Pr^{3+}. The emission spectra at 315 and 273 nm excitation in 300 K are shown in Fig. 2 and Fig. 3, respectively. Peaks A, B, C exist in the each spectra. On the other hand, peak D appears only in 273 nm excitation and has different dependency to Pr concentration compared with the other peaks. The intensity of D decrease with Pr concentration while it decreases after the increase in A, B and C. The emission spectra at 273 nm excitation in different temperatures are shown in Fig. 4. It is found that the peak D has also different dependency to temperature compared with the peaks A, B and C.

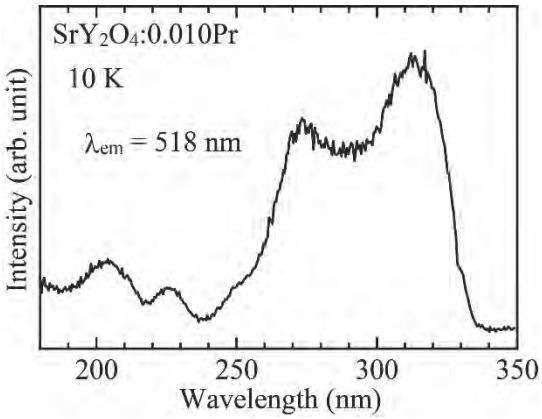

Fig. 1. Excitation spectrum of SrY_2O_4:0.010Pr.

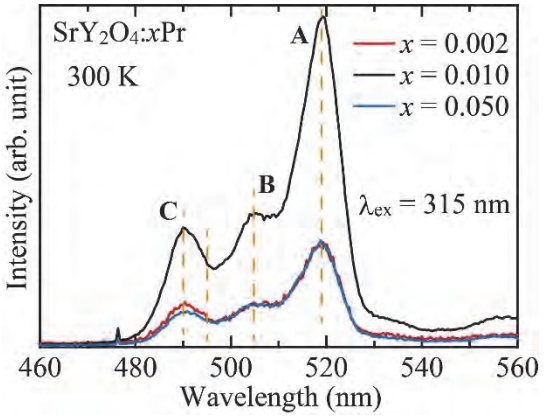

Fig. 2. Emission spectra of SrY_2O_4:*x*Pr. (λ_{ex}= 315 nm, 300 K)

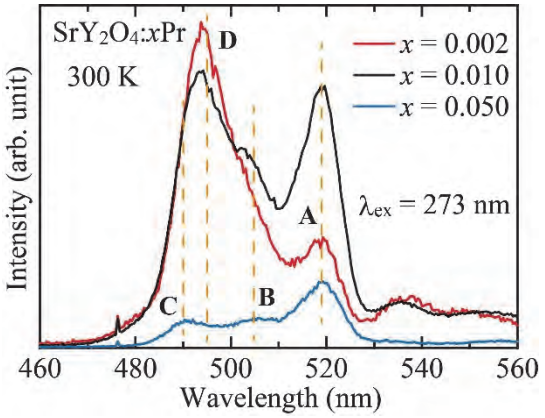

Fig. 3. Emission spectra of SrY_2O_4:*x*Pr. (λ_{ex}= 273 nm, 300 K)

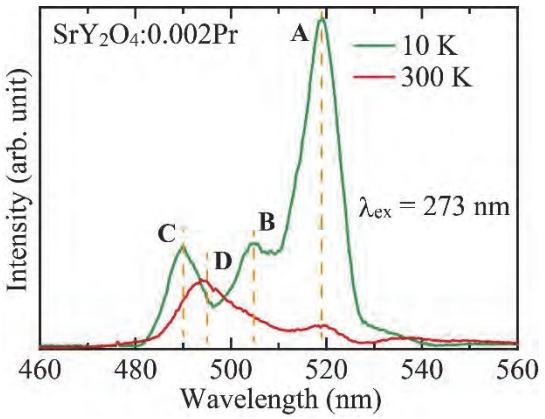

Fig. 4. Emission spectra of SrY_2O_4:0.002Pr. (λ_{ex}= 273 nm)

[1] M. Yoshino, S. Watanabe and Y. Ichikawa, UVSOR Activity Report **36** (2009) 122.

BL7B

Optical Conductivity of Zn-Ag-Sc Quasicrystal and Approximant Crystal

K. Imura[1], M. Hayashi[1], S. Kimura[2, 3] and N. K. Sato[1]

[1]*Department of physics, Graduate School of Science, Nagoya University, Nagoya 464-8602, Japan*

[2]*Graduate School of Frontier Biosciences, Osaka University, Suita 565-0871, Japan*

[3] *Department of Physics, Osaka University, Toyonaka 566-0043, Japan*

Quasicrystal (QC) is a solid in which constituent atoms are arranged according to a special rule "quasi-periodicity". QCs show a sharp x-ray diffraction pattern as shown in usual crystals, however, peculiar five or ten folded rotation symmetry is observed which is forbidden to normal crystals [1]. Therefore, the electronic state of the QC is considered to be different from the normal one; however, it has not been clarified experimentally yet. Zn-Ag-Sc QC which has an isostructural to a typical binary icosahedral Cd-Yb QC [2], and Zn-Ag-Sc approximant crystal (AC), which has locally the same structure as QC are target materials of this study.

Polycrystalline Zn-Ag-Sc QC and AC were obtained by annealing method using an evacuated quartz tube. The reflectivity measurement in the visible, ultraviolet, and vacuum-ultraviolet region i.e., the photon energy region of 1.2-30 eV, was performed at the BL7B which consists of a 3-m normal incidence monochrometer at room temperature. Low-energy reflectivity (0.01-1.5 eV) has been carried out by using a Michelson-type rapid-scan Fourier spectrometer at selected temperatures from 10 to 300 K. The optical conductivity spectra σ(ω) were obtained from the Kramers-Kronig analysis (KKA) of the reflectivity spectra extrapolating to zero-energy (DC) limit assuming Hagen-Rubens relation.

Figure 1 shows an incident energy dependence of the reflectivity $R(\omega)$ at several temperature. Comparing between QC and AC, $R(\omega)$ of QC is higher than AC in a wide energy region and some broad structures are observed at around 0.09, 1 and 3 eV.

Figure 2 shows optical conductivity spectra σ(ω) of AC at several temperatures from 10 to 300 K obtained by KKA. σ(ω) slightly increases as decreasing temperature which is consistent with the DC conductivity as shown in the inset of Fig. 2. It does not seem to reach the DC value even if it is extrapolated smoothly.

σ(ω) decreases as increasing photon energy at whole temperatures. This energy dependence is qualitatively different from icosahedral-QC Al-Cu-Fe: the σ(ω) increases linearly from DC limit to near-IR region [3]. An understanding of this difference may give important information to elucidate the electronic state of the QC. In order to clarify the low-energy electronic state, further experiments are needed.

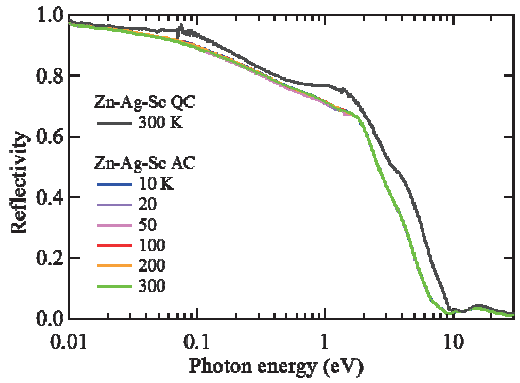

Fig. 1. Incident photon energy dependence of the reflectivity of Zn-Ag-Sc quasicrystal (T = 300 K) and 1/1 approximant crystal (T = 10, 20, 50, 100, 200, 300 K).

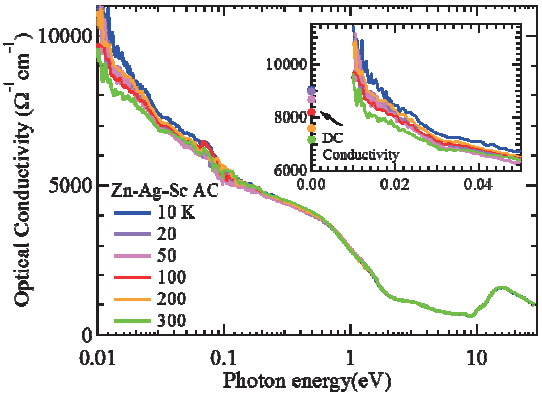

Fig. 2. Incident photon energy dependence of the optical conductivity of Zn-Ag-Sc 1/1 approximant crystal. Closed circles show DC conductivity measured by conventional four terminal method.

[1] D. Shechtman, I. Blech, D. Gratias and J. W. Cahn, Phys. Rev. Lett. **53** (1984) 1951.

[2] H. Takakura, C. P. Gomez, A. Yamamoto, M. Boissieu and A. P. Sai. Nature Matter. **6** (2007) 58.

[3] C. C. Homes, T. Timusk, X. Wu, Z. Altounian, A. Sahnoune and J. O. Strom-Olsen, Phys. Rev. Lett. **67** (1991) 2694.

BL7B

Effects of Fluorine Substitution on the Bi 6s-6p Transition of Zinc Bismuth Phosphate Glass

N. Kitamura
National Institute of Advanced Industrial Science and Technology, Ikeda 563-8577, Japan

Bismuth phosphate glasses, which have high refractive index and low deformation temperature, are candidate materials for producing high performance optical components such as compact lenses and diffractive optics. It is of interest that a zinc bismuth phosphate glass system has two distinct glass-forming regions; orthophosphate and isolated phosphate structures are dominant in the region that the atomic ratio O/P is higher than 3.5 and metaphosphate and pyrophosphate structures are dominant in the region of O/P < 3.5 [1, 2]. We have reported the glass structure and local structure around bismuth ions in a previous work [2, 3]. Recently, we found that the absorption edge of the glasses in the region O/P<3.5 shifts higher energy side by substituting ZnF_2 for ZnO [4], as shown in fig. 1. In the present study, reflectivity of the fluorine substituted bismuth phosphate glasses has been measured to make clear the band structure in the vacuum ultraviolet region.

Ternary $55ZnO\text{-}20Bi_2O_3\text{-}25P_2O_5$ glass was used a base glass. Fluorine doping was performed by substituting ZnF_2 for ZnO in the mixture of starting materials (ZnO, Bi_2O_3, and $Zn(PO_3)_2$). Fluorine content was determined by the electron probe micro analysis (EPMA). Two samples, 8%ZnF_2 (x=10 in fig.1) and 12%ZnF_2 (x=20 in fig. 1) substituted glasses, were used for reflection measurement. Reflectivity of optically polished samples was measured in the photon energy region of 3.6-25 eV with an incident angle of 10˚ at the BL7B.

Figure 2 shows reflection spectra of the un-substituted $55ZnO\text{-}20Bi_2O_3\text{-}25P_2O_5$ glass, and 8% and 12% ZnF_2 substituted glasses. Spectra for polycrystalline samples of BiF_3, ZnF_2 and ZnO were also shown in the figure. Distinct reflection peak and broad contour were respectively observed at around 4.5 eV and 5-10 eV. The peak and contour are assigned to the $6s^2 \rightarrow 6s^1 6p^1$ transition in the Bi^{3+} ion [2, 4-6]. We know that transitions from the ground state ($^1S_0$) to excited states $^3P_0$ and $^3P_2$ are spin-forbidden, but transition to $^3P_2$ level would be allowed by spin-orbit coupling [6]. Therefore, the lower distinct peak is expected to the $^1S_0 \rightarrow {}^3P_1$ transition and the next contour could be due to the $^1S_0 \rightarrow {}^3P_2$ and $^1S_0 \rightarrow {}^1P_1$ transition at least. The peak of BiF_3 was located at about 5.0 eV. The lowest peak at 4.5eV for the glass sample shifted toward higher energy side by the substitution, and the magnitude of the peak shift was about 0.3 eV by the 12%ZnF_2 substitution. It was very consistent with the absorption edge shift (~0.3eV). It was deduced that some of substituted fluorine ions would terminated to bismuth ions directly for oxygen ions.

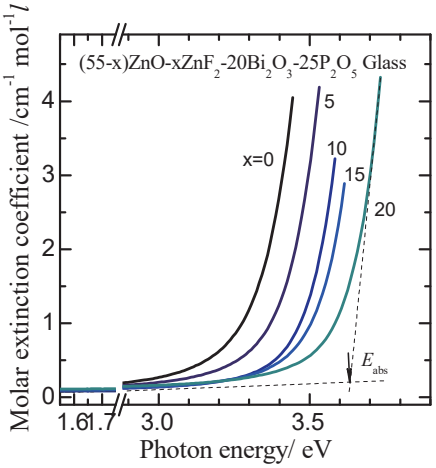

Fig. 1. Absorption spectra of (55-x)ZnO-xZnF_2-20Bi_2O_3-25P_2O_5 glasses.[4]

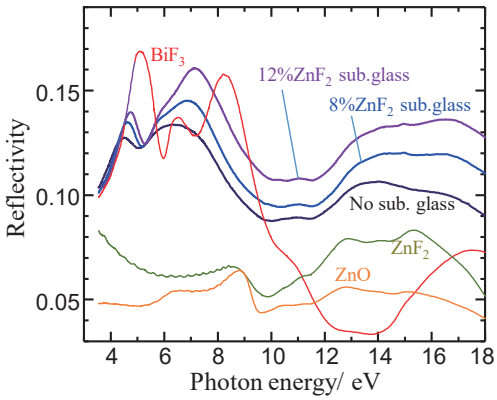

Fig. 2. Reflection spectra of 8% and 12% fluorine (ZnF_2) substituted $55ZnO\text{-}20Bi_2O_3\text{-}25P_2O_5$ glass. Spectra of un-substituted glass, polycrystalline BiF_3, ZnO and ZnF_2 also shown.

[1] B. Elouadi *et al.*, Phase Trans. **13** (1988) 219.
[2] N. Kitamura *et al.*, Mater. Sci. Eng. B **161** (2009) 91.
[3] N. Kitamura and K. Fukumi, J. Ceram. Soc. Jpn. **121** (2013) 355.
[4] N. Kitamura *et al.*, J. Non-Crysta. Solids **357** (2011) 1188.
[5] G. Blasse and A. Bril, J. Chem. Phys. **48** (1968) 217.
[6] R. H. P. Awater and P. Dorenbos, J. Lumin. **184** (2017) 221.

UVSOR User 5